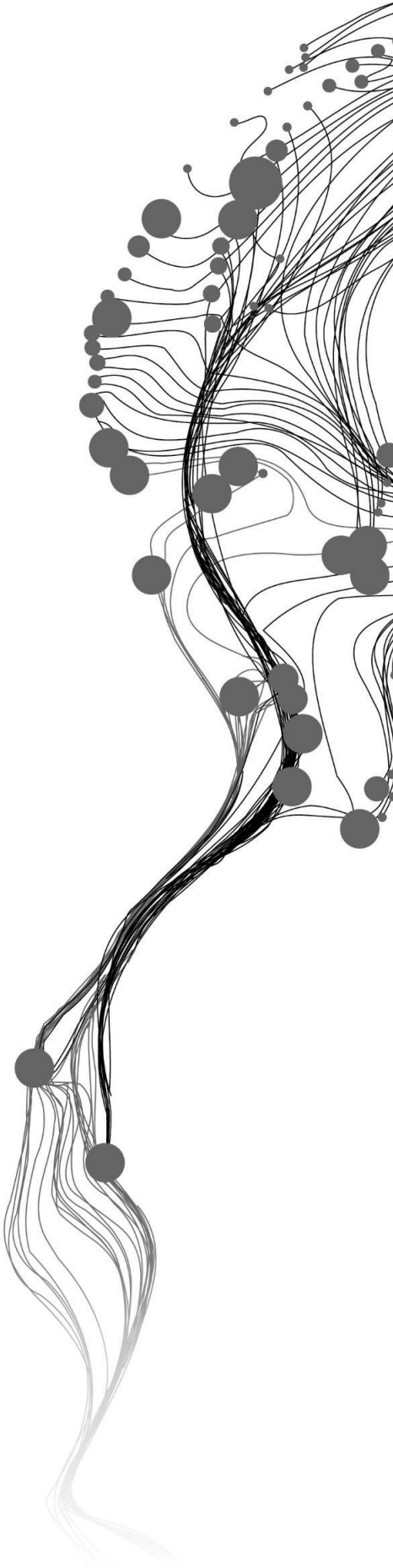


Detecting Artisanal Small-Scale Gold mines with LandTrendr multispectral and textural features at the Tapajós river basin, Brazil.

ALEJANDRO FONSECA GOMEZ
JUNE, 2021

SUPERVISORS:

Dr. M.T Marshall
Dr. ir. Suhyb Salama



Detecting Artisanal Small-Scale Gold mines with LandTrendr multispectral and textural features at the Tapajós river basin, Brazil.

ALEJANDRO FONSECA GOMEZ

Enschede, The Netherlands, June 2021

Thesis submitted to the Faculty of Geo-Information Science and Earth Observation of the University of Twente in partial fulfilment of the requirements for the degree of Master of Science in Geo-information Science and Earth Observation.

Specialization: Natural Resources Management

SUPERVISORS:

Dr. M.T Marshall
Dr. ir. Suhyb Salama

THESIS ASSESSMENT BOARD:

Dr. R. (Roshanak) Darvishzadeh (Chair)
Dr. H.M.A. van der Werff (External examiner)

ABSTRACT

Artisanal Small Scale Gold Mines (hereafter ASGM) is one the major disturbances in the Amazon Forest, which lately has received scientific attention owing to the environmental impact in water sources because of the use of mercury in the amalgamation process, the deforestation trend in the mine settlements, the association with insurgent groups, and direct linkage with 8 out 17 United Nations SDGs. UN Environment Program under the Minamata Convention on Mercury and the planetGOLD program has provided some guidelines to foster the National Action Plans (NAP) to incorporate formalization, mitigation, and adaptation processes of the ASGM activities, which leads to the reduction of mercury usage, decreasing the environmental impact and improving the socio-economic conditions of the population-related with the ASGM. The NAP encourages the local government – among others- the implementation and development of a monitoring system program dedicated to delimitating and identify the ASGM and assess the environmental impact that allows the land title and formalization of areas dedicated to. Current methods of monitoring ASGM activities are time-consuming, resource-intensive, and unable to cover extended areas such as military campaigns and aerial reconnaissance by aircraft. However, some different approaches in remote sensing have been used to face the NAP requirements and improve the monitoring of the ASGM using spectral land characteristics, concluding that mixed label classes are not separable by just the use of spectral information. Therefore, this research proposes an innovative remote sensing approach that combines multifeatured spectral and textural analysis with Landsat time series to map and detect the ASGM in the Tapajós River Basin (Brazil) from 2000 to 2019.

LandTrendr is the time series algorithm employed that uses Landsat images to perform temporal segmentation of pixel value trajectories over time to detect forest disturbances. Every pixel is fitted with a linear regression model represented by a set of vertex and segments rendering the land cover changes in a 2D profile, allowing to incorporate the spectral and temporal attributes to classify forest loss because of ASGM activities.

The entire set of predictors (86) were prone to assess feature relevance/importance through Variable Selection Using Random Forest (VSURF), which uses a stepwise regression in an ensemble model to efficacy remove noise considering the OOB error and the mean decrease error to select the most important features in ASGM detection. After performing feature importance and feature reduction, a final set of 33 features (26 textures, 5 spectral indices, and 2 topographic data) were used for binary (Mine – No Mine) using Random Forest Classifier. For the tuning parameter, 500 ntrees (number of trees) and 6 mtry (number of drawn candidate variables in each split) with 50 iterations were used for classification purposes, achieving an overall accuracy of 90.8%. Additionally, a probabilistic classification (probability of ASGM presence) was also performed considering that the threshold between classes is not clearly defined in the landscape and the transition areas from one class to another are fuzzy. An average vote counting of the threes in the Random Forest model was used to calculate the probability of ASGM occurrence at pixels level. The results show that the proposed method is reliable and robust to detect the forest disturbances produced by ASGM activities and arise as an alternative to achieve the NAP.

Keywords: ASGM, LandTrendr, Texture-features, VSURF, Random Forest, Landsat

ACKNOWLEDGEMENTS

I would like to thank my supervisors Dr. Michael Marshall and Dr. ir. Suhyb Salama for their valuable guidance and support throughout the research process; without their continuous advice and supervising, this work could not have been done smoothly and enjoyable. My humble gratitude for following me and supporting me with this idea which looked like scribbled lines at the earliest phase but got shape thanks to their thought-provoking questions and constant encouragement throughout this research.

I also would like to extend my gratitude to the ITC Excellence Scholarship to financially support part of my education and allow me to come to the Netherlands to study as an international student. My sincere gratitude to Dr. Roshanak Darvishzadeh, chair of the thesis assessment board, for her constructive feedbacks during the proposal defense and mid-term presentation.

My appreciation also goes to Drs. E.H. Kloosterman, whose constant support in the neediest moments was invaluable for the good ending of this journey, not only as a professor but also as a friend.

My gratitude and respect to my mentor Dr. I.C van Duren, for your continuous suggestions and notable advice to help me out go through these tough covid months.

Last but not least, I would like to express my profound gratefulness to my parents for their love, for encouraging me throughout this phase of my life, and for their immense support and sacrifices. My appreciation also goes to my best friend, Jorge, for rendering necessary help whenever required, for our productive conversations, discussions, suggestions, and insights. My heartfelt greatest gratitude to my beloved girlfriend Rebeca for the restless support and unconditional love she has always had for me. Nobody else but you, deserve this achievement.

Alejandro Fonseca
June 2021
Enschede

TABLE OF CONTENTS

1. INTRODUCTION	6
1.1 Background	6
1.1.1 Socio-Economical and Environmental problems related to ASGM	7
1.1.2 ASGM Formalization Approach.....	7
1.1.3 Monitoring ASGM activities	8
1.1.4 Methods in Remote Sensing for identifying the ASGM.....	9
1.1.5 Challenges in Monitoring ASGM with Remote Sensing.....	10
1.1.6 LandTrendr Time Series Algorithm.....	11
1.1.7 Spatial Relations Analysis by Texture image extraction	12
1.1.8 Incorporating Ancillary Data for Problem Context	12
1.1.9 Random Forest in the Classification Process	13
1.1.10 Problem Statement	14
1.2 Research Objectives.....	15
1.2.1 Specific Objectives	15
1.2.2 Research Question	15
2. STUDY AREA AND DATA USED	16
2.1 Study Area	16
2.2 Dataset used.....	17
2.3 ASGM Dataset.....	18
2.4 Landsat Satellite Images Landsat 7 ETM + and Landsat 8 OLI	19
2.5 NASA SRTM Digital Elevation	20
2.6 Roads and Water Bodies.....	20
3 METHODOLOGY.....	21
3.1 Data Preparation.....	22
3.1.1 Unbalanced Data	23
3.1.2 Image Pre-Processing and Harmonization.....	25
3.1.3 Cloud Masking and Mosaic Composition.....	27
3.1.4 Texture Feature Extraction.....	29
3.1.5 Spectral Indices	31
3.2 Temporal segmentation using LandTrendr.....	32
3.2.1 Setting Parameter Model and Temporal Segmentation	33

3.2.2	LandTrendr Outputs	35
3.2.3	Ancillary Data	39
3.3	CLASSIFICATION	42
3.3.1	Random Forest	42
3.3.2	Variable Selection Using Random Forest (VSURF)	44
3.3.3	Partial Dependence Plots (PDP)	47
3.3.4	RF Model Building	47
4.	RESULTS.....	49
4.1	Variable Selection and Feature Reduction Results	49
4.2	Partial Dependence Plots Prediction Model.....	52
4.3	Prediction Model Error Assessment	54
4.4	Binary Classification.....	56
4.5	Probabilistic Random Forest Classification.....	57
4.6	Change Detection.....	61
4.	DISCUSSION	62
4.1	LIMITATIONS	68
4.2	IMPLEMENTATION	68
5.	CONCLUSIONS.....	70
6.	REFERENCES	71
7.	APPENDIXES	82
7.1	LandTrendr Parameters for Texture.....	82
7.2	Partial Dependence Plots	83

LIST OF TABLES

Table 1. Dataset Used.....	17
Table 2. RAISG's Ground Truth data description	19
Table 3 Landsat sensor characteristics	19
Table 4. Harmonization Surface Reflectance Sensor Transformation Functions based	25
Table 5. Inputs Predictors used for Classification.....	29
Table 6. Texture Feature Description.....	30
Table 7. Spectral Indices used for Spectral Segmentation.	31
Table 8. LandTrendr segmentation Parameters (Kennedy et al., 2010).....	34
Table 9. Setting Parameters for LandTrendr using Spectral Indices as Input.....	34
Table 10. The Random Forest Input Parameters.....	47
Table 11. Ranking most important variables for Prediction Model	50
Table 12. Prediction model by type of features	50
Table 13. Ranking Variable Importance with Mean Decrease Accuracy and VI standard deviation	51
Table 14. Model Comparison Assessment.....	54
Table 15. Confusion Matrix for Binary Classification.....	56

LIST OF FIGURES

Figure 1 Area of Interest. (a) Top Left: Brazilian Federate States and Tapajós Basin Location. (b) Bottom Left: Area of Interest at the Tapajós River Basin. (c) Forest / No-Forest map of the Area of Interest.....	17
Figure 2. Methodology Flowchart.....	21
Figure 3. Area of Interest and ASGM digitized example date: 12-2001, image: Landsat / Copernicus Google Earth Pro.....	23
Figure 4. Sampling Schema for Mine and Non-Mine Classes	24
Figure 5. Time Series Image Collection using harmonization and NDVI.	26
Figure 6. NDVI Median Composite time-series images harmonized to Landsat 8 OLI.....	26
Figure 7. Harmonization and Image composite using medoid and NDVI as an example.	26
Figure 8 Image Annual-Composition Collection Structure (TrimbleInc, 2015).....	28
Figure 9. LandTrendr Temporal Segmentation.....	33
Figure 10. Temporal Segmentation of Spectral Indices	35
Figure 11. LandTrendr outputs configuration (Cohen et al., 2018)	36
Figure 12. LandTrendr Array output using NDVI values.	36
Figure 13. NDVI LandTrendr Output (MAG - YOD)	37
Figure 14. B7_Variance LandTrendr Output (MAG - YOD)	37
Figure 15. B5_Contrast LandTrendr Output (MAG - YOD)	38
Figure 16. NBR LandTrendr Output (MAG - YOD)	38
Figure 17. Ancillary Data: Aspect (AoI).....	39

Figure 18. Ancillary Data: TWI (AoI)	40
Figure 19. Ancillary Data: Elevation (AoI)	40
Figure 20. Ancillary Data: Slope (AoI).....	41
Figure 21. Ancillary Data: Euclidean Distance to Roads (AoI).....	41
Figure 22. Variable Importance using Mean Decrease Gini	43
Figure 23 Variable Importance using Mean Decrease Accuracy.....	44
Figure 24. Features sorted by decreasing mean Variable Importance	45
Figure 25 Nested RF model for model's definition with the lower OOB.....	46
Figure 26. Step-by-step added in regression for feature reduction	46
Figure 27. Prediction Model based on OOB Error.....	46
Figure 28. RF mntry tuning Parameter.....	48
Figure 29. RF ntrees Tuning Parameter.....	48
Figure 30. The threshold for Prediction Model and Interpretation model based on MSE.....	49
Figure 31. OOB Error delta mean square error per predictor variable	50
Figure 32. Partial Dependence Plot per Feature. Top: NDVI. Medium: B7_Var. Bottom: B5_Shade	52
Figure 33. Partial Dependence Plot per Feature. Top: B5_Prom. Medium: B5_Shade. Bottom: B7_Shade	53
Figure 34. OOB error and independent error for Top: the whole set of features. Medium: Interpretation Model Bottom: Prediction model	55
Figure 35. Binary Classification using Random Forest Classifier	57
Figure 36. ASGM Occurrence Probability in percentage (%)	59
Figure 37. ASGM Occurrence Probability Multiclass Percentage.....	60
Figure 38. Year of Detection using RGB representation (R:2000, G: 2010, B: 2019)	61

LIST OF APPENDIXES

1. List of LandTrendr parameters for texture features
2. PDPS

LIST OF ACRONYMS

- ASGM: Artisanal small-scale gold mines
UNEP: United Nations Environment Program
ILO: International Labor Organization
SDG: Sustainable Development Goal
SDC: Swiss Agency for development and cooperation
MIA: Minamata Initial Assessment
UNITAR: United Nations Institute for Training and Research
WHO: World Health Organization
NAP: National Action Plan (Minamata Convention)
AOI: Area of Interest

PDP: Partial Dependence Plot
MeHg: MethylMercury
LSWI: Land Surface Water Index
MNDWI: The Modified Normalized Difference Water Index
NBR: Normalized Burn Ratio Index
NDMI: Normalized Difference Moisture Index
NDPI: Normalized Differential Pond Index
NDVI: Normalized Differential Vegetation Index
NDWI: The Normalized Difference Water Index
GEE: Google Earth Engine
TWI: Topographic Wetness Index
LT: LandTrendr
RF: Random Forest
VSURF: Variable Selection Using Random Forest
SVM: Support Vector Machine
OOB-Error: Out of the Bag
MLC: Maximum Likelihood Classification
ANA: Agência Nacional de Águas e Saneamento Básico
IBGE: Instituto Brasileiro de Geologia e Estadística
RAISG: Amazonian Network of Georeferenced Socio-Environmental Information
USAID: United States Agency for International Development
NICFI: Norway's International Climate and Forest Initiative
GLCM: Gray-Level-CoOccurrence-Matrix
MAG: Magnitude of Change
YOD: Year of Detection
QA: Quality Assessment Band
ASM: Angular Second Moment
Corr: Correlation
Var: Variance
IDM: Inverse Difference Moment
Ent: Entropy
DVar: Difference Variance
Dent: Difference Entropy
Prom: Cluster Prominence
Diss: Dissimilarity
Shade: Cluster Shade

1. INTRODUCTION

1.1 Background

Artisanal and small-scale gold mining (hereafter ASGM) is a low-tech, labor-intensive mineral processing and extraction method conducted by a small group of local miners or small enterprises with limited capital investment and rudimentary techniques (UNEP, 2013). The legal status, defining criteria, and detailed definition of ASGM vary from country to country. Each country is responsible for defining ASGM in its national law and policy(UNITAR & UNEP, 2018). The debate on the definition of ASGM has continued for more than two decades without a clear resolution and a general agreement (Hinton, 2006). Nevertheless, for the scope of the current research, the definition used previously is attained with the Minamata Convention on Mercury (UNEP, 2013), declared by the United Nations Environment Program in 2013.

The ASGM sector produces about 12% to 15% of the world's gold extraction, and the activities have increased notably in the last years, attributed to the rise of gold prices in the international market (Swenson et al., 2011). Since the global economic crisis in 2008, the gold price has soared by 100%. Consequently, the gold exploitation in the Amazon countries has grown and expanded, triggering migration to mining areas, and increasing the environmental degradation issues associated with (Alvarez Berrios & Mitchell Aide, 2015).

ASGM is the largest source of mercury contamination and global emissions (UNEP, 2013). The activity is responsible for more than 37.7% of the global anthropogenic mercury emissions, with more than 800 tons/year (Veiga, Maxson, & Hylander, 2006). Particularly in the Amazon countries, releases to air, water, and land are approximate18% of the global annual mercury emission due to ASGM activities (AMAP/UN Environment, 2018). Also, according to The Carnegie Amazon Mercury Project, artisanal small-scale gold mines have dropped more than 150 tons of Mercury in the rivers since 2001 (CAMEP, 2013).

Mercury is a global pollutant that poses threats to human health (Veiga et al., 2006). Some harmful effects on the nervous and digestive system, lungs, kidneys, and immune system are highly associated with mercury exposure (World Health Organization, 2019). Some forms of Mercury have caused increases in several types of tumors that directly affect the heart and circulatory system (Ofosu et al., 2020). Some studies have found associations between mercury wastes in the human body with the probability to develop a reduction in motor function, poor leg coordination, visual contrast sensitivity, and manual dexterity (World Health Organization, 2019)

During the ASGM's process, excavators and dredgers dig up the riverbeds, and the mined material is processed at the same site to separate gold from sediments. Small mining ponds are excavated mechanically adjacently to the riverbed. On these ponds, the Mercury and cyanide are combined with the mined material to wash the ore. The resulting mixture of Mercury and gold, known as amalgam, is heated to vaporize the toxic mercury and leave the gold behind. Then the mercury waste is released from the ponds into the water streams, polluting the freshwater sources (Obeng et al., 2019). The Mercury is converted to methylmercury (MeHg)

in the aquatic ecosystems, which is easily bioaccumulated and spreads through the food net, toxic for humans and wildlife (Martín et al., 2020).

1.1.1 Socio-Economical and Environmental problems related to ASGM

ASGM activities are one of the most significant causes of land and environmental degradation (Obeng et al., 2019). Environmental impacts such as deforestation, landscape degradation, alteration of stream and river morphology, widespread environmental pollution, siltation of water bodies, biodiversity loss, among others, are the most significant adverse impacts of mineral exploitation. In the Brazilian Amazon, deforestation primarily from these sources was estimated to be 574 100 km² in 1998 (Peterson & Heemskerk, 2001); in the Peruvian Amazon, the pace is by around 2000 ha/year from 2006-2009, particularly at the "Madre de Dios Region" (Swenson et al., 2011). More than 80 natural reservations and buffer zones in the Amazon rain forest have presented substantial evidence of ASGM in their boundaries, and some 55 of them are located in indigenous communities (Ipenza & Valencia, 2014).

Although ASGM is a source of income for many people, its activities have brought multiples socio-economic impacts. According to the (ILO) International Labour Organization (2018), more than 2 million miners are involved in the ASGM activity in the Amazon. More than a million displaced peasants from areas with ore exploitations, and around 500 thousand children and women work in ASGM's without safety or healthy labor conditions. It is expected that by 2022 the number increase to 115 thousand and up to five million, respectively (Alvarez Berrios & Mitchell Aide, 2015). Besides, under the ILO convention No.182, work performed by children in ASGM is considered the "worst form of child labor" (International Labour Organization, 2018).

1.1.2 ASGM Formalization Approach

According to Hilson & Maconachie (2020), the regulation and control of ASGM must be seen as a new opportunity to minimize negative environmental and social impacts. The ASGM activities are significantly vital since they sometimes are unique livelihood sources for millions of people, particularly in developing countries (Hilson, 2002). The ASGM activities have been practiced for more than five centuries in more than 70 countries, and it represents a third of the total gold production annually. The estimated value of the gold production from ASMG is up to 25 billion USD per year (Rogers, 2005). Therefore, the formalization and regularization of the sector are needed, considering the magnitude of the official numbers, the socio-economic problems related with, the detrimental effects in the environment and human health, the business proficiency, and the direct relation with multiples SDG.

The ASGM sector is directly linked to 8 out of the 17 United Nations SDGs (Sustainable Development Goals) (Hilson & Maconachie, 2020). Remarkably, The SDG-1 (No Poverty), SDG-2 (Zero Hunger), SDG-3 (Good health and well-being), SDG-6 (Clean Water and Sanitation), SDG-7 Affordable and Clean Energy, SDG-8 (Decent work and economic growth),

SDG-11 Sustainable cities and communities, SDG- 12(Sustainable Consumption and Production), SDG-14 (Life Below Water), SDG-15 (Life on Land).

Reduce mercury emissions and used within the ASGM activities is an essential task to reduce environmental issues, decrease the human health consequences and control the labor conditions associated with it. A multi-disciplinary approach is needed to address the social, economic, and environmental issues to achieve global goals and foster sustainable development. Therefore, the formalization process and integration into the formal economy for a regulatory system are critical to addressing ASGM management.

Some formalization process such as the Sustainable Artisanal Mining Project (SAM) in Mongolia funded by the Swiss Agency for development and cooperation (SDC) (Swiss Cooperation Office, 2013), and the formalization approach based on experiences executed in Tanzania (UNEP, 2012) and Uganda (Hinton, 2006) have proven the benefits of the development of responsible artisanal mining adopting a human-rights based approach and environmental lesser impact—eliminating the use and distribution of mercury completely, and developing an ASGM miners committee for local organization and sustainable effectiveness (UNITAR & UNEP, 2018). The formalization also goes hand-in-hand with the agreement of the Minamata Convention on Mercury. Mainly and essentially Article 7. Which declares that countries with ASGM activities in their territories must develop a National Action Plan (NAP) outlining steps that will be taken to reduce and eliminate mercury use in the ASGM sector (UNEP, 2013). Moreover, the United nations environment, through the sustainable development goals and global environment facility, have developed the planetGOLD program with a guideline and plan for adaptation and mitigation of environmental impacts due to ASGM, where feasible constant monitoring and formalization or the ASGMs are declared indispensable requirements to eliminate the worst practices (PlanetGOLD, 2020)

These requirements urge formulating policies and increasing the provision of services among various agencies and institutions (e.g., education, environmental, labor, and health). The Natural Resources Defense Council and a team of experts in mining and policy development provide some recommendations for supporting countries' commitments under the Minamata Convention on Mercury and the fight against the spread of ASGM, which was provided to the United Nations Environment Program and present at the intergovernmental Negotiating Committee on Mercury (UNEP, 2013). The resulting guidance document sights the relevant and essential requirement of incorporating a suitable ASGM monitoring program as a mechanism of control that every country must adapt to the National Action Plans (NAP). The monitoring must assess and present the current state of the ASGM, addressing not only the mercury supply chain and the mercury trade at borders, but also in the environmental impact assessment, the ASGM camps, and the regulation and protection of the natural resources(UNITAR & UNEP, 2018).

1.1.3 Monitoring ASGM activities

The National Action Plan implies expanding the roles of the local or provincial government in monitoring the ASGMs and the activities related to them (UNITAR & UNEP, 2018). Nevertheless, the adaptation and implementation of the NAP in monitoring ASGM's face a set

the inconveniences that are even more problematic in the Amazon Rainforest context. Firstly, national government mining and environmental institutions often lack the capacity to monitor and enforce the ASGM sector regulations (UNEP, 2012). Secondly, the absence of state regulation at remote sites and the volatile nature of the ASGM operations tend to result in conflicts between miners and regional authorities (Salman & de Theije, 2017). The lack of enough technological instruments to fully incorporate a monitor system in the forest to assess the different types of forest disturbances, and finally, the complex nature of mining activities (Corbett, 2017), which is characterized by a diversity of scales, temporalities, processes, and techniques in the exploitation process. Such variability causes different impacts and footprints in the ecosystem and different sorts of evidence on the surface.

Given the environmental importance of the Amazon Rainforest and its relevant role in a climate change context, and following the guidelines from the UN Environment Program in the formalization approach of ASGM, and the increasing of the ASGM activities, a monitor system appears to be all the more needed. In that sense, remote sensing plays an invaluable role in assessing ecosystems' conditions and welfare, consistently capturing continuous information regarding the spectral, spatial, and temporal features. Additionally, it allows us to assess and monitor forest degradation and spatial distribution of the environmental impacts of anthropogenic activities (Nagendra et al., 2013). Additionally, given the global and temporal coverage and non-destructive characterization of the surface, its usability has been well recognized in the academic literature as a notable tool to identify geometric, spectral, spatial, and textural features of the land surface, enabling the analysis of ecosystem conditions (Obeng et al., 2019). On the other hand, the free accessibility to data and processing remote sensing tools raise as a suitable alternative for local or provincial governments or no profitable organizations for monitoring ASGM with low cost and high proficiency (Spiegel & Veiga, 2010).

1.1.4 Methods in Remote Sensing for identifying the ASGM

Remote sensing studies have used a variety of optical sensors and techniques for identifying and monitoring ASGM in the forest with different results (Asner & Tupayachi, 2017), and (Ngom et al., 2020) combined field surveys with airborne mapping and satellite imaging to assess road-and river-based gold mining districts in Peru and Senegal, respectively. In both situations, an extra validation with field survey was required to assess the final thematic map, given the challenges of access and interpretation of surrounding vegetation conditions. (Isidro et al., 2017) used satellite images with high spatial resolution such as Pleiades and SPOT imagery and object-based support vector machine classifier in the Philippines. The author considers that the proposed method cannot distinguish ASGM from other LULC classes as small-scale mining arose from the spatial, spectral, and textural similarities of various forms of bare soil. In contrast, the usability of topographical features provide more reliability for classifying the large-scale mine (Ibrahim et al., 2020) incorporate a Principal Component Analysis (PCA) using sentinel-2 images for ASGM detection in Colombia, getting a considerable performance in small areas but with similar results as (Isidro et al., 2017) regarding spectral similitude with other land covers in the final classification. Moreover, a qualitative inspection of the thematic maps produced by the high-resolution images also indicated that it might be possible to estimate the type of small-scale mine by the spatial and temporal context.

Using a spatial approach, particularly a semantic segmentation using the convolutional neural network method, was proposed by (Gallwey et al., 2020) in Ghana, with noticeable improvement and 90% overall accuracy compares to other traditional machine learning methods. However, the model requires to be assessed in different climatologic conditions, particularly in tropical forests where the availability of cloud-free images even in the dry season is lower and the forest density higher, the mining sector is notoriously informal (therefore no official records of the settlements) and processes such as deforestation is also related with. A multitemporal approach has been conducted by (F. L. Lobo, Costa, & Novo, 2015), (F. de L. Lobo et al. (2018), using a Landsat surface reflectance time series to assess changes in water quality and consequences to the aquatic environment due to ASGM activities at the Tapajós River. The author provides an alternative for water quality monitoring a recognizes the seasonality effect in the ASGM detection (dry and rainy period). Besides, the approach based on water quality parameters allows to detect big ASGM hot spots given that the water siltation effects are similar to the high-tech mining techniques, but the small ASGM patches are not easily detected using the approach. Additionally, the author incorporates a low time-consuming and high detection accuracy method using Google Earth Engine (GEE) for mapping mining areas within 13 regions of the Brazilian Amazon using Sentinel-2 images. Nevertheless, the mapping is generalized to industrial mining and based on the official mining dataset for training and validation purposes.

Additionally, LULC mapping methods also have been used to identify ASGM based on temporal forest changes (Almeida-Filho & Shimabukuro, 2002) with a post-classification approach and image segmentation. Nonetheless, the outcome was influenced by non-mining disturbances such as clear-cutting or dry grass and bank sands. The post-classification error was sensitive to the initial classification accuracy, requiring independent and additional verification.

1.1.5 Challenges in Monitoring ASGM with Remote Sensing

It is essential to consider some limitations and challenges that remote sensing faced in monitoring ASGM according to previous studies. (i) the absence of official information for training and validation purposes given the informality characteristic of the ASGM and the incapability to access ground truth efficiently (Güiza Suárez & Aristizabal, 2013). (ii) the specialized activity, characterized by a set of different techniques in scale and exploitation processes that produce different effects inland (F. de L. Lobo et al., 2018). (iii) the high intra-class spectral variability, related to the previous challenge, since the diversity of techniques and exploitation scales causes different impacts and evidences, such as bare soil, topsoil clearance, mining ponds, land pits, and logging patches (Isidro et al., 2017), this condition also leads to misclassification problems with other land covers such as dry soil, deforested patches, recently burned forest, and sandbanks along the water streams (Asner et al., 2013). (iv) the ASGM size and locations, according to (F. Lobo et al., 2016), a considerable amount of ASGM occurs within forest lands in small patches only detectable by images with high and medium spatial resolution. Additionally, the size is highly related to the specialized activity, and they can vary from half to hundreds of hectares. (v) Context absence in final land cover classification, some land uses such as roads and ports are part of the ASGM which must be considered in the monitoring process and included in consideration (F. Lobo et al., 2016a).

Considering the studies mentioned above and the challenges of using remote sensing for monitoring ASGM, it is clear that the traditional spectral class separability approach often causes misclassifications issues given the similar spectral features with other classes. Moreover, fuzzy boundaries and multiple different changes and impacts in the land cover induce addressing these challenges considering the spatial relations and pattern approach rather than spectral capabilities solely. Additionally, the seasonality effect (F. L. Lobo et al., 2015) leads us to consider the changes in the dry season, where the cloud-free images are more likely to capture land features, and the ASGM are more common. Finally, the incorporation of topographic or ancillary data might provide extra information regarding infrastructures associated with the ASGM such as roads or ports for classification and identification purposes.

Considering all these factors, it is likely that multisource and multitemporal analysis be feasible to identify and monitor the ASGM, given the challenges and nature of the problem presented above. On the one hand, the multifeatured approach includes spectral information from multispectral imaging collections, allowing to discriminate objects based on the spectral response at different wavelengths. It is complemented with information that describes the spatial relations and pattern identification by estimating texture features, which is a distinctive feature of every LULC class and thus valuable for compared classes that exhibit spectral similarities (Kupidura, 2019). Additionally, multisource image features are used in addition to multispectral image data to increase the thematic mapping accuracy (Marshall et al., 2017). As an alternative to confirming the quality of the outcomes and the proper interpretation of the data, context analysis must be considered to assess the observed changes and detect omission and commission errors in a thematic mapping (Lersch, Haertel, & Shimabukuro, 2007).

On the other hand, the multitemporal approach by the inclusion of time series provides a sequence of measurements of the same variable collected over time, allowing to monitor the changes, the temporal transitions, and capturing the complexities of the landscape changing surface (Gómez, White, & Wulder, 2016). Besides, time series in remote sensing has proved capacity for environmental issues characterization while describes trends and seasonal behavior, and thus allows to detect of temporal patterns by continuous monitoring (Gillanders et al., 2008), identifying the precise timing and magnitude of the change (R. E. Kennedy, Yang, & Cohen, 2010). Furthermore, a set of data in the timeline reduces adverse effects from the inherent process of capturing information in remote sensing, such as natural circumstances like cloud cover, illumination, atmospheric effects, and sensor deficiencies like radiometric gaps (Jensen, 2015).

1.1.6 LandTrendr Time Series Algorithm

The LandTrendr (i.e., The Landsat based detection of Trends in Disturbance and Recovery) is a pixel-based algorithm that uses temporal segmentation and fitting trajectory regression vertex-to-vertex to identify spectral trajectories from annual time series (Kennedy et al., 2010). The algorithm decomposes spectral information as a function of time (e.g., spectral bands or vegetation indices) using a set of parameters that assures that the fitting regression represents the temporal changes. The temporal segmentation is characterized by segments (vertex, points, breakpoints) representing the spectral trajectory's behavior in a period. The algorithm has been used for monitoring forest disturbances, particularly for industrial mining disturbance and

restoration in South Africa (Dlamini & Xulu, 2019a) and detecting vegetation recovery by coal mining in Inner Mongolia's Coalfield (W. Xiao, Deng, He, & Chen, 2020), also for assessing historical forest cover change in the lower Amazon floodplains (Fragal, Silva, & Novo, 2016). The temporal segmentation analysis of the time-domain provides meaningful information to capture diverse land cover dynamics, and the use of regression-based trajectory allows to detect abrupt changes and more prolonged forest disturbances such as ASGM activities (Kennedy et al., 2010). Moreover, because a temporal trajectory pattern is allowable, the characterization of the magnitude of change and the timing of change is extracted and used as a predictor in the ASGM monitoring.

1.1.7 Spatial Relations Analysis by Texture image extraction

The texture is an essential spatial feature of an image for pattern recognition, spatial analysis among land classes, and visual interpretation (Kupidura, 2019). Remote sensing literature has proven the usability of these characteristics to retrieve visually similar patterns and establish spatial relations in a specific window of analysis (Clausi & Zhao, 2002). Texture in image analysis is a distinctive feature for every object that assesses the spatial relationships of the object in a geographic space with its surroundings. Besides, texture analysis features are often used as complementary information, particularly in applications where similar land classes are not separable using just the spectral information (Ramola, Shakya, & Van Pham, 2020). What is more, the use of texture for detecting specific targets and mapping LULC change can be extended to (Conners, Trivedi, & Harlow, 1984), (N. Li et al., 2014)(Horch et al., 2019).

Image texture can be retrieved from a gray-level Co-Occurrence matrix (GLCM), a metric used to characterize LULC classes and category-identification of objects regions of particular interest on an image, proposed by Haralick et al. (1973). A total of 14 different texture features based on grey-level or single image-based spatial dependencies of pixels were proposed to identifying objects or regions of interest in an image. Additionally, some other texture features have been used as input in the segmentation process of differentiated uniform regions from the boundary and unspecified regions, such as the proposed by Conners et al. (1984). This research used the GLCM, which has been widely accepted for vegetation modeling and classification purposes (Jin et al., 2018)

1.1.8 Incorporating Ancillary Data for Problem Context

According to F. de L. Lobo et al. (2018), some infrastructures such as ports, airstrips, and access roads should be considered in LULC classification since directly associated with ASGM activities. Ancillary data such as topographic data derived from digital elevation models, LULC maps, or infrastructure information is incorporated into multifeatured remote sensing analysis since spectral-radiometric data cannot always discriminate land-cover classes in their entirety (Rogan et al., 2003). It also helps contextualize the phenomenon by increasing detailed thematic levels of land-cover change (Wasige et al., 2012). Additionally, remote sensing analysis must undergo processing that incorporates other data sources for interpretation and final

consideration in differentiating significant from non-significant change (Corcoran, Knight, & Gallant, 2013a).

Ancillary topographic and soil data derivatives are the most significant input variables for mapping wetlands and classifying vegetation wetland types (Corcoran et al., 2013a). Topographic characteristics such as a slope, aspect, or altitude determine the spatial distribution of the LULC and complement the description of the target with meaningful context (Lersch et al., 2007), (Szantoi et al., 2013) demonstrated the significance of using digital elevation model and land use map as ancillary data for classifying riparian vegetation in the forest.

1.1.9 Random Forest in the Classification Process

Random Forest (hereafter RF) is a machine learning supervised classification technique that is based on the aggregation of a large number of independent and unrelated decision trees (Corcoran et al., 2013) under the premise that the combination of many trees is often more accurate than to depend on just one tree. Compared with other traditional automatic classification algorithms such as MLC (e.g. maximum likelihood classification) and SVM (e.g. support vector machine), the information dimension of RF processing can be increasingly complex in terms of size, structure, and type (Hu & Hu, 2020). It is usually trained with the "Bootstrapping" method, a sampling technique in which the algorithm randomly draws samples with replacement about two-thirds of the data set (i.e., in-bag samples) for training purposes. The remaining third part (i.e., out-of-the-bag) is used for performance assessment of the model, simulating the concept of k-fold cross-validation in the set of multiple trees with replacement. This training method implies that the same sample can be selected several times, while others might not be selected at all. The estimation Error is called OOB-Error is the average error for each prediction from the trees that were not contained in the bootstrapping sample; it is also an indicator of the model performance. The final classification decision is made by taking the most popular voted class from all the tree predictors in the forest (Belgiu & Drăgu, 2016). The RF has been widely used in remote sensing for both regression and classification purposes. The model's architecture based on multiple trees and random sampling creates high variance and low correlation, representing a notable advantage to avoid overfitting issues (Touw et al., 2013).

The RF is a versatile algorithm with high prediction accuracy and provides meaningful information about variable importance, allowing assess variable interaction and relationships (Touw et al., 2013). Variable importance helps interpret the relevance of variables for the data set under study, showing a direct link between predictors and samples and optimizing prediction accuracy (Belgiu & Drăgu, 2016). The main reason for choosing RF as a machine learning method for classification purposes compared with other classifiers is that RF is intrinsically suited for multiclass and multitype type data problems, allowing assessment features with different scales (Corcoran et al., 2013).

1.1.10 Problem Statement

Through the Intergovernmental Negotiating Committee on Mercury (UNEP, 2014), United Nations Environment Program emphasized the need for a cost-efficient monitoring technology for ASGM and reducing mercury emissions in a forest management context (UNEP, 2014). Moreover, it is a priority research problem unanimously identified by the local governments, land managers, and social scientists from the Amazon countries to assess the state of the ASGM (Hinton, 2006). Current methods of identifying ASGM are resource-intensive (Eduful et al., 2020) (surveys and military campaigns) and the remote sensing methods employed failed in separating the ASGM above similar spectral classes, omitting the spatial context and relations in detecting the dynamic process of the ASGM (F. Lobo et al., 2016a), (Isidro et al., 2017). Additionally, ASGM detection approaches by (Elmes et al., 2014) recognizes inaccurate boundary delimitation by exploiting the spectral features derived from satellite images.

As Kupidura (2019) shows, texture refers to the visual effect caused by the spatial variations in tonal quantity in a specific area, providing information regarding pattern and local variations (Shaban & Dikshit, 2001) assures that statistical textural information results useful for classifying heterogeneous classes with similar spectral properties and boundaries delimitation. Additionally, (Champion et al., 2008), (Feng, Liu, & Gong, 2015), (Small, 2001) have found that using textural information in multispectral images for classification, apart from spectral data, can significantly increase the accuracy of classification.

On the other hand, time series by spectral segmentation provides the ability to determine the drivers of the land cover change and estimate the magnitude and year of detection (Cohen et al., 2018), using vegetation indices as an efficient way to provide a direct connection to vegetation's physical characteristics and the land cover change (Dash et al., 2007). Moreover, approaches that incorporate spatial, spectral, and temporal data of the classes of interest are prone to comprehend the phenomenon better and, therefore, better detect the ASGM (Gómez et al., 2016).

Consequently, to the knowledge of this research, incorporating a multifeatured (textural, spectral, and ancillary) and multitemporal analysis (LandTrendr time series) for ASGM detection is the core of the current scope. The study focuses on characterizing the magnitude of changes of spectral and texture features by using the LandTrendr algorithm adding ancillary data for ASGM detection. Since temporal segmentation enables describing the temporal changes in a time series, texture represents patterns in pixels and spatial variations that spectral values cannot describe (Feng et al., 2015); this study, therefore, aims to address the research gap by characterization the textural with spectral features through temporal segmentation using the LandTrendr algorithm, combining with ancillary data, to assess the textural and spectral changes through time to identify ASGM in the Amazon Rainforest.

1.2 Research Objectives

The current research aims to detect and monitor ASGM in the Amazon Rainforest by incorporating multisource features and multitemporal image time series analysis in the period cover by 2000-2019.

Based on the above discussion and reasoning, the main research aim of the proposed study is:

- To detect ASGM through LandTrendr for temporal segmentation on time series using multispectral and textural features on the Random Forest classifier.

To achieve this primary aim, the specific objectives of the study are as follow:

1.2.1 Specific Objectives

1. To perform temporal segmentation of texture features and spectral indices using the LandTrendr algorithm to assess the magnitude of the change and add ancillary data for ASGM detection.
2. To perform data mining to assess the most relevant and least redundant features in the ASGM detection and classification process.
3. To develop an accurate and efficient classification method (probabilistic) using the relevant spectral characteristics and textural features derived from temporal segmentation and ancillary data.

1.2.2 Research Question

Several research questions were formulated to address the objectives:

1. Does the LandTrendr, through temporal segmentation of multispectral and textural features in a time series, detect abrupt changes related to ASGM activities?
2. What is the most relevant set of textural, spectral, and ancillary features retrieved for data mining for classification purposes?
3. Is the ASGM detectable by exploiting the temporal segmentation of textural and spectral features?

2. STUDY AREA AND DATA USED

2.1 Study Area

The Tapajós River Basin is one of the largest tributaries of the Amazon river (Ngom et al., 2020). It is 2.080 km long and covers 492.000 km² approximately (Ngom et al., 2020). The area has a monomodal flood-pulse, with a high-water period from February to May and a low-water period from August to November (Domingues et al., 2019). More than 95 percent of the Tapajós Basin is divided between Mato Grosso and Pará states, with the states of Amazonas and Rondônia skirting the western drainage. The area is well known for creating the Gold Mining district in 1983, and the area has been intensively mining since then (F. L. Lobo et al., 2015).

The area of study spans 370km². It is located in the south of Pará state and the downstream part of the Tapajós River (figure 1). The area of interest is delimited by the spatial coverage of a Landsat scene located in the row and path 228-64.

Figure 1 Shows the area of interest (AoI)¹, the official land cover map for the whole Tapajós river basin considering the Forest/No Forest classes retrieved from the *mapbiomas* platform which belongs to the project: Brazil annual mapping of land use and land cover project (Mapbiomas, 2015). The other inputs were obtained from Instituto Brasileiro de Geologia e Estadística (IBGE, Brazil) and the Agência Nacional de Águas e Saneamento Básico (ANA).

According to F.L Lobo et al. (2015), gold mining in the area is traditionally performed by removing topsoil layers or dragging out the sediments from the bottom of the rivers using suction and separating the gold by gravity. Both techniques discharge a high concentration of sediments, composed chiefly of fine organic particles that carry out a significant concentration of Mercury used in the amalgamation process (Telmer & Stapper, 2007). The Tapajós river basin was intensively explored during the gold rush in late 1980. Since then, it has been exploited for the last 30 years (Roulet et al., 2001), releasing significant amounts of Mercury into its water tributaries, notably the Peixoto de Azevedo, Teles Pires, Juruena, Tropas, and Crepuri (Malm et al., 1995).

¹ Given that the aim of this research is to assess the accuracy and performance of a potential method for detecting ASGM. Therefore just a small area from the Tapajós river basin was selected.

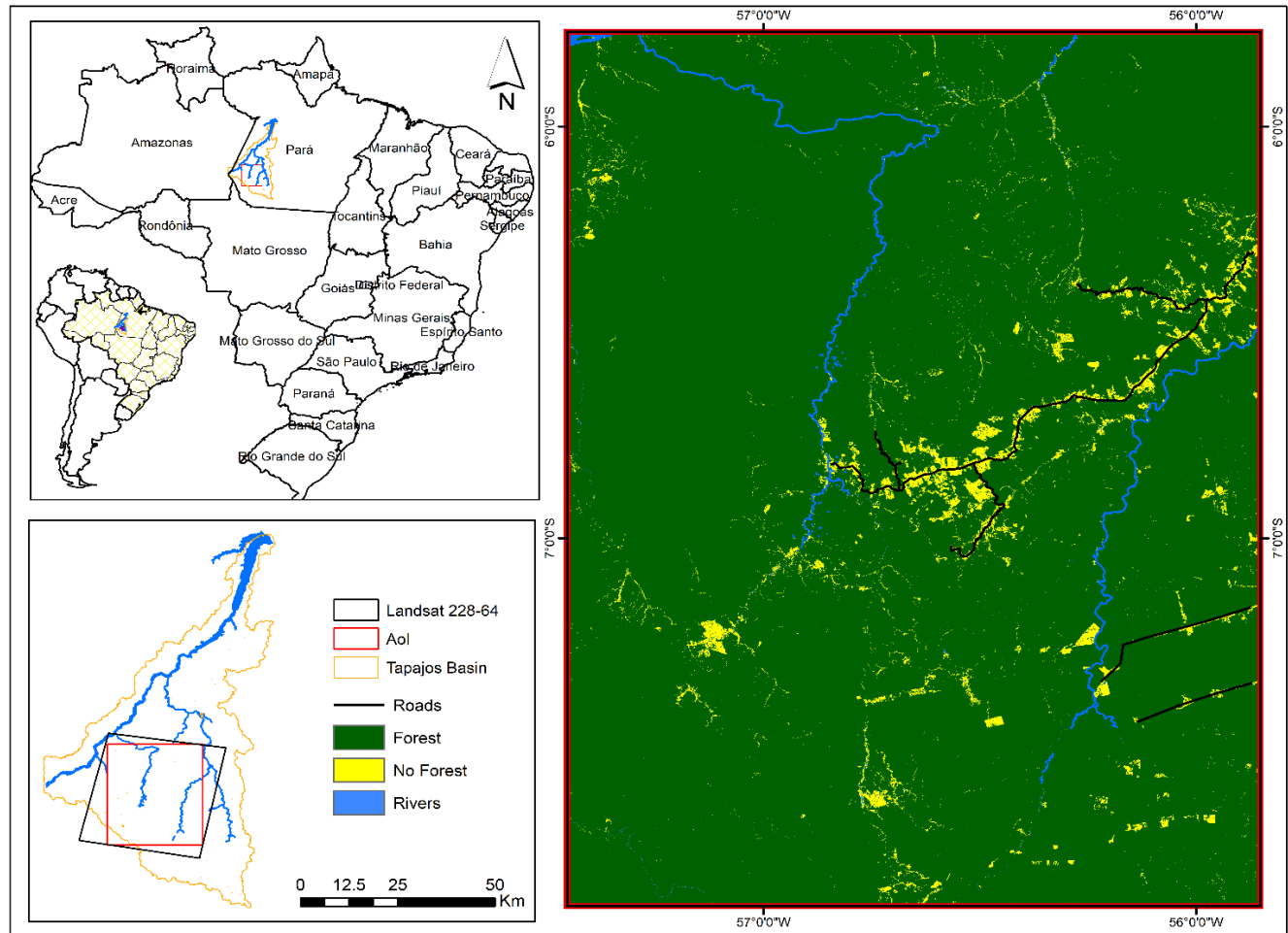


Figure 1 Area of Interest. (a) Top Left: Brazilian Federate States and Tapajós Basin Location. (b) Bottom Left: Area of Interest at the Tapajós River Basin. (c) Forest / No-Forest map of the Area of Interest

2.2 Dataset used.

This section describes the data used in this research. Table 1 shows a summary of every set of data. A detailed description of every feature can be found below.

Table 1. Dataset Used

DATASET	SOURCE	FORMAT	DATA PROVIDER
ASGM Data	RAISG	.shp	(RAISG, 2020)
Landsat 7 ETM+	Google Earth Engine	.GeoTiff	(Department of the Interior U.S. Geological Survey, 2011)
Landsat 8 OLI	Google Earth Engine	.GeoTiff	(Department of the Interior U.S. Geological Survey, 2016)
NASA SRTM Digital Elevation 30m	Google Earth Engine	. GeoTiff	(Farr et al., 2007)
Water Bodies and Roads	IBGE (Instituto Brasileiro de Geografia e Estadística)	.shp	(IBGE, 2020)
VHR Images	Google Earth	Cloud Computed Base	(Google, 2019)

2.3 ASGM Dataset

The ASGM dataset is second-hand data formed as a compendium of multiple considerable types of research, methodologies, institutes, and sources. It ranges from anthropological studies, hydrological research, remote sensing findings, military campaigns, journal, and research articles, where the location and identification of the ASGM mines were settled by in field. The compendium is part of the agreement by multiple institutions and organizations and their efforts for sharing and broadcast information regarding environmental and social issues in the Amazon Forest. It is compiled by RAISG (e.g., Rede Amazônica de Informação Socioambiental / Socioenvironmental Information Amazon Network), which is a consortium of civil society organizations in the Amazon countries. It is supported by international partners such as Rain Forest, USAID (United States Agency for International Development), NICFI (Norway's International Climate and Forest Initiative) concerned with the socio-environmental sustainability of Amazon. The organization produces and disseminates knowledge, statistical data, and geospatial socio-environmental information on Amazon developed through protocols common to all the region's countries (RAISG, 2020).

The dataset is a compilation of more than a decade of research above the Amazon Forest. The following institutions and programs were responsible for capturing information with regards to the Area of Interest.

- Data bank Protected Areas Monitoring Program / ISA, 2016
- Database of the Binational Brazil Venezuela map, referring to the Brazilian part.
- DETER / INPE (Instituto Nacional de Pesquisas Espaciais): Mapeamento de áreas de garimpo 2017 (Mapping of mining Areas)
- Data base of the Xingu (Observatório do Xingu) / ISA Program, 2013.

In table 2, there is a description of the RAISG's data set used. Given that data acquisition depends on the type of the study, source, and data owner, there are two sorts of data in the area of interest: Punctual location and Area delimitation. Additionally, from the whole set, only gold mines (mineral substance) were considered in further analysis, and the data field was measured after the year 2000 since it is the first year of the time series.

Table 2. RAISG's Ground Truth data description

DATA	ATTRIBUTES	ELEMENTS	FORMAT	GEOMETRY
Punctual ASGM	Location (X, Y) Coordinates Spatial Reference Country Mineral (Substance) Date (detection) Source of the Information Condition (Active / Inactive) Institute Involve	516	.shp	Point
Set of ASGM's	Location (X, Y) Coordinates Spatial Reference Country Mineral (Substance) Date (detection) Source of the Information Condition (Active/Inactive) Institute Involve Area	182	.shp	Polygon

2.4 Landsat Satellite Images Landsat 7 ETM + and Landsat 8 OLI

The Landsat satellite missions provide multispectral imagery with 30m spatial resolution since April 1972 and onwards (P. Li, Jiang, & Feng, 2013). The constellations Landsat-7 ETM+ y Landsat-8 OLI were used in the time series to cover the twenty years. Both satellite constellations orbit the Earth in a sun-synchronous, near-polar orbit altitude of 705 km with circles around the Earth every 99 minutes. The satellites have a 16-day repeat cycle and are freely accessible from different sites such as the USGS website and Google Earth Engine Platform. Given the extended period of analysis and the need for an automated process in the ASGM detection, all the images were processed using a Google Earth engine script. In total, 820 images from Landsat-7 ETM + and Landsat-8 OLI were used for the set of images to cover the period.

Some Landsat specifications of both sensors are given as follows:

Table 3 Landsat sensor characteristics

Satellite	LANDSAT-7 ETM+ Wavelength (μm)	LANDSAT-8 OLI Wavelength (μm)
Band 1	0.45 – 0.52	0.43 – 0.45
Band 2	0.52 – 0.60	0.45 – 0.51
Band 3	0.63 – 0.69	0.53 – 0.59
Band 4	0.77 – 0.90	0.64 – 0.67
Band 5	1.55 – 1.75	0.85 – 0.88
Band 6	10.40 – 12.50	1.57 – 1.65
Band 7	2.08 – 2.35	2.11 – 2.29
Band 8	0.52 – 0.90	0.50 – 0.68
Band 9	-----	1.36 – 1.38
Ground Sampling Interval (Pixel Size)	30m reflective 60m Thermal	30m reflective 15 m Panchromatic
Product delivered as	8-bits with 256 gray levels	12-bits with 4096 gray levels

2.5 NASA SRTM Digital Elevation

The Shuttle Radar Topography Mission digital elevation data (SRTM) is an international research effort that obtained digital elevation models on a near-global scale. NASA JPL provides this SRTM V3 product (SRTM Plus). It used dual radar antennas to acquire interferometric radar data, processed to digital topographic data at one arcsec resolution, approximately 30m of spatial resolution to the year 2000. SRTM uses two synthetic aperture radars, a C band system (5.6 cm, C radar) and an X band system (3.1 cm, X radar) (Farr et al., 2007). These swaths offered nearly continuous coverage at higher latitude. The DEM-based elevation data has been further used for derived topographic image features such as aspect, slope, elevation, and topographic wetness index.

2.6 Roads and Water Bodies

In order to provide context and association with some infrastructures related to ASGM activities, some ancillary data were calculated, such as Euclidean distance to roads and water bodies, using the data set of roads and water bodies in the AOI. The data set was downloaded from the Brazilian National Institute of Statistics and Geography (O Instituto Brasileiro de Geografia e Estadística). Given the conditions of the landscape and the forest density, the roads are the type of tertiary beams and rural roadbuilding. The water bodies include all the river streams of the Tapajós river basin.

3 METHODOLOGY

This chapter describes the overall flow and the further steps to achieve the research objectives and provide findings to the research question. The figure at the bottom represents the methodology flowchart of the whole process in the research.

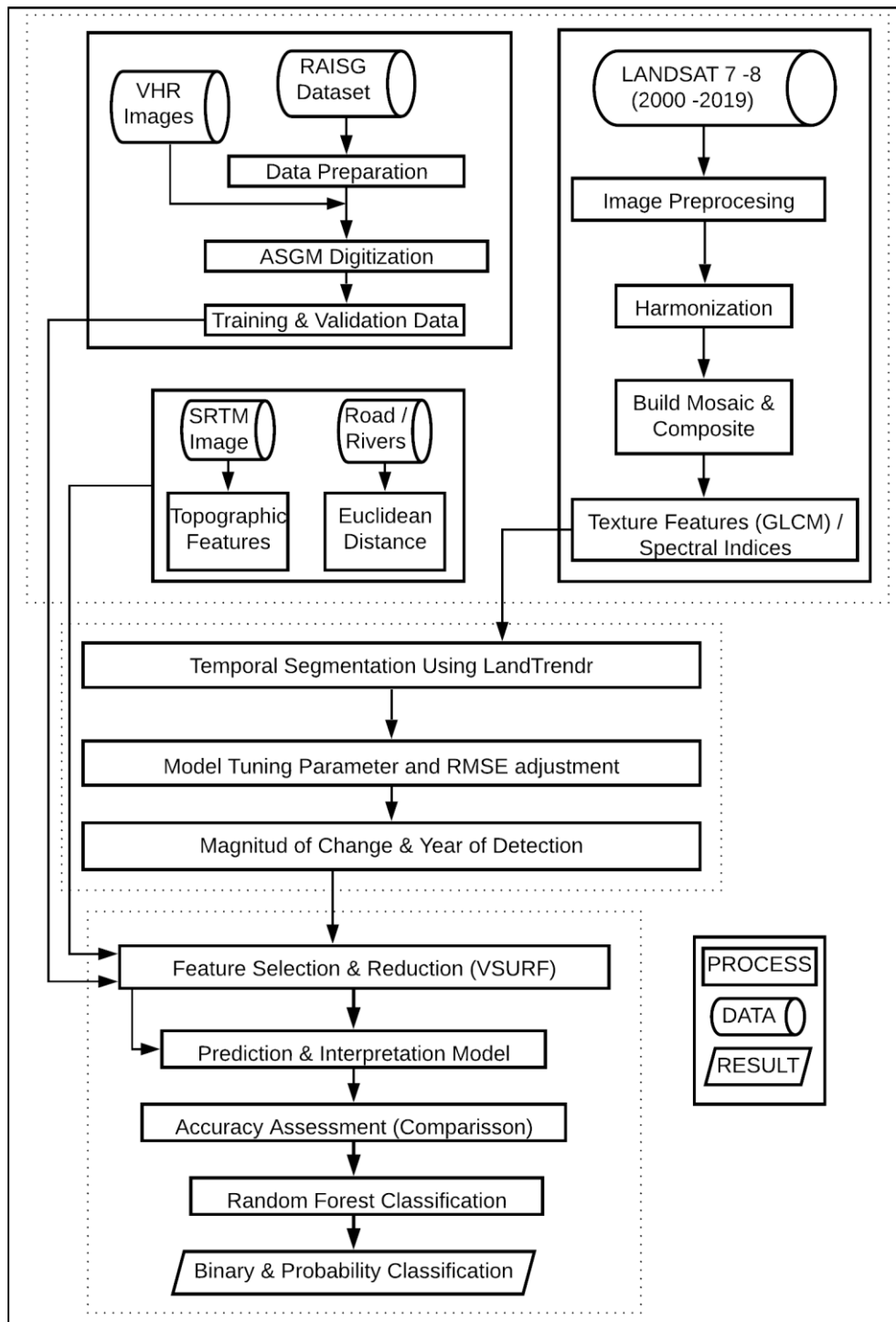


Figure 2. Methodology Flowchart

The research is composed of the third mains stages, as shown in the previous flowchart. Firstly, a pre-processing stage called *Data Preparation* where ASGM data compendium is organized a filtered by area of interest, year of identification (2000 -2019), and type of mine (ASGM). A photo interpretation process is employed for ASGM delimitation. From the ASGM polygons, a set of points were randomly selected and used for classification purposes (75% for training and 25% for validation). An unbalanced data limitation was overcome using an over-sampling on the ASGM polygons and an under-sampling process out of the ASGM areas. Moreover, Landsat images - L2Cproduct atmospherically corrected - are filtered by date and cloudiness conditions and composited. A set of texture features and spectral indices (table 5, 6) were calculated from the image composition and prepared as inputs of the time series analysis from the image collection. Besides, the ancillary data is generated in this step.

The second stage is *Running LandTrendr*, where the time-series algorithm is run using the texture features and the spectral indices to identify and retrieve the temporal breakpoints, the magnitude of change (MAG), year of change (YOD) as raster outputs from forest disturbances. A total of 80 variables were used for temporal segmentation, 72 texture features (table 5), and 8 spectral indices. Ancillary data, given their nature, was not included in the segmentation, and was directly used in the following phase.

Thirdly, the *Classification* stage was conducted in two steps: feature reduction by variable importance assessment using the package VSURF, and a binary and probabilistic classification using Random Forest Classifier. The assessment of the variable importance was performed to reduce the set of predictors in classification and identify what features are important in ASGM classification. A final prediction model was resultant after VSURF with 33 features (table 11). Additionally, a set of partial dependence plots was generated to analyze the features' influence on ASGM classification individually.

The following subsections explain in detail the process carried on for every step.

3.1 Data Preparation

The ASGM second-hand dataset comprises different types of sampling, methods, period, and accuracy. Therefore, an additional adjustment of the dataset was needed. Initially, it was filtered by mineral and year in the area of interest. Subsequently, the polygons were digitized based on the location, and the definition of the boundaries was delineated considering the routinely essential elements of image interpretation and aerial photos image analysis (e.g., location, size, shape, shadow, tone/color, texture, pattern, site/situation/association). The digitization was carried on using different very high spatial resolution images in Google Earth considering the period of analysis and data collection date (2000-2019). Those polygons were used for sampling the validation and training samples. The third quarter of the sampling was used for training, and the remaining part for validation. In the following section, there is a description in detail and explanation of the sampling process and the limitations of the size sampling and land classes' nature. Figure 3 shows an ASGM digitized and the location in the area of interest.



Figure 3. Area of Interest and ASGM digitized example date: 12-2001, image: Landsat / Copernicus Google Earth Pro

3.1.1 Unbalanced Data

Unbalanced data refers to the classification problem where the classes are not represented equally, posing a problem for the suitable performance of the machine learning algorithms, particularly with unbalance predictor classes (Riddell et al., 2020). The unbalanced data restriction is expected under the conditions and characteristics of this environmental problem, the target class size, the informality related to this activity, the spread pattern by small clusters, the restrictions presented for field work, and the extension of this activity in the rainforest. According to (Millard & Richardson, 2015), an adequately alternative to deal with the unbalance data is using a combination of under-sampling and over-sampling of the major and lesser classes, respectively. For under-sampling, a subset of samples was selected randomly from the class with more instances (i.e., forest and water bodies). On the latter, there is an additional and intense sampling of the minor class to increase the number of samples and thus mitigate the difference among the classes.

Nevertheless, it is essential to consider some drawbacks that the combination of both methods might arise. On the one hand, the main disadvantage of under-sampling is likely to lose valuable and relevant information from the left-out samples. On the other hand, over-sampling may lead to overfitting the model and make the classification prone to get the same samples in the test and training data, leading to overestimating the model and its poor generalization.

The random sampling of the mine class was carried over the ASGM polygons generated in the digitization step “*Data Preparation*” section. The Non-mine class was also randomly sampled but over the rest of the land covers present in the study area (i.e., forest, crops, roads, and rivers). Finally, three-quarters of the entire set of samples were used for model validation; the remaining samples were used for training purposes—figure 3 shows the whole sampling dataset and distribution.

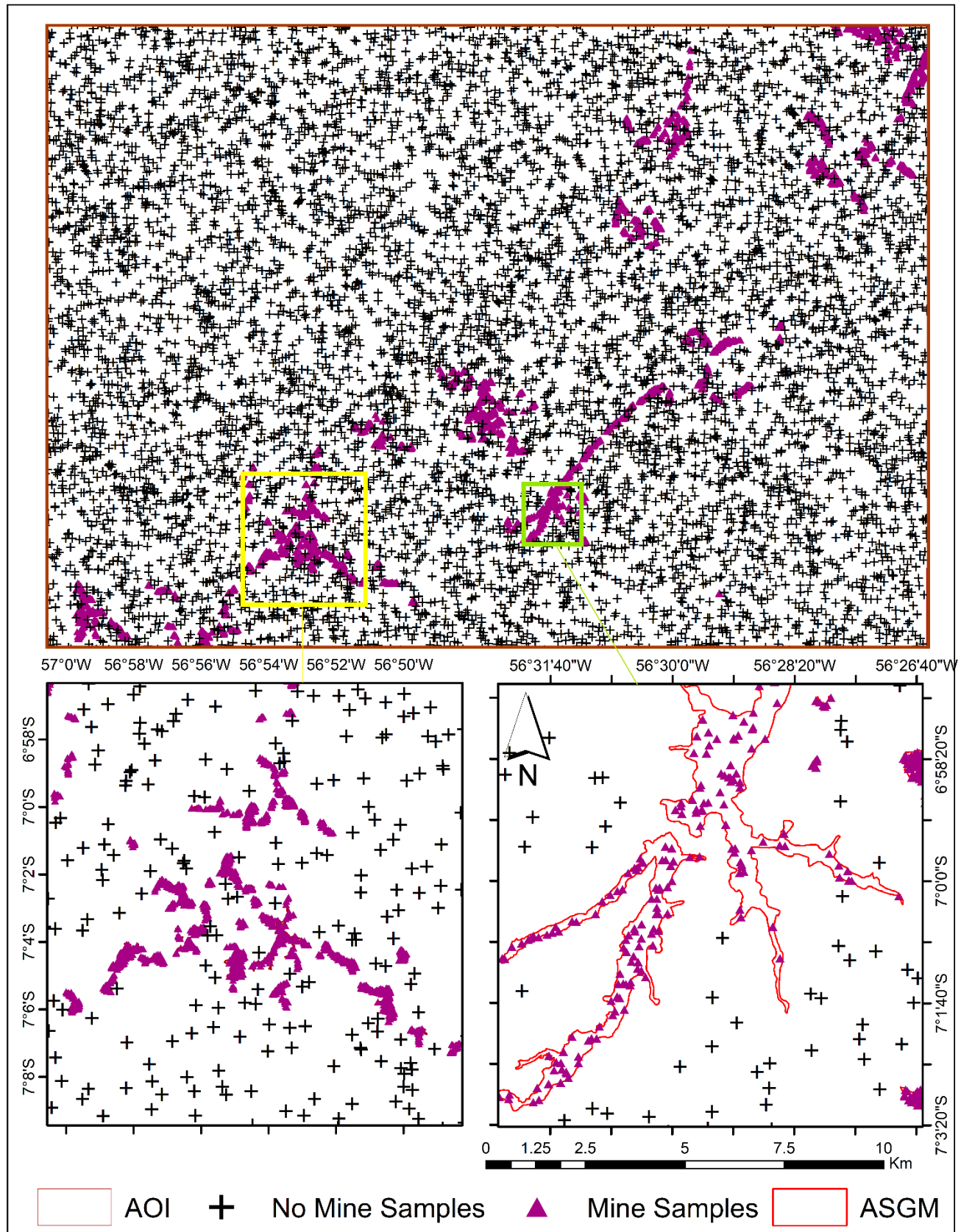


Figure 4. Sampling Schema for Mine and Non-Mine Classes

3.1.2 Image Pre-Processing and Harmonization

The selection of the satellite images and the posterior processing ran into LandTrendr was carried on the Google Earth Engine platform. The Landsat 7 ETM+ and Landsat 8 OLI images were selected based on the Landsat row-path (228-64), a cloudiness factor lower than 20%, and over the dates in the dry period (June to September (F. L. Lobo et al., 2015)). Nevertheless, given the extended period of analysis (twenty years) it is needed to combine and relate spectral information of both sensors to assure the spectral continuity of the time series through the period (2000-2019), generate near-date intra-annual images composition, reduce the effect of missing observations either the sensor ETM+ SLC-off or clouds and shadows and increase the observation frequency (Vogeler et al., 2018). Making comparable sensor bands and spectral values from one sensor to another and ensuring the Landsat images' continuity in the time series is called *harmonization*. According to Roy et al. (2016), harmonized ETM / ETM+ / OLI can minimize and link the differences between the sensors regarding the spectral wavelength and wideband, time of acquisition, and atmospheric state. The harmonization used in this research is a pixel basis method presented by Roy et al. (2016), using a linear transformation of the Landsat 7 ETM+ spectral space to link with the Landsat 8 OLI spectral space. Table 3 shows the coefficients and slope proposed in the method and the regression used for harmonization from ETM+ to OLI, the wideband of the resultant band, and the name assigned to each one. Figure 5 illustrates the images available in the time series for each sensor using the NDVI as an example for representation. Additionally, a single-pixel spectral response time series chart using the same vegetation index composite by median to represent the Landsat ETM+ harmonization to OLI by a linear transformation (figure 6).

The transformation functions were developed using ordinary least squares (OLS) regression. The different models had good fits for every band (r^2 values > 0.7 , p-values < 0.0001), indicating that spectral transformations can be applied to broadly normalize the reflectance of one sensor with the other (Roy et al., 2016). Table 4 shows the transformation functions applied to every band and the band's name resultant after the harmonization process.

Table 4. Harmonization Surface Reflectance Sensor Transformation Functions based

Band (Name)	OLI (μm)	ETM+ (μm)	Linear Transformation Function	Wavelength After transformation (μm)	Band Name After Transformation
Blue	0.45 – 0.51	0.45 – 0.52	$\text{OLI} = -0.0095 + 0.9785 \text{ ETM+}$	~0.48	B1
Green	0.53 – 0.59	0.52 – 0.60	$\text{OLI} = -0.0016 + 0.9542 \text{ ETM+}$	~0.56	B2
Red	0.64 – 0.67	0.63 – 0.69	$\text{OLI} = -0.0022 + 0.9825 \text{ ETM+}$	~0.66	B3
NIR	0.85 – 0.88	0.77 – 0.90	$\text{OLI} = -0.0021 + 1.0073 \text{ ETM+}$	~0.85	B4
SWIR 1	1.57 – 1.65	1.55 – 1.75	$\text{OLI} = -0.0030 + 1.0171 \text{ ETM+}$	~1.61	B5
SWIR 2	2.11 – 2.29	2.09 – 2.35	$\text{OLI} = 0.0029 + 0.9949 \text{ ETM+}$	~2.21	B7

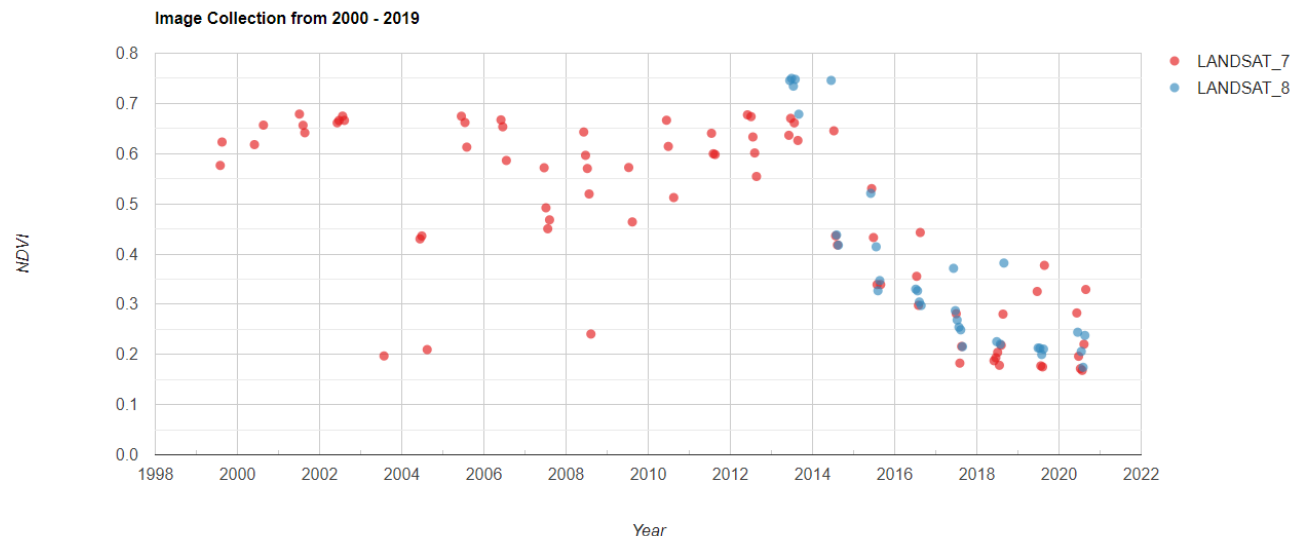


Figure 5. Time Series Image Collection using harmonization and NDVI.

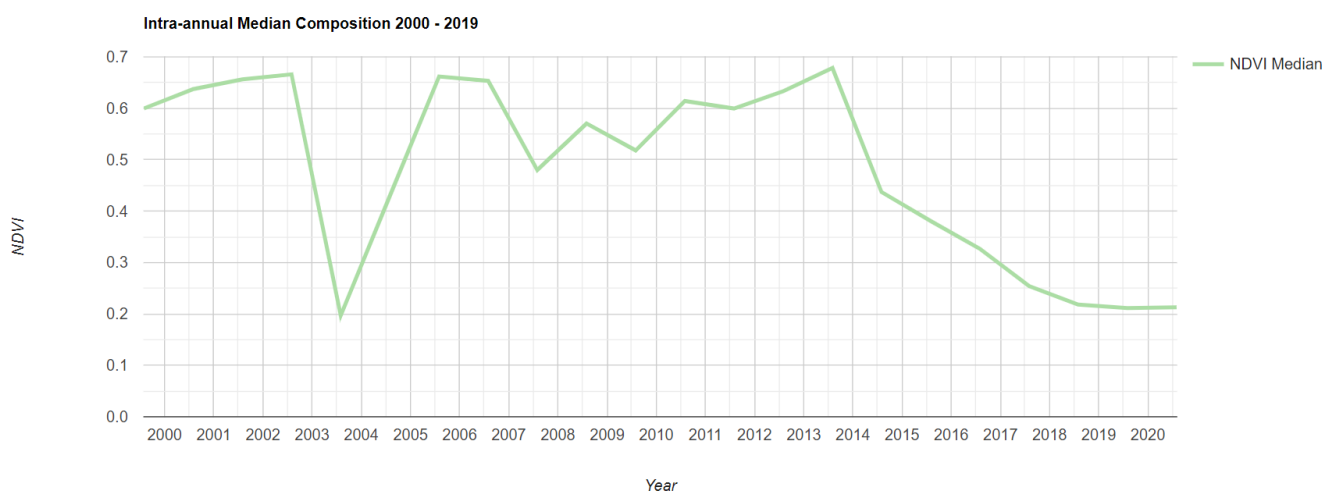


Figure 6. NDVI Median Composite time-series images harmonized to Landsat 8 OLI.

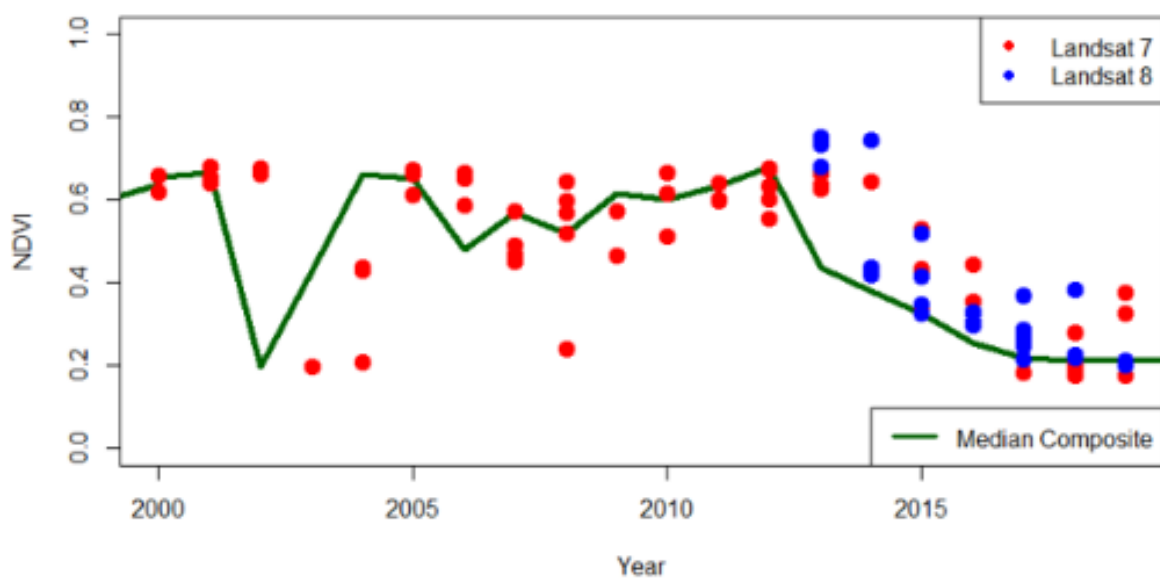


Figure 7. Harmonization and Image composite using medoid and NDVI as an example.

The image collection set formed after the Harmonization process and composited by medoid is hereafter called "*Sensor Collection*" for simplicity and clarity with the terms. Remarkably, this collection has only six bands due to the harmonization process from ETM+ to OLI. The wideband resultant is the arithmetical average of the wavelength inputs and the band's name as render in the previous table (table 4).

3.1.3 Cloud Masking and Mosaic Composition

Identification of clouds, cloud shadows, and snow in optical images is often necessary to reduce noise that can effect the trend analysis and thus the outcome (Jensen, 1996). The sensor collection has been atmospherically corrected and includes a cloud, shadow, water, and snow mask produced by the CFMASK function available in Google Earth Engine. This function was used considering that the harmonization process was employed to adjust the spectral values from Landsat 7 ETM+ over Landsat 8 OLI, which means that the spectral information for further analysis is related to the second sensor. The new version of the mask function for use with Landsat-8 OLI takes advantage of the *cirrus* band and is especially helpful for detecting high altitude clouds, returning the count of unmasked pixels per year available for compositing. Additionally, the quality assessment band (QA) provides cirrus confidence information in the mask processing (Zhu & Woodcock, 2014).

The sensor collection must include only one image per year to be accepted by the temporal segmentation algorithm (Cohen et al., 2018). However, because clouds are often present in the tropical forest, it is safe to retrieve multiple images along the dry season, mask the clouds out, cloud shadows from each of them, and posteriorly perform a composite collection (Kennedy et al., 2010). In this sense, it is possible to have an annual spatial coverage free-cloud pixel, and thus the spectral information will not be altered because of non-interested elements. Moreover, according to Lobo et al. (2016), the ASGM activities are prone to be settled in the dry season (June – September), and thus the image collection was performed into this period.

There are multiples options to perform an image composite of satellite images, based on the median (Fauvel et al., 2012), nearest to a target day of the year (Griffiths et al., 2013), maximum NDVI composite or medoid (Jensen, 2015). In order to keep the spectral trajectory along the time with the fewer alterations or modifications in the pre-processing as much as possible, and also, to produce an image collection representing the period (figure 7), the medoid technique was conducted in the research based on Flood (2013).

The medoid is a multi-dimensional analog of the median composition, robust against extreme values (Flood, 2013). For each pixel, the medoid is always selected from the available set of images. The medoid is the value in the whole data set, which minimizes the median distances from all other points. It is selected from the input set of images, assuring that the final pixel value will lie roughly in the midpoint of the cluster, in contrast to average or median values where the output is not necessarily a real pixel value in the data set but calculated (Flood, 2013). Therefore, the result is always a real observation; compare to the median or the average, where the pixel value resultant is estimated. A formal definition of the calculation of medoid is presented in the following equation.

$$\text{Medoid } (X_i) = \operatorname{Arg} \min_{x_i \in X} \sum_{x_j \in X} \|x_i - x_j\|, \text{ where } x_i, x_j \in X \text{ and } (X_i) \subset R^n$$

$$(X_i) = \text{Target pixel}$$

$$R^n = \text{Image dimensions (Bands)}$$

The $\|\ \|$ represents the Euclidean distance, and the *arg min* operator selects the element of X (X_i) That minimizes the expression (Flood, 2013).

The sensor collection has been transformed into an Image composition collection. Every pixel has been atmospherically corrected (dataset is atmospherically corrected -surface reflectance - from the source of origin), masked by the CFMASK function to reduce the noise from clouds and shadows, harmonized using Roy's linear regression and transformation relating the spectral feature space from ETM+ to OLI with six resultant spectral bands and composited by the medoid method. This image composite collection (hereafter *Image Collection*) comprises twenty images per year from 2000 to 2019. The *Image Collection* is the set of images prone to the calculation of texture features and spectral indices, and it is the primary input to run the LandTrendr algorithm and estimate the temporal segmentation. Figure 7 represents the structure of the image collection for the time series analysis.

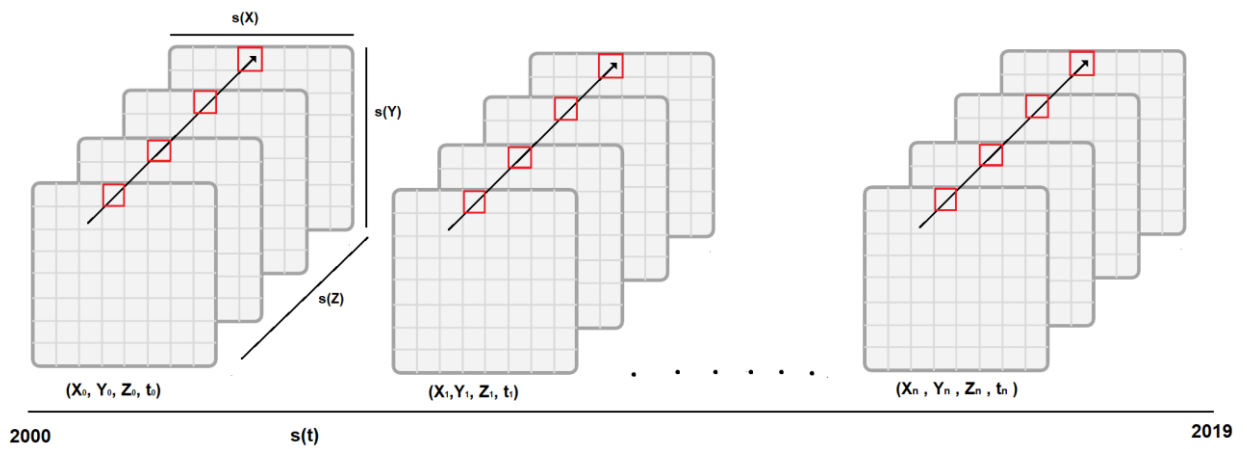


Figure 8 Image Annual-Composition Collection Structure (TrimbleInc, 2015)

Table 5. Inputs Predictors used for Classification.

PREDICTORS	QUANTITY	DETAIL
MAG TEXTURE FEATURES	72 Features	Angular Second Moment Contrast Correlation Variance Inverse Difference Moment Entropy Difference Variance Difference Entropy Cluster Prominence Dissimilarity Inertia Shade
MAG SPECTRAL INDICES	12 texture x 6 spectral Bands	EVI LSWI MNDWI NBR NDMI NDPI NDVI NDWI
ANCILLARY FEATURES	8 Features	Aspect Slope Elevation Distance Roads Distance Rivers TWI
	6 Features	

3.1.4 Texture Feature Extraction

GLCM (i.e., Gray Level of Co-occurrence Matrix) method extracts second-order statistical texture features. A GLCM is a matrix where the number of rows and columns is equal to the number of gray levels in the image (Ramola et al., 2020). The GLCM measures the probability of two grey levels separated by a given distance in a given direction. According to Mohanaiah *et al.* (2013), “the matrix element $P(i, j | \Delta x, \Delta y)$ is the relative frequency with which two pixels, separated by a pixel distance ($\Delta x, \Delta y$), occur within a given neighborhood, one with intensity ‘i’ and the other with intensity ‘j.’ The matrix element $P(i, j | d, \Theta)$ contains the second-order statistical probability values for changes between gray levels ‘i’ and ‘j’ at a particular displacement distanced and at a particular angle (Θ).” Using the texture features in terms of gray intensity levels implies using spatial-temporal relations in the data set, high accurate discrimination in pattern recognition with low computation capacity.

The GLCM texture features extraction was calculated from the Image Collection. A set of nine GLCM metrics proposed by Haralick et al. (1973) and three metrics considering Conners et al. (1984) were generated for each band, year after year, along with the period cover by the time series. The outputs consist of twelve images of texture features per band input (72 bands in total), using a directional averaging kernel of 3 x 3 size. The kernel’s size was established

considering the smaller ASGM at the RAISG data set (1Ha) and the spatial resolution of the Landsat Images (30m). Table 3 shows the Gray Level Co-occurrence Matrix and Conners' metrics features and a brief description of each one. The texture features were estimated using the function *glcmTexture (size, kernel, average)* in Google Earth Engine.

Table 6. Texture Feature Description

TEXTURE	DESCRIPTION
Angular Second Moment	Measures the number of repeated pairs
Contrast	Measures the local contrast of an image
Correlation	Measures the linear dependency between pixels pairs
Variance	Measures the spread of gray-level in an image is in an image
Inverse Difference Moment	Measures the homogeneity of an image
Entropy	Measures the randomness distribution of a gray-level in an image
Difference Variance	Measures the variance of the gray-level distribution in an image
Difference Entropy	Measures the difference in the randomness of the gray-level
Cluster Prominence	Measure cluster by the gray-level occurrence
Dissimilarity	Measures the variation between pixels pairs
Inertia	Measures the intensity between a pixel and its neighborhood
Shade	Measures the cluster shade of gray-level distribution

The texture is the pattern of intensity variations in an image used for improving land cover classification. It provides information from neighboring pixels that are allowed to characterize and identify target objects in the scene. Each texture models different properties of the statistical relationships calculated from a moving kernel in a defined direction. Variance texture measures a pixel's heterogeneity with its neighbors, increasing when the gray-level values differ from their means. It has no spatial frequency; nevertheless, it is an indicator of high contrast values from a set of pixels. Cluster prominence (here called PROM) is an asymmetry measurer. The higher the PROM, the higher the asymmetric is the image; in contrast, low values in the cluster prominence indicate a peak in the mean in the GLCM matrix, thus asymmetric and low grayscale variation image. Cluster shade (here called SHADE) measures the skewness and the uniformity of the grayscale matrix. According to Yang et al. (2012), in the calculation process, a new image is created with a new range of intensities and updated based on its nearby pixel position; high values of shade are related to image asymmetry and, therefore, variation in the gray-level co-occurrence matrix (Ramola et al., 2020). Contrast measures the local variations, showing the difference between the highest and the lowest values of a continuous set of pixels. The higher the image's variation, the higher the contrast value. Inertia is also a local indicator, measuring the contrast between a pixel and its neighbors in terms of pixel intensity in the original image. Correlation indicates the gray-level linear dependency of a pixel with a point in the image; similar gray-level regions register high correlation values. ASGM or angular second moment indicates the textural uniformity of the gray levels; if the matrix contains few gray levels, the ASGM will have high values (X. Yang et al., 2012).

3.1.5 Spectral Indices

Spectral Indices are designed to normalize spectral reflectance for different atmospheric conditions, topography and soil background, which tends to accentuate certain surface properties (Jensen, 1996). They are relatively simple to calculate and are commonly used to monitor vegetation cover, health, state, vigor, and growth dynamics, among others. (Xue & Su, 2017). Moreover, they show better sensitivity than individual raw spectral bands for different applications related to vegetation conditions and constitute a notable method for detecting the LULC changes (Asrar et al., 1985). Additionally, Jovanović et al. (2015) and (1993) have proven that the usability of vegetation indices improves the classifications in thematic mapping considerably, given that each spectral indices are designed to accentuate a particular vegetation or water body's property.

A set of 8 spectral indices were calculated from the *Image Collection* considering the resultant bands after the harmonization process, the indices in table 4 were adapted accordingly to the features of the resultant bands.

Table 7. Spectral Indices used for Spectral Segmentation.

SPECTRAL INDEX	FORMULA	AUTHOR
Enhanced Vegetation Index	$EVI = 2.5 * \frac{(NIR - RED)}{(NIR + 6 * RED - 7.5 * BLUE + 1)}$	(Huete et al., 2002)
Land Surface Water Index	$LSWI = \frac{(SWIR 1 - NIR)}{(SWIR 1 + NIR)}$	(X. Xiao et al., 2002)
Modified Normalized Difference Water Index	$MNDWI = \frac{(GREEN - SWIR)}{(GREEN + SWIR)}$	(Lira, 2006)
Normalized Burn Ratio	$NBR = \frac{(NIR - SWIR 2)}{(NIR + SWIR 2)}$	(Key et al., 2006)
Normalized Difference Moisture Index	$NDMI = \frac{(NIR - SWIR)}{(NIR + SWIR)}$	(Wilson et al., 2002)
Normalized Difference Pond Index	$NDPI = \frac{(SWIR - GREEN)}{(SWIR + GREEN)}$	(Wang et al., 2017)
Normalized Difference Vegetation Index	$NDVI = \frac{(NIR - RED)}{(NIR + RED)}$	(Rouse et al., 1974)
Normalized Difference Water Index	$NDWI = \frac{(GREEN - NIR)}{(GREEN + NIR)}$	(Gao, 1996)

The spectral indices and the texture features extracted from the Image Collection were stacked in a multilayer image that went through the LandTrendr temporal segmentation algorithm to identify the temporal changes and estimate the year of change and the highest magnitude of the change per input feature (band).

3.2 Temporal segmentation using LandTrendr.

The LandTrendr is a spectral trajectory-based algorithm used on time-series analysis to identify and detect vegetation loss or gain changes (Kennedy et al., 2010). It is capable of detecting abrupt and smooth changes and trends from the annual time series. LandTrendr is ported on the Google Earth Engine platform, simplifying the data management and timely processing of the algorithm and taking advantage of the cloud-based processing for less time-consuming and effective monitoring of forest disturbances.

The LandTrendr is a pixel-basis algorithm that enables to characterize a temporal trajectory of a pixel value using a sequence of connected straight segments bounded by break-points or vertices, representing a pixel's yearly behavior in a time series (Kennedy et al., 2018). The temporal segmentation is carried on in two main steps. Initially, some vertices are identified as candidates through iterative anomaly detection to detect break-points (vertices) separating periods of durable change and stability in the spectral trajectory along the time. Once the vertices are detected, a set of straight segments are connected and fitted to the observed spectral values using linear regression to assure that the segment is anchored between two vertices. The best-fitting segment is calculated iteratively to find successively the suitable representation of the time series using a linear regression vertex-to-vertex to identify the best fitting straight line trajectory across the vertices (Cohen et al., 2018). In every iteration, a goodness of fit statistic is estimated to adjust the vertices and segments to the spectral values, and this way, rendering the spectral segmentation. The result of this procedure for each pixel is a fitted trajectory with a set of vertices and segments that provide information about distinct spectral epochs (Kennedy et al., 2010).

The temporal segmentation process is performed considering a set of user-defined parameters that control the number of segments, the best fitting model, and the minimum of the observations needed to perform the output fitting. Table 4 shows the meaning of each parameter, and table 5 the values used for different spectral indices. Moreover, from the temporal segmentation, a set of metrics can be retrieved. Particularly, the duration of change, year of change, and the magnitude of disturbance. Figure 8 renders a temporal segmentation using the LandTrendr for an ASGM pixel in the AoI.

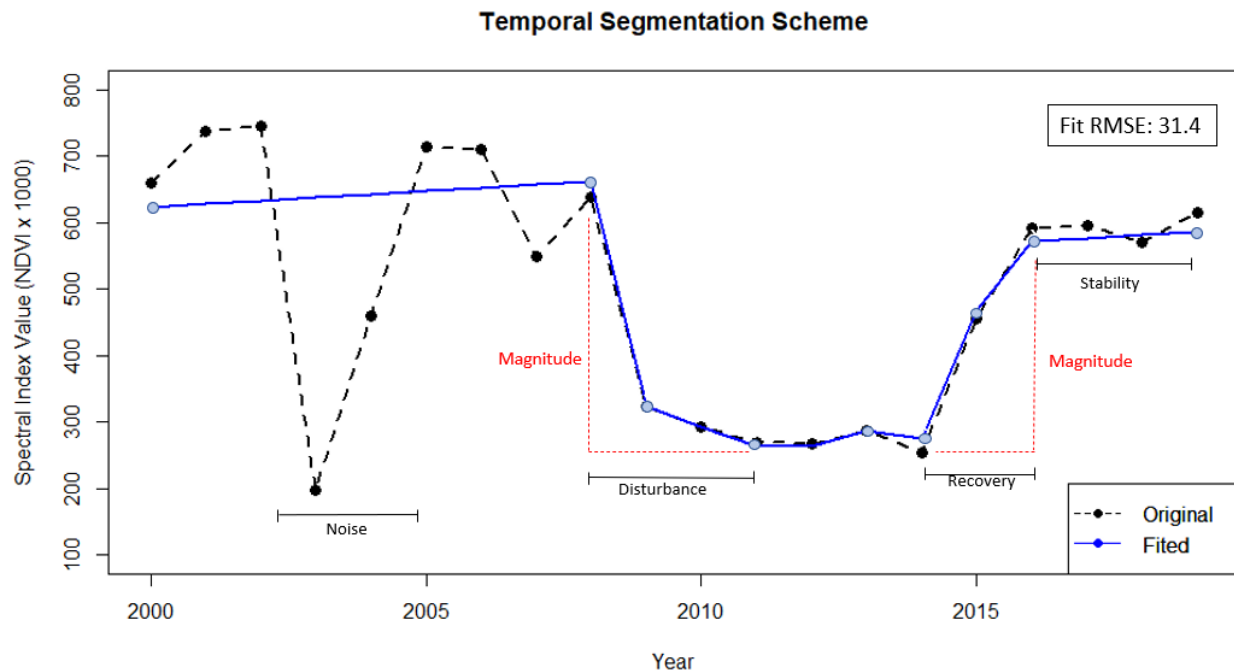


Figure 9. LandTrendr Temporal Segmentation

Figure 8 renders a conceptual model of LandTrendr fitting spectral index using NDVI values to spectral-temporal segments for the Spatio-temporal dynamics using NDVI values. The pixel characterization underwent a forest disturbance, a recovery process, and some stability over the twenty years. The fitted temporal segments (lines) are linked by fitted vertices (points) and sequentially represent the temporal segmentation. From the fitted linear regression is possible to retrieve the magnitude of change (MAG) for forest disturbance and forest recovery, the year of detection (YOD), and the fitted value (RFIT). The magnitude of disturbance is calculated considering the difference among the fitted regression's highest and lowest spectral values and multiplied by (-1), which relates the negative slope as loss of vegetation.

Running the LandTrendr requires three main phases. Firstly, the construction of an annual image collection stacked and composite, atmospherically corrected, and free of noise. Secondly, the tuning of the user-defined parameters model to perform the spectral segmentation and posterior linear regression. It uses the RMSE (Root Mean Square Error) to assess parameters' sensitivity. Finally, extraction of meaningful outputs (e.g., Year of Detection, Magnitude of Change).

3.2.1 Setting Parameter Model and Temporal Segmentation

Temporal segmentation is the milestone concept of the LandTrendr algorithm. Every potential analysis depends on the proper estimation of the parameters and the fitting regression controlled by the RMSE. The LandTrendr requires eight control parameters to perform the spectral, temporal segmentation, and further detection analysis. In the light of achieving a better result, a combination of the algorithm's parameters was used, considering the best fitting with the RMSE value. For parameter estimation, each one's value was modified by one step length every time, while the rest remain constant. The procedure was iterative, parameter by parameter until the RMSE of the fit regression reached the lower value. The linear regression determined the sensitivity of those parameters per spectral input (texture features and spectral indices). The

RMSE indicator assesses the fitness between the temporal segmentation and the spectral trajectory. The lower the RMSE, the higher the linear regression fit and, therefore, the temporal segmentation. Figure 9 shows the temporal segmentation for spectral vegetation indices and the values used in table 5. For the texture parameters used in the LandTrendr see appendix 1.

Table 8. LandTrendr segmentation Parameters (Kennedy et al., 2010).

PARAMETER	TYPE	DETAIL
Max Segments	Integer	Maximum number of segments to be fitted
Spike Threshold	Float	The threshold for dampening the spikes (1.0 means no dampening)
Vertex Count Overshoot	Integer	The initial model can overshoot the max segments + 1 vertices by this
Prevent One-Year Recovery	Boolean	Prevent segments that represent one-year recoveries
Recovery Threshold	Float	If a segment has a recovery rate faster than 1/recoveryThreshold (in years), then the segment is disallowed.
p-value Threshold	Float	If the p-value of the fitted model exceeds this threshold, then the current model is discarded and another one is fitted
Best Model Proportion	Float	Takes the model with most vertices that have a p-value that is at most this proportion away from the model with the lowest p-value
Min Observations Needed	Integer	Min observations needed to perform output fitting

Table 9. Setting Parameters for LandTrendr using Spectral Indices as Input

PARAMETER	NDVI	NBR	NDMI	EVI	NDWI	LSWI	MNDWI	NDPI
Max Segments	9	10	9	9	8	8	9	9
Spike Threshold	0.9	0.6	0.8	0.7	0.9	0.9	0.4	0.1
Vertex Count Overshoot	3	3	3	3	3	3	3	3
Prevent One Year Recovery	True	True						
Recover Threshold	0.5	0.5	0.25	0.25	0.95	0.95	0.65	0.25
Pval. Threshold	0.05	0.05	0.05	0.05	0.05	0.05	0.05	0.05
Best Model Proportion	0.75	0.8	0.75	0.75	0.75	0.75	0.75	0.75
Min Observations Needed	7	8	7	7	6	6	7	7

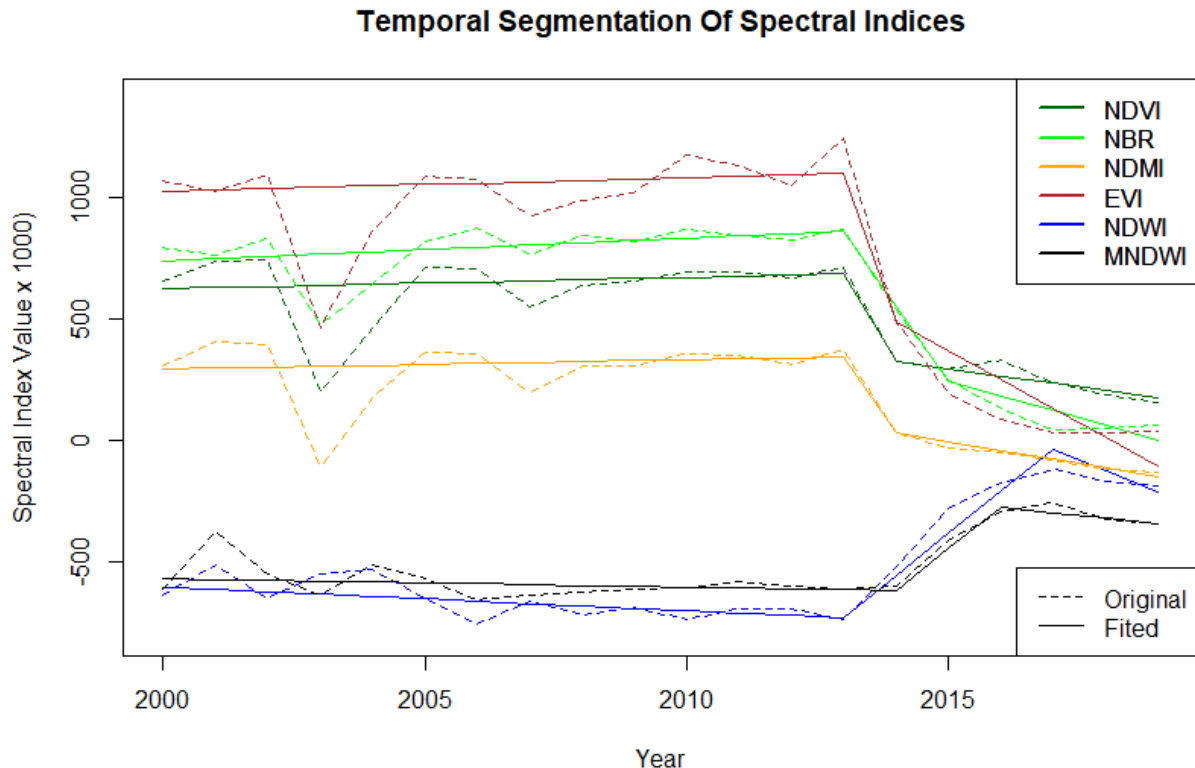


Figure 10. Temporal Segmentation of Spectral Indices

3.2.2 LandTrendr Outputs

The results of GEE-LT are not immediately ready for analysis or used as maps of change detection based on a fitted time series. The LandTrendr's output is conformed by three bands (fig 10). The first band, the LandTrendr band, represents the segmentation process. A pixel array of 4 bands per number of years in the time series requires geometric operations to extract meaningful information. The second band is a raster image with scalar values on a pixel basis that describes the linear regression's adjustment to the spectral trajectory by the RMSE value. The last band explains the fitted annual spectral data by the “fit-to-vertex image data” index. The index has two primary purposes: to fill in data from missing observations in the time series because of cloud masking, cloud shadow, or detector failure. And, to keep consistency in predictive mapping through time, avoiding minor spectral differences from atmosphere or shadows (Kennedy et al., 2018)

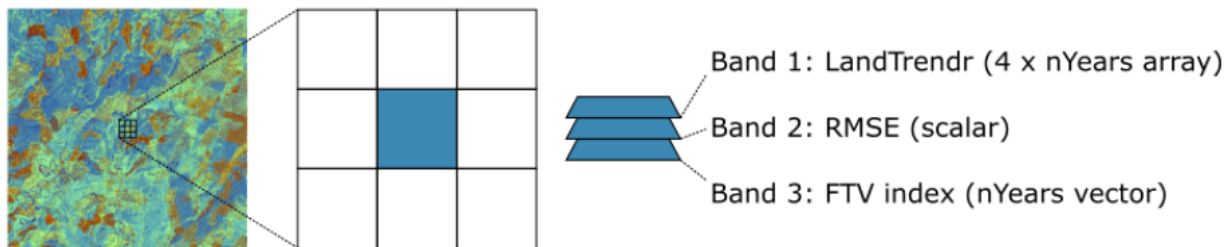


Figure 11. LandTrendr outputs configuration (Cohen et al., 2018)

The LandTrendr band is an array that possesses the primary information of the temporal segmentation process. From this array is possible to retrieve meaningful information related to changes by simple arithmetic and geometric operations. Figure 10 schematizes the array of the LandTrendr band. The values are from the same pixel used in the LandTrendr temporal segmentation (figure 11).

```
[2000,2001,2002,2003,2004,2005,2006,2007,2008,2009,2010,2011,2012,2013,2014,2015,2016,2017,2018,2019]//YEAR
[659,736,745,198,459,713,709,549,638,322,292,269,267,286,254,455,591,595,569,614]// SOURCE VALUE
[623,628,633,637,642,647,652,657,662,322,293,263,263,287,274,466,571,576,581,586]//FITTED VALUE
[1,0,0,0,0,0,1,1,0,1,0,1,1,1,1,0,0,1]// EIRTHER VERTEX (1:Vetex, 0:No Vertex)
```

Figure 12. LandTrendr Array output using NDVI values.

The first array's column contains information about the year of observation, the second row the original spectral value corresponding to the year, the third row is the value fitted to the line using the temporal parameters and the linear regression. The last row identifies if an observation is a vertex or not. Following the methodology and the operations proposed by Cohen *et al.* (2018) & Kennedy *et al.* (2009) for retrieving information and outputs management, it is possible to extract such as year of change, the magnitude of change, disturbance, or recovery values.

Below, you can find some maps representing the magnitude of change and the year of detection.

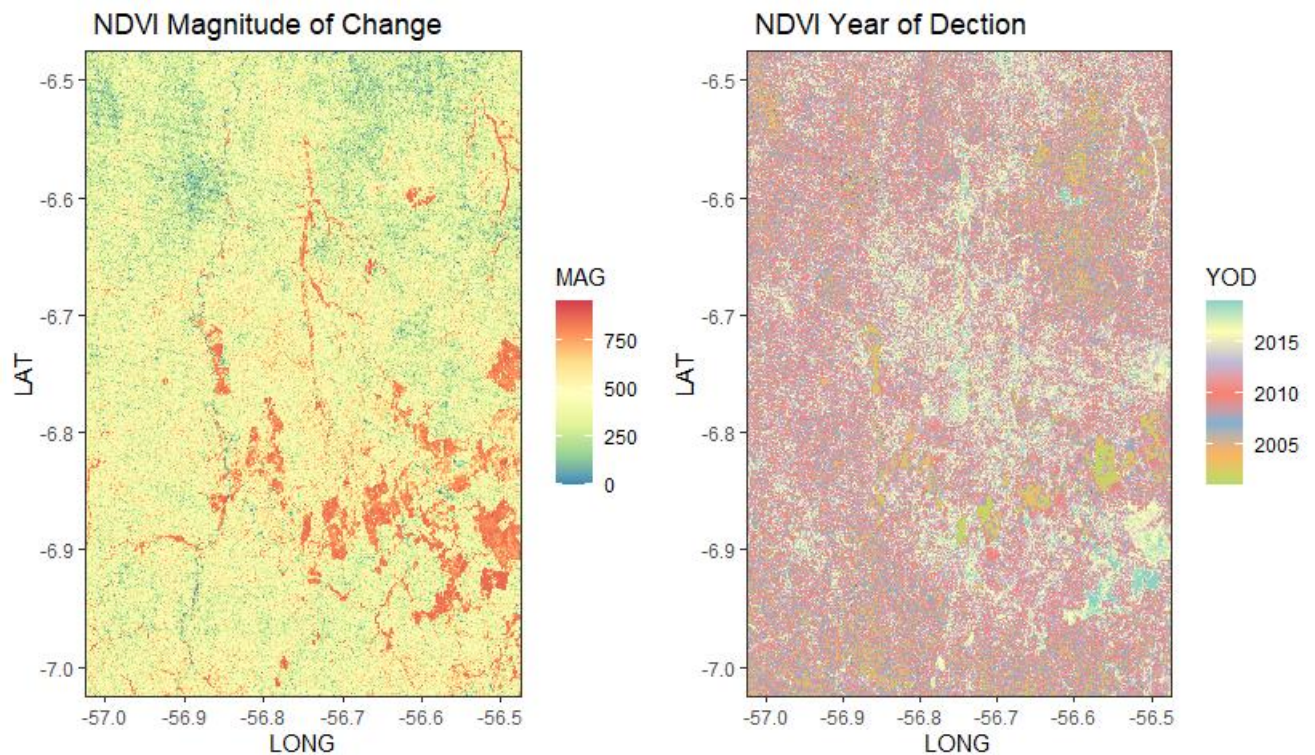


Figure 13. NDVI LandTrendr Output (MAG - YOD)

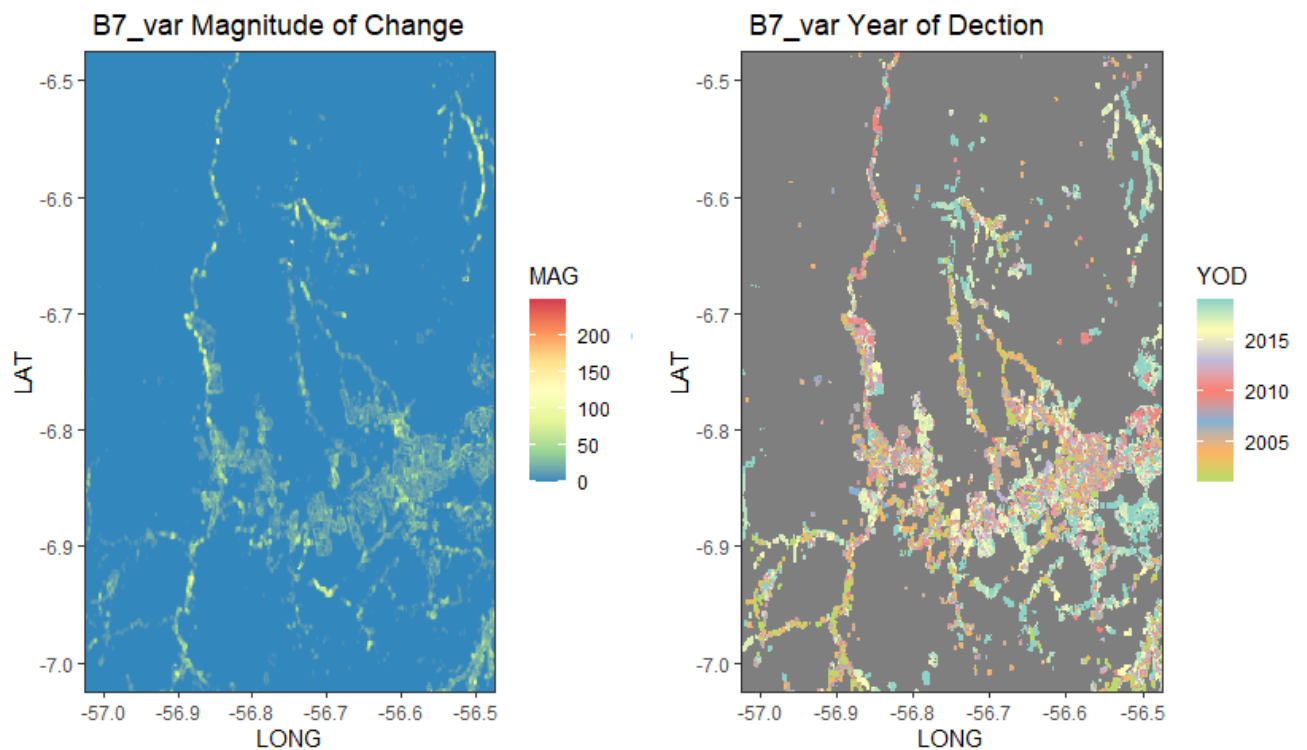


Figure 14. B7_Variance LandTrendr Output (MAG - YOD)

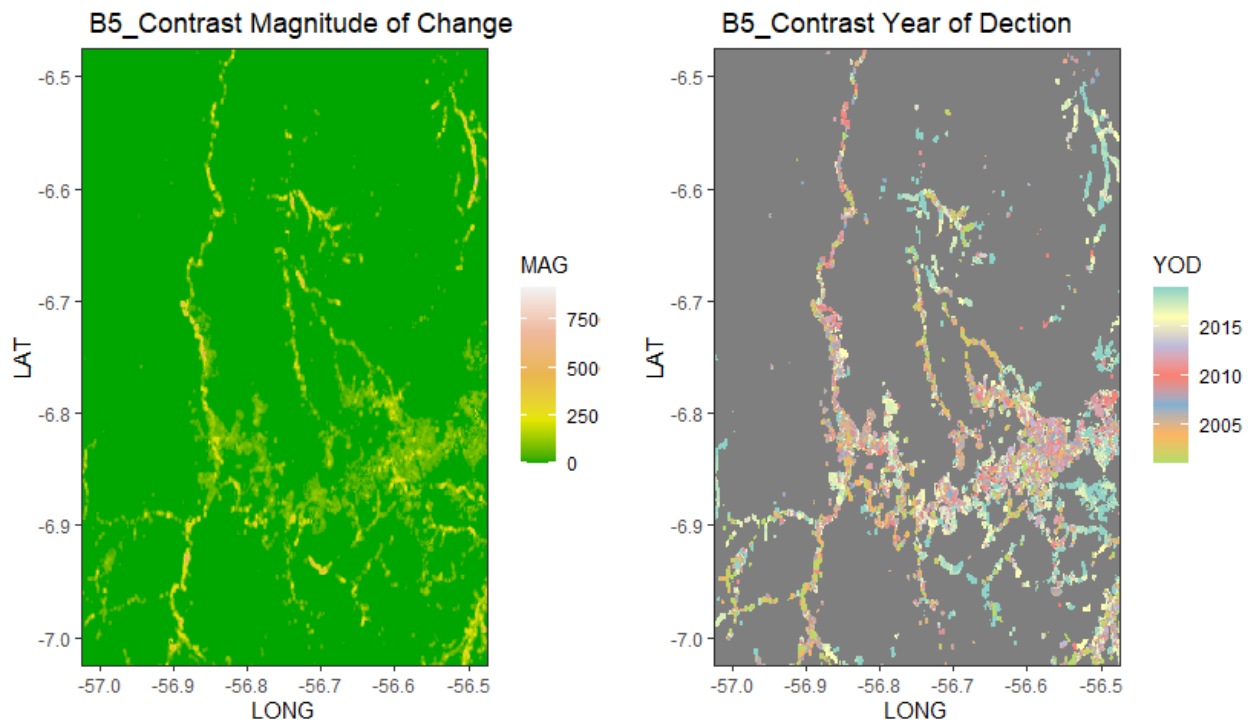


Figure 15. B5_Contrast LandTrendr Output (MAG - YOD)

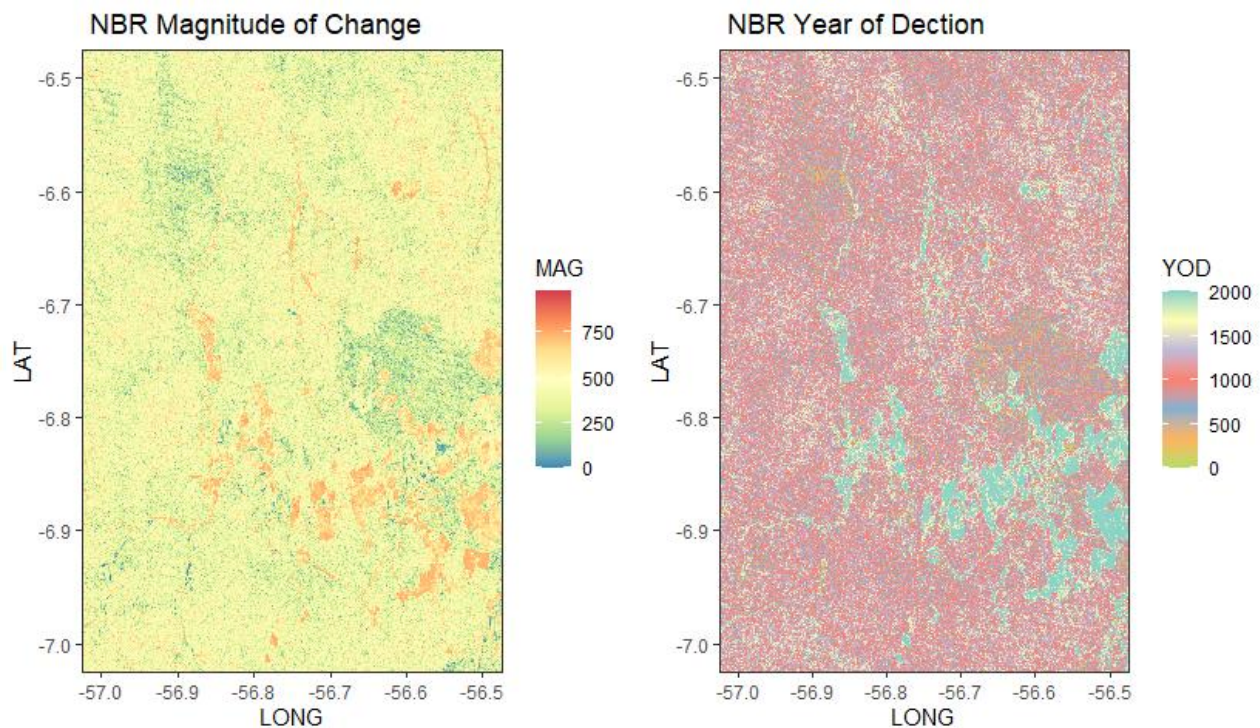


Figure 16. NBR LandTrendr Output (MAG - YOD)

3.2.3 Ancillary Data

Multisource image features are used in addition to multispectral image data to increase the thematic map's accuracy (Mcnaire & Protz, 1993). As an alternative to confirming the quality of the outcomes and the proper interpretation of the data, context analysis must be considered in a data-integration approach for LULC modeling (Lersch et al., 2007). The contextual inputs used in the current scope are: distance to rivers, distance to roads, Aspect, Elevation, Slope, and Topographic wetness index. These latest features were retrieved from a digital elevation model using an SRTM image collected by The Shuttle Radar Topography Mission (SRTM) (Farr et al., 2007). The SRTM image is a V3 product (SRTM Plus). It is provided by NASA JPL at a resolution of 1 arc-second (approximately 30m), downloaded, and wholly processed on the Google Earth Engine Platform.

The distance to roads data was calculated over the last image of the time series image collection (i.e., 2019). The water bodies and the roads dataset were downloaded from the Brazilian geo-web service at the Institute of geography and statistics to monitor the land use land cover of the Brazilian territory (e.g., IGBE, Monitoramento da Cobertura e Uso da Terra do Brasil). The distance is referred to as Euclidean distance, which measures the closest orthogonal distance from every ASGM to road or streams.

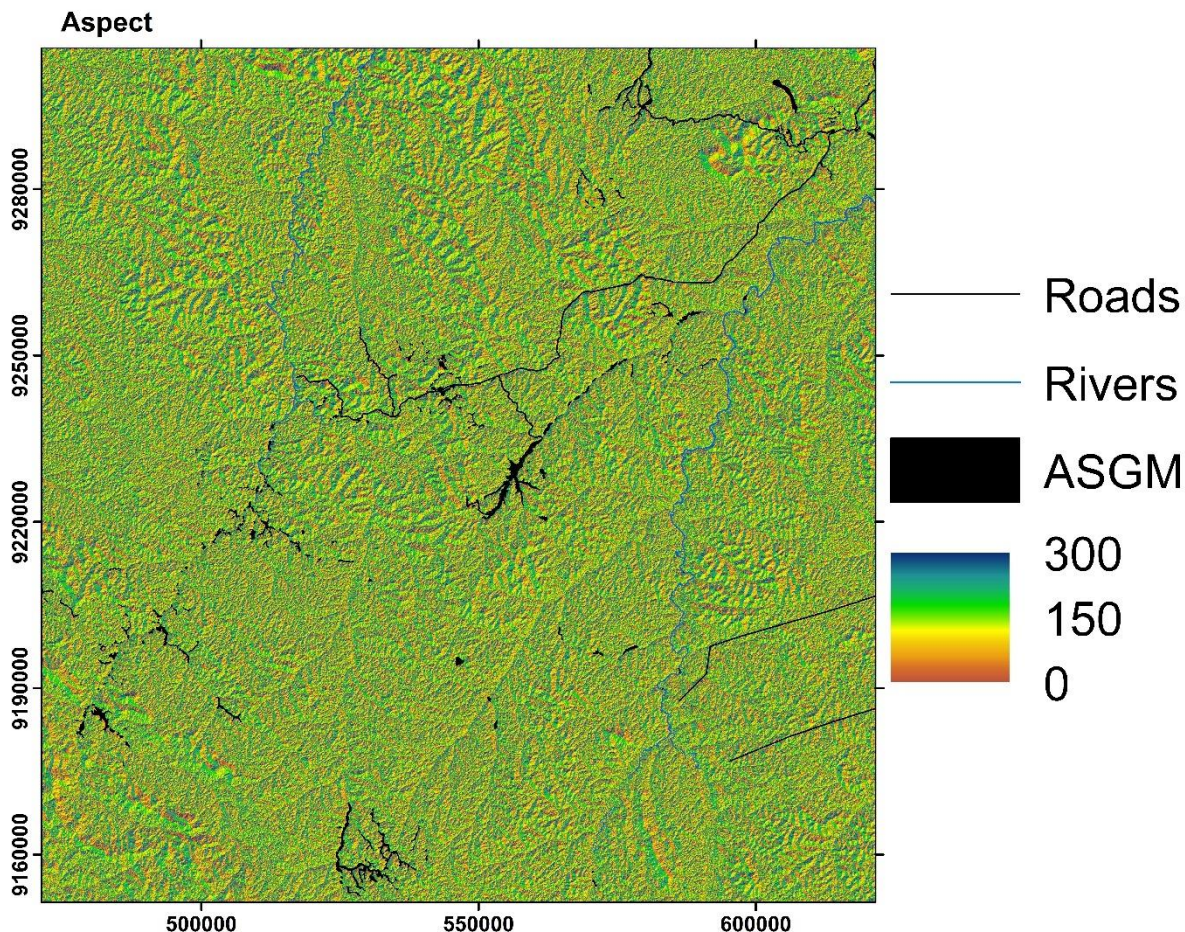


Figure 17. Ancillary Data: Aspect (AoI)

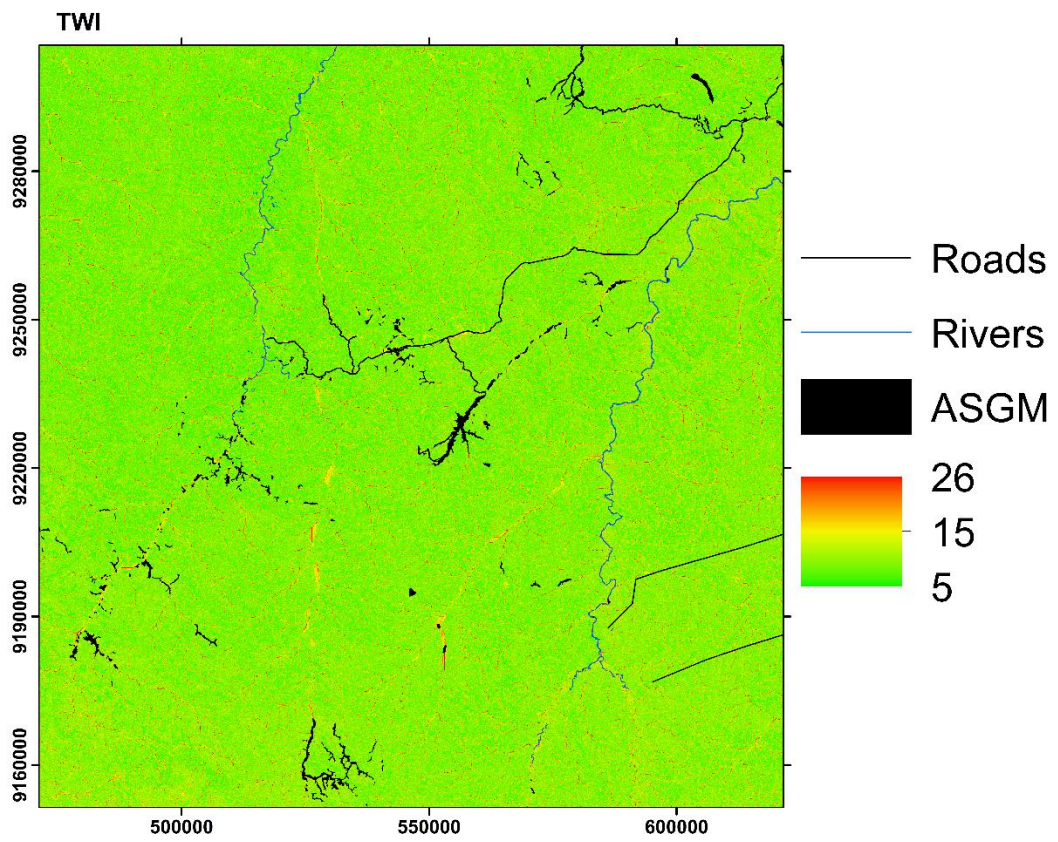


Figure 18. Ancillary Data: TWI (AoI)

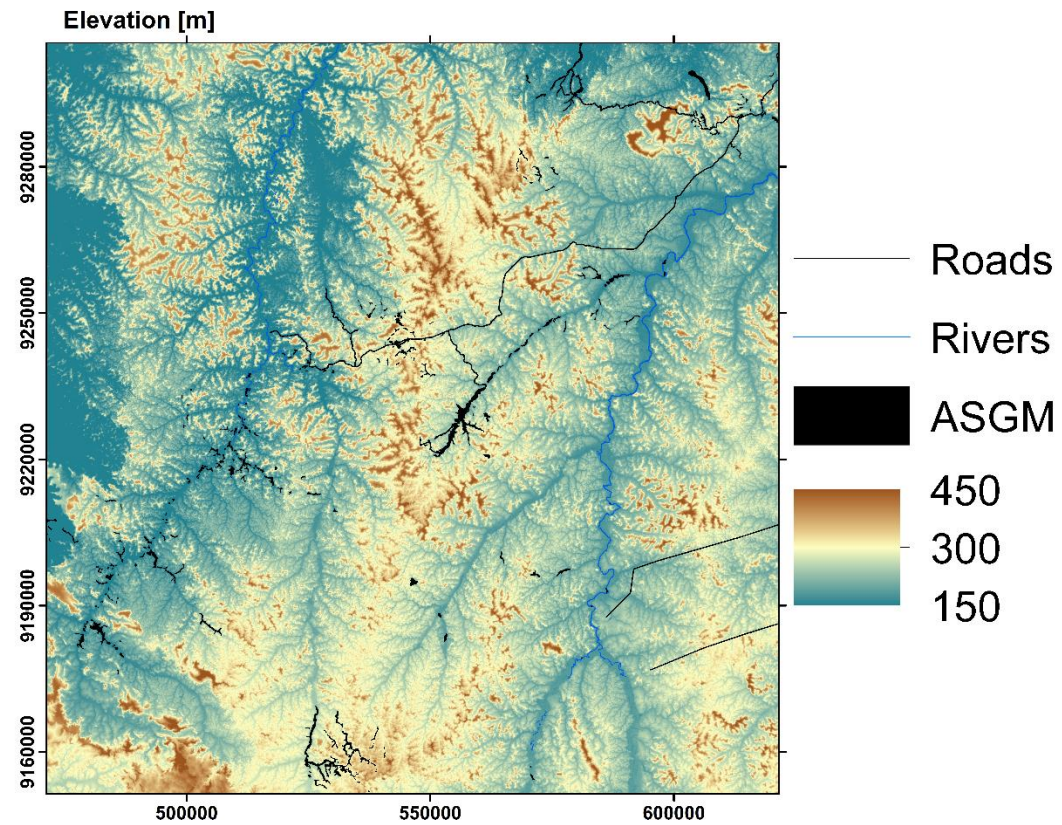


Figure 19. Ancillary Data: Elevation (AoI)

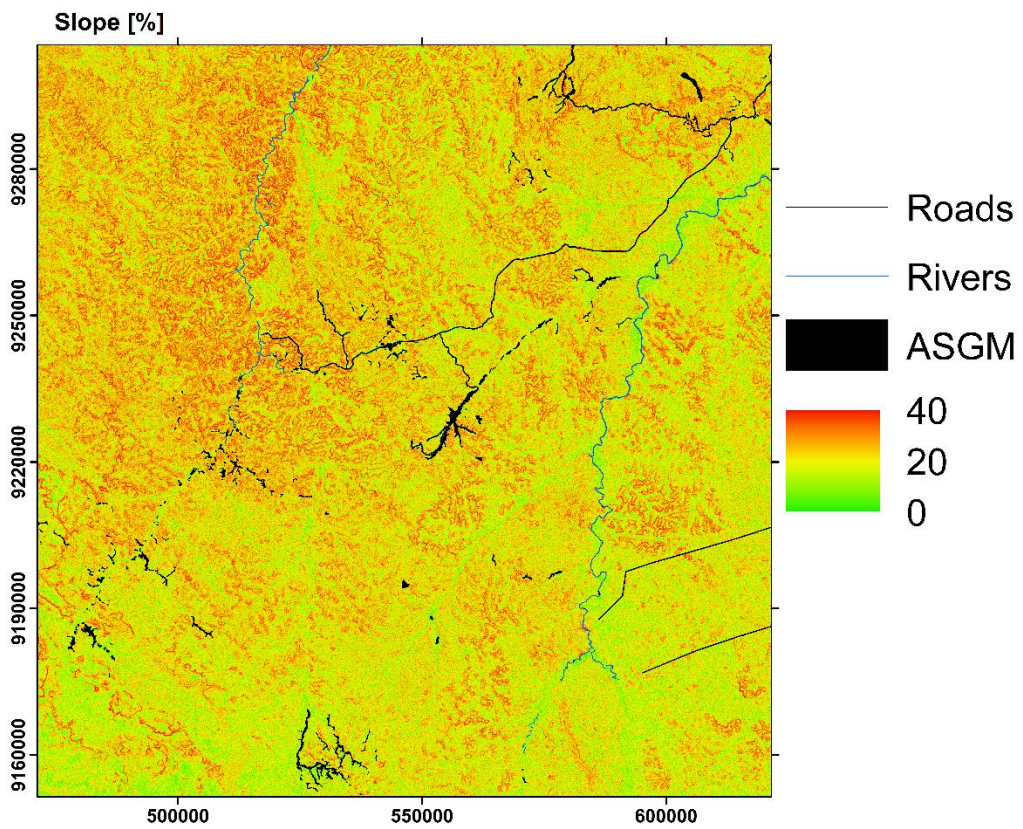


Figure 20. Ancillary Data: Slope (AoI)

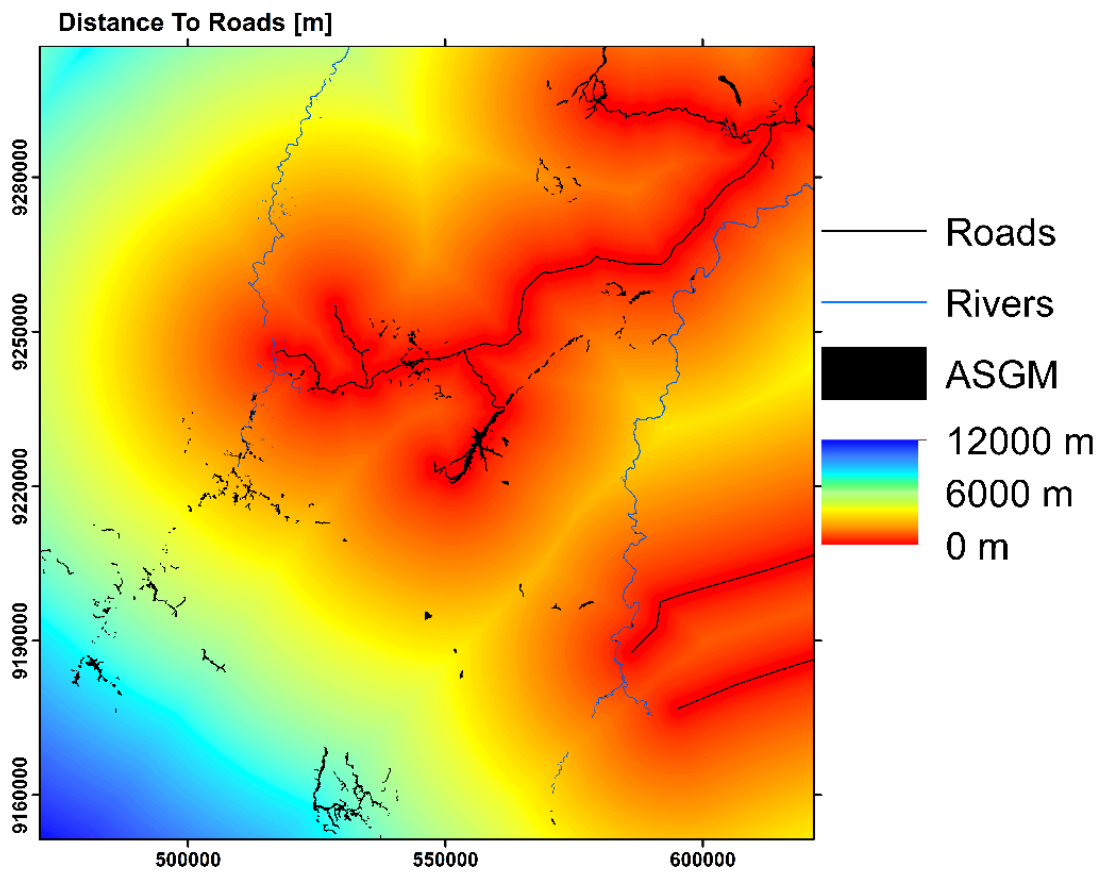


Figure 21. Ancillary Data: Euclidean Distance to Roads (AoI)

3.3 CLASSIFICATION

3.3.1 Random Forest

According to Belgiu & Drăgu. (2016), Random Forest (RF) is the most machine learning algorithm used in the remote sensing field given that it is a non-parametric model, relatively robust to outliers, and fast to train with few parameters. RF uses a bagging approach where a subset of the training samples randomly creates trees through replacement, indicating that some samples might be selected many times while others may not be selected (Breiman, 2001). The model splits the sample data set into training data (75%) and validation data (25%). The former is called in-bag-samples, and the latter out-of-bag (OOB), which is used for cross-validation through the classification process for the model's performance and error assessment. Moreover, the RF can handle extensive features datasets and noise (Breiman, 2001), being robust towards over-fitting compared to other machine learning algorithms because of the bootstrapping of weak learners and bagging characteristics (Breiman, 2001). Another reason for using the random forest in the current research is identifying important and relevant features in the high-dimensional dataset with efficient feature selection for subsequent feature reduction (Zhu & Woodcock, 2014). The feature selection is based on the model's performance during the learning process as an embedded feature selection method.

The most frequent variable importance measures in RF are the mean decrease which is based on prediction accuracy after permutation averaged over all trees in the forest, and the Gini impurity index that is calculated as the sum of the impurity decrease of every node that each variable was used for splitting in the forest (Touw et al., 2013).

The implementation of the Random Forest algorithm in this research has been adapted from Millard & Richardson. (2015) over an R programing language that provides complete support to perform various image classification processes. A set of 86 features were prone to feature important using mean decrease accuracy and mean decrease Gini metrics in the RF package (figure 22 and 23). Feature reduction using VSURF for model building with the best set of most important features, and subsequently classification using RF classifier for binary and probability of occurrence classification. The whole set of predictors is conformed by as shown in table 6. “*MAG TEXTURE FEATURES*” refers to the predictor calculated from raw spectral bands (image collection), which textures were calculated using the GLCM metrics and temporal segmented by the LandTrendr algorithm. Retrieving the Magnitude of Change for every textural feature used. Similarly, “*MAG SPECTRAL INDICES*” are the spectral indices calculated from the raw spectral bands in the image collection and temporal segmented, retrieving a singular raster of Magnitude of Change (MAG) per spectral index.

For mean decrease accuracy, the prediction accuracy is calculated on the OOB sample. The prediction is randomly selected in the OOB error, keeping the remaining variables constant, and the decrease prediction accuracy is calculated over the randomly selected data. Therefore, the metric indicates how much removing a variable the OOB decreases and how much including randomly a variable the OOB increases (Han, Guo, & Yu, 2016).

For mean decrease accuracy using the GINI index, the assessment is done on the variable at the tree splitting, which means that the calculations are performed during the training phase. Variables that result in nodes with higher purity have a higher decrease in the Gini index, and therefore the “pureness” is an indicator of feature relevance (Han et al., 2016).

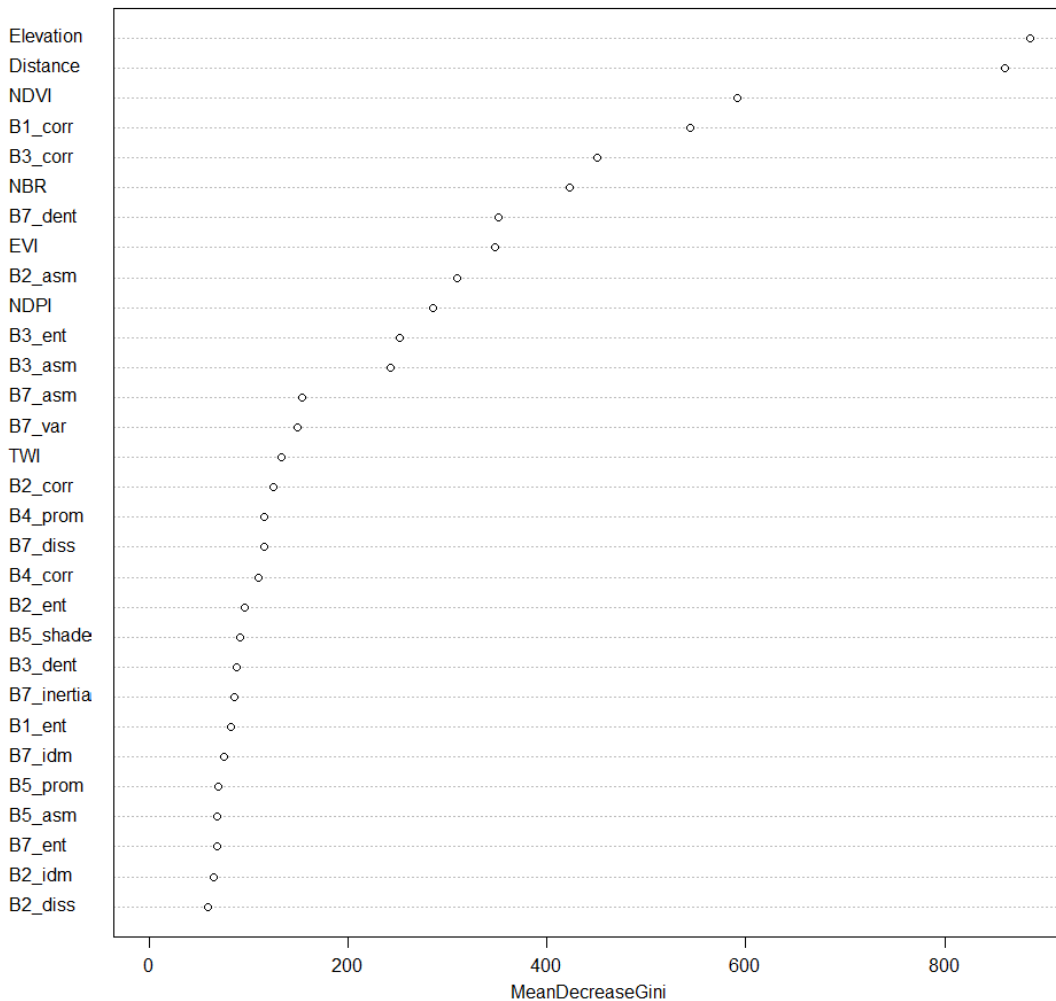


Figure 22. Variable Importance using Mean Decrease Gini

Figures 22 and 23 show the *variable importance* by both metrics. Nevertheless, both methods may overstate the importance of correlated predictors, the redundancy is not eliminated, and unreliable variables keep impairing the performance of the outcome. Additionally, the predictors and the relevant variables' selection are not established by a clear threshold. Therefore, for *variable selection*, *feature reduction*, and optimal outcome prediction, the package VSURF was employed using the function “Variable Importance” (hereafter VI).

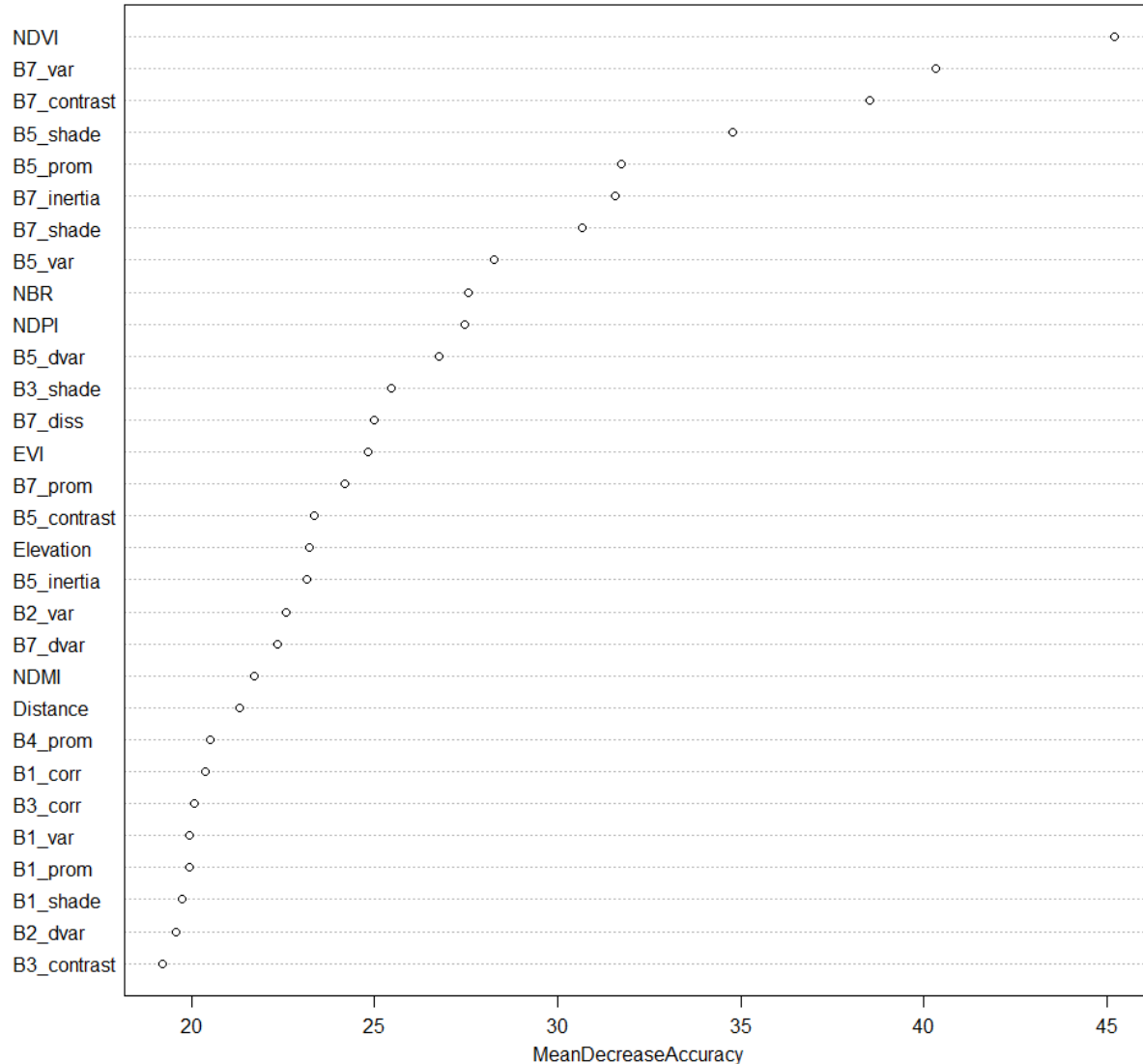


Figure 23 Variable Importance using Mean Decrease Accuracy

3.3.2 Variable Selection Using Random Forest (VSURF)

The efficacy of selection and feature reduction by different machine learning methods has been developed for classification and regression purposes. According to Sanchez-Pinto et al. (2018), tree-based methods such as VSURF perform the best feature selection and parsimony in larger and multicenter datasets instead of the classic-based stepwise selection based on the p-value. VSURF is an R language package that performs feature selection based on the Random Forest for regression and classification purposes (Genuer, Poggi, & Tuleau-Malot, 2015). It is implemented to reduce the outcome variability that RF as an ensemble technique might present and set a threshold for feature reduction based on VI measure standard deviation (a variable not included in the true underlying model has null importance).

VSURF is a wrapper-based algorithm that uses RF as the base classifier (Genuer et al., 2015) and works in three steps: Firstly, the whole set of features are ranked considering their mean

VI, and removing all the irrelevant features that have a low contribution to outcome in the classification. Secondly, the remaining set of features are tested in a descendent way of using nested RF models. The most accurate model is preserved, setting a cutoff based on the increase in model performance versus input by importance. Afterward, an ascending stepwise regression (model with n variables and the following one with $n+1$ variable consecutively) is executed for redundancy elimination of features. The variable is selected if the OOB error decreases more than the average variation resulting from the threshold set in the previous step (Genuer et al., 2015). In other words, a feature is rejected just if the OOB error does not decrease or decrease slightly based on the threshold calculated for minimizing the OOB error (Genuer et al., 2015). As a result, two models are resultant at the final step of the procedure: An *interpretation* model, formed in the second step based on the cutoff of the variable importance. Furthermore, a prediction model was obtained in the third step with the essential features. Features selected during the prediction steps are considered for further analysis.

Figures from 24 to 27 show the feature reduction process performed with VSURF. Figure 24 shows all variables sorted in declined order considering their mean VI. Figure 24 shows the nested RF models performed using the remaining features to estimate the lower OOB error and the threshold (red line) established by using a CART (Classification And Regression Tree) model based on the standard deviation of the variable importance (Genuer et al., 2015). Features with a mean and standard deviation of the VI greater than the threshold are selected. Figure 25 shows the added step-by-step fashion features that decrease error by a small margin larger than a threshold (Virdi et al., 2019). Besides, figure 26 renders the prediction model with the best set of features and the OOB error. Finally, figure 27 shows the final output with the prediction model.

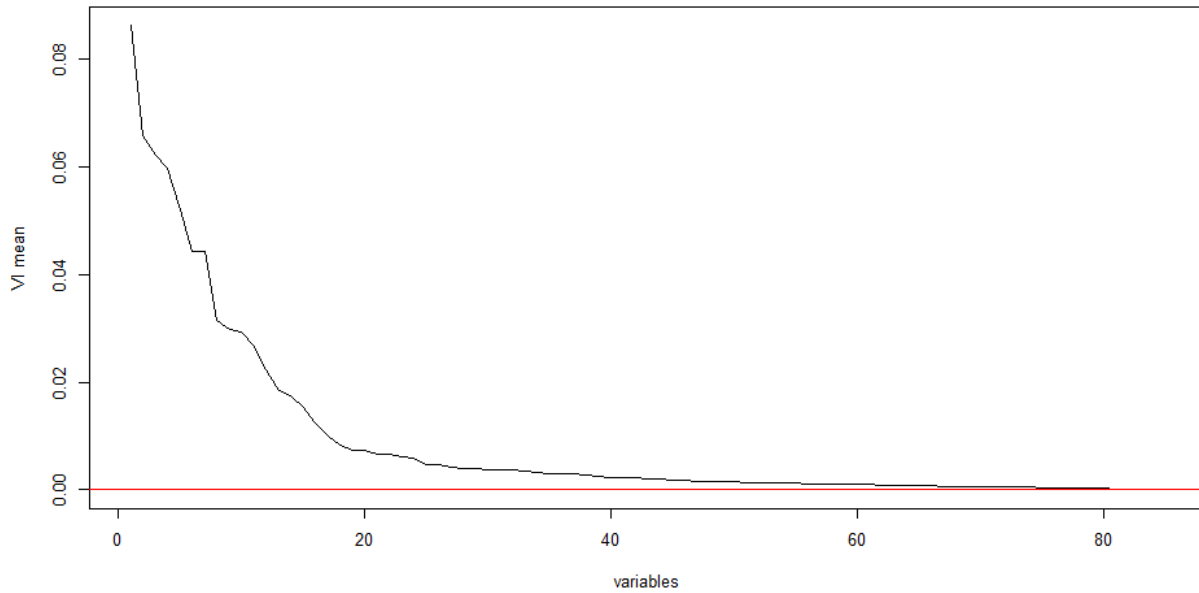


Figure 24. Features sorted by decreasing mean Variable Importance

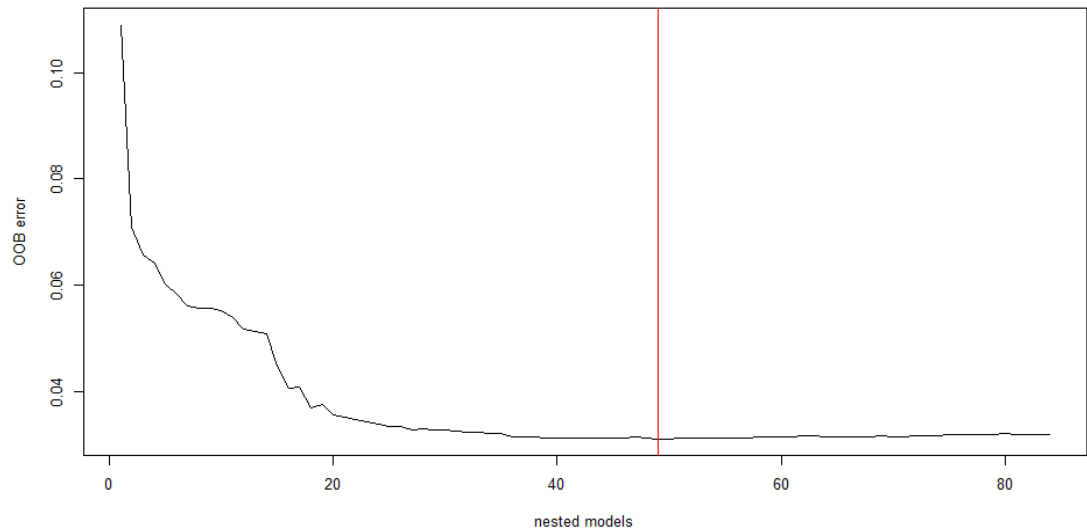


Figure 25 Nested RF model for model's definition with the lower OOB

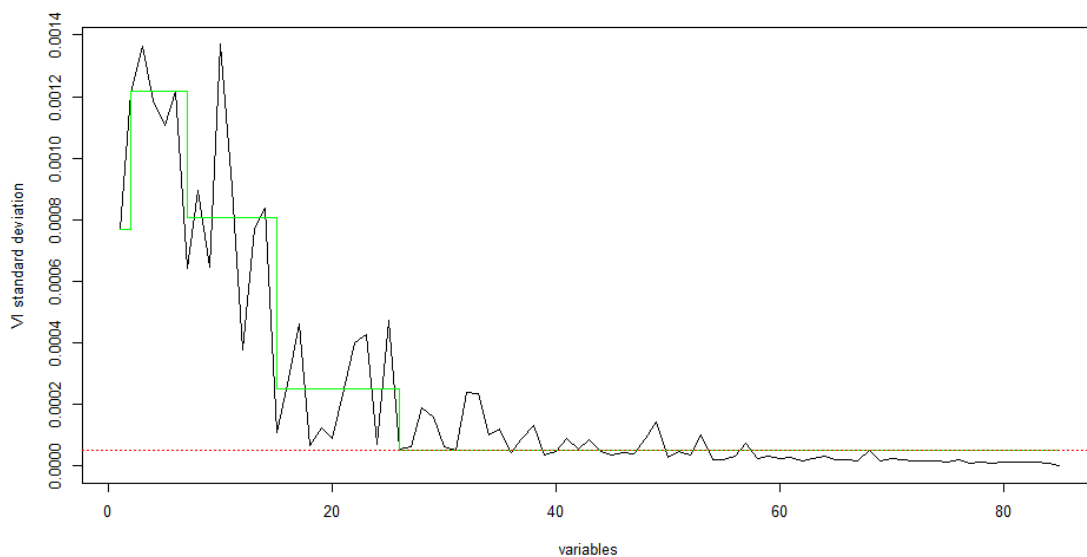


Figure 26. Step-by-step added in regression for feature reduction

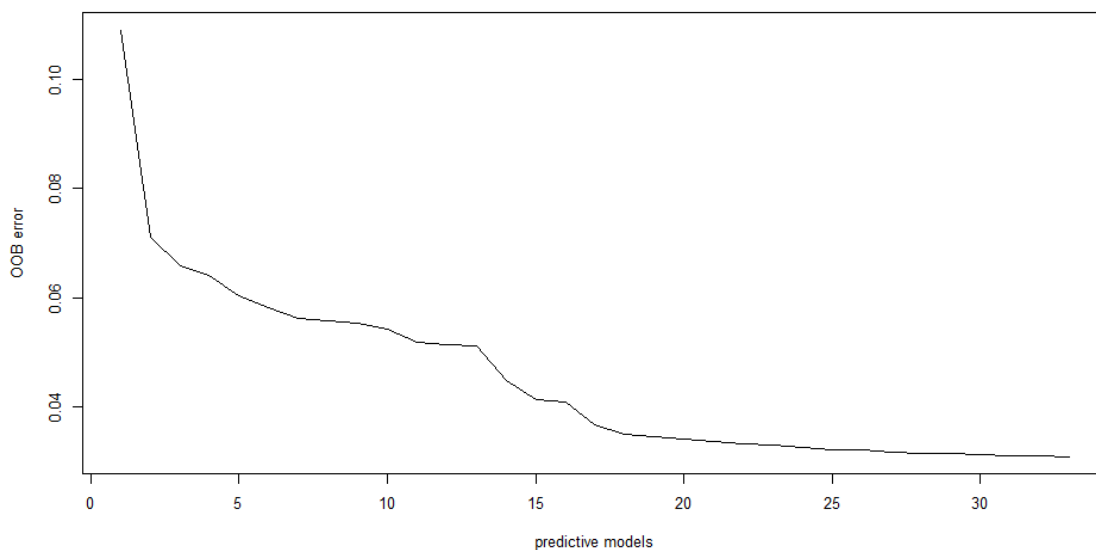


Figure 27. Prediction Model based on OOB Error

3.3.3 Partial Dependence Plots (PDP)

Finding the most relevant variables is essential for feature reduction, reduce data processing and improve computer time processing. Nevertheless, the most significant variables do not provide complete information about the relationship between the input and the predicted outcome, neither how changes influence the predictions in the input variables. An alternative to analyze the feature's incidence over the outcome and how variations influence the result and performance is using a Partial Dependence Plot (PDP).

According to Friedman, (2001), a partial dependence plot explains the marginal effect that one or two features have on the predicted outcome of a machine learning model. The PDP shows the relationship between the target response and a set of input features of interest, marginalizing over the whole set of predictors' values. The plots mainly explain the relationship between the response and a specific input variable by a function that renders the expected target response while accounting for the other predictors' average effect in the model.

The partial dependence plot is particularly convenient to understand the assumptions and hidden relations present in the prediction outcome and model performance. Figure 32 and 33 shows the PDP for the most important features of the prediction model.

3.3.4 RF Model Building

The prediction model was used for RF model Building considering the variable selection and feature reduction results. The main input parameters of the Random Forest classifier are the number of trees and the number of variables at a split. Table 7 shows the input parameters, and figure 29 displays the OOB error vs. the number of variables at the split. Figure 30 the OOB error vs. the number of trees, generated for the Random Forest model calibration. The values coincides with Belgiu & Drăgu. (2016), where the optimal number of trees is around 500, and the number of a variable at the split is estimated based on the square root of the number of predictors.

Table 10. The Random Forest Input Parameters.

PARAMETER	VALUE
NUMBER OF TREES (ntrees)	500
NUMBER OF VARIABLES AT THE NODE-SPLIT(mntry)	6
ITERATIONS	50

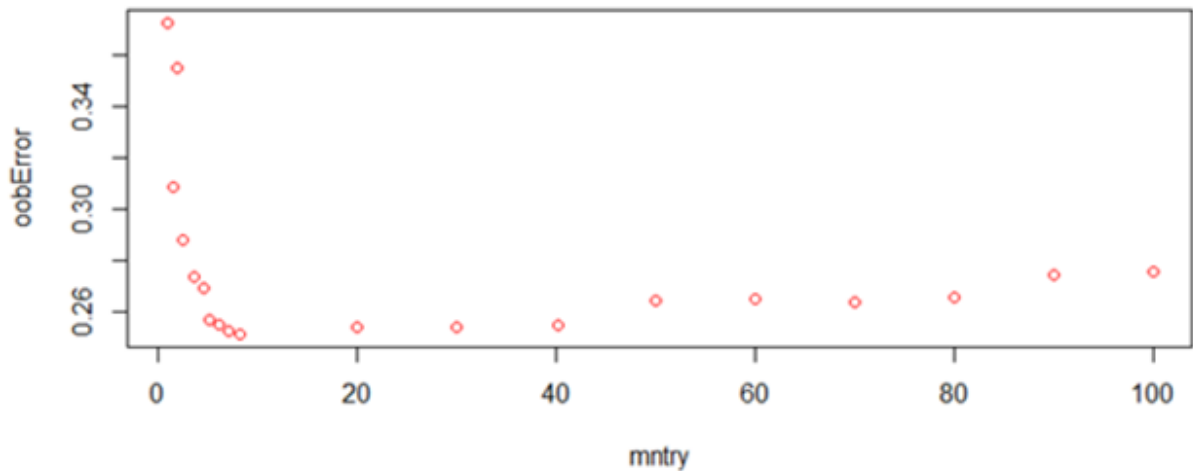


Figure 28. RF mntry tuning Parameter

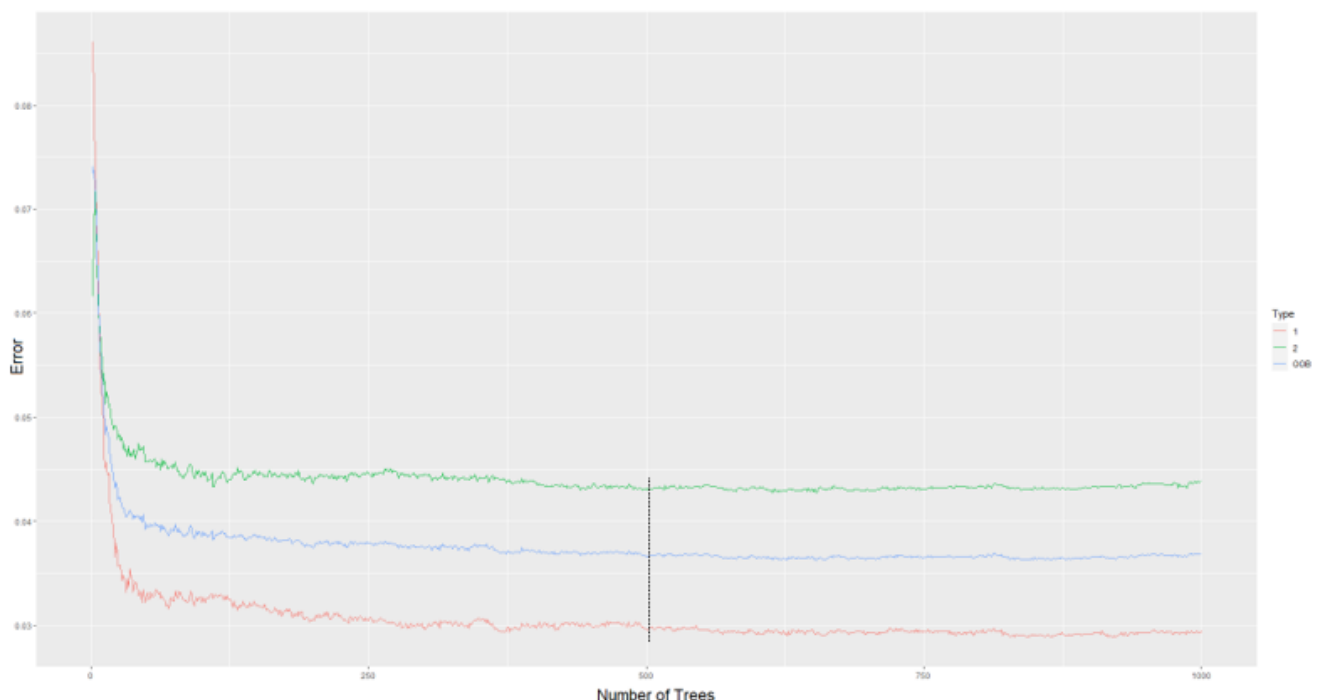


Figure 29. RF ntree Tuning Parameter

4. RESULTS

This chapter is divided into four main parts. The feature selection and reduction resulting after using the VSURF package, showing the established thresholds for feature reduction and model performance. The second, is a quantitative accuracy comparison of three sets of features to assess the relationship between model accuracy and the number of features. Afterward, PDPs were extracted for the most important variables for extending comprehension of each feature over the ASGM detection. Finally, a binary classification (Mine / No Mine) and probabilistic classification (probability of mine occurrence) were performed. A total of 500 ntree and seven mntry using 50 iterations were used for model parameters and model error estimation, respectively. The average OOB error was 0.0382, and the average mean independent error was 3.79, with an average accuracy of 89.27%.

4.1 Variable Selection and Feature Reduction Results

A total of 49 features had been selected for the interpretation model. For model prediction, the final selection has been reduced to 33 features. Figure 30 shows the thresholds of the two models considering the mean square error, and table (11) details the set of 33 variables. From the prediction model, a total of 26 predictors corresponds to texture features, five spectral indices, and two ancillary data. The most important texture predictors are retrieved from the harmonized bands 5 and 7 (SWIR-1 and SWIR-2, respectively), where healthy vegetation shows the lowest reflectance values in the spectral signature. Figure 31 renders the final predictor variables vs. the OOB error. NDVI has been found the most important variable, followed by the B7 variance texture, B5 prom, B5 shade, and B7 shade as the top five features.

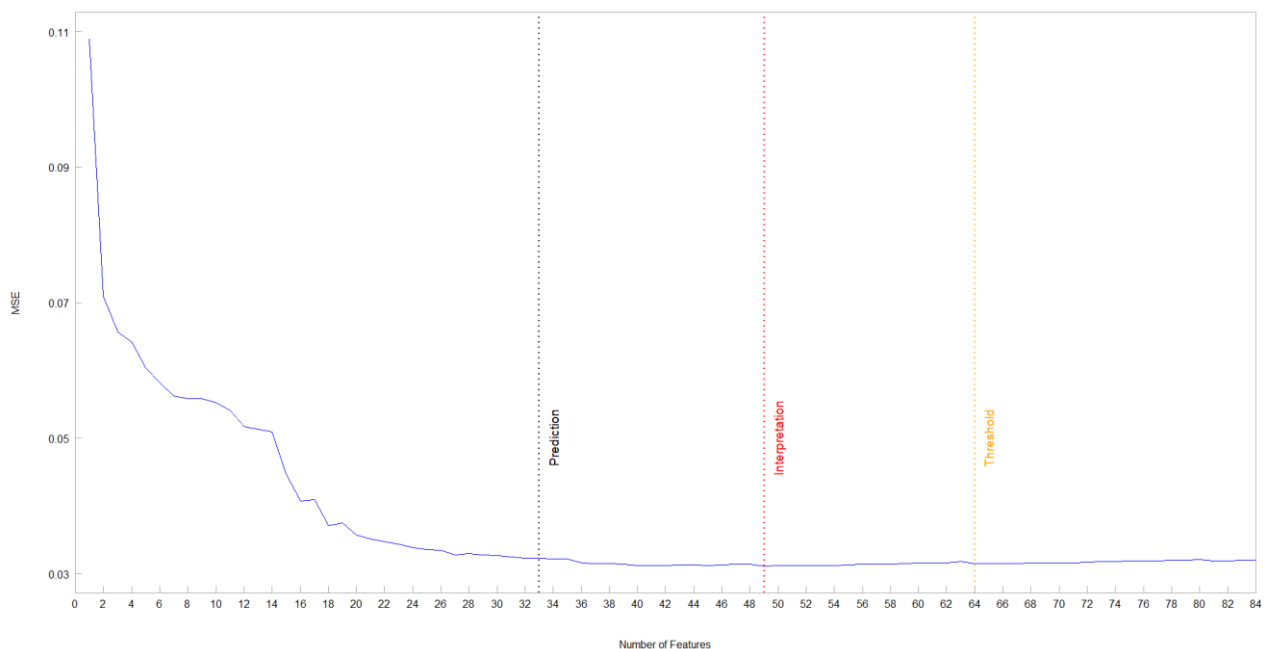


Figure 30. The threshold for Prediction Model and Interpretation model based on MSE

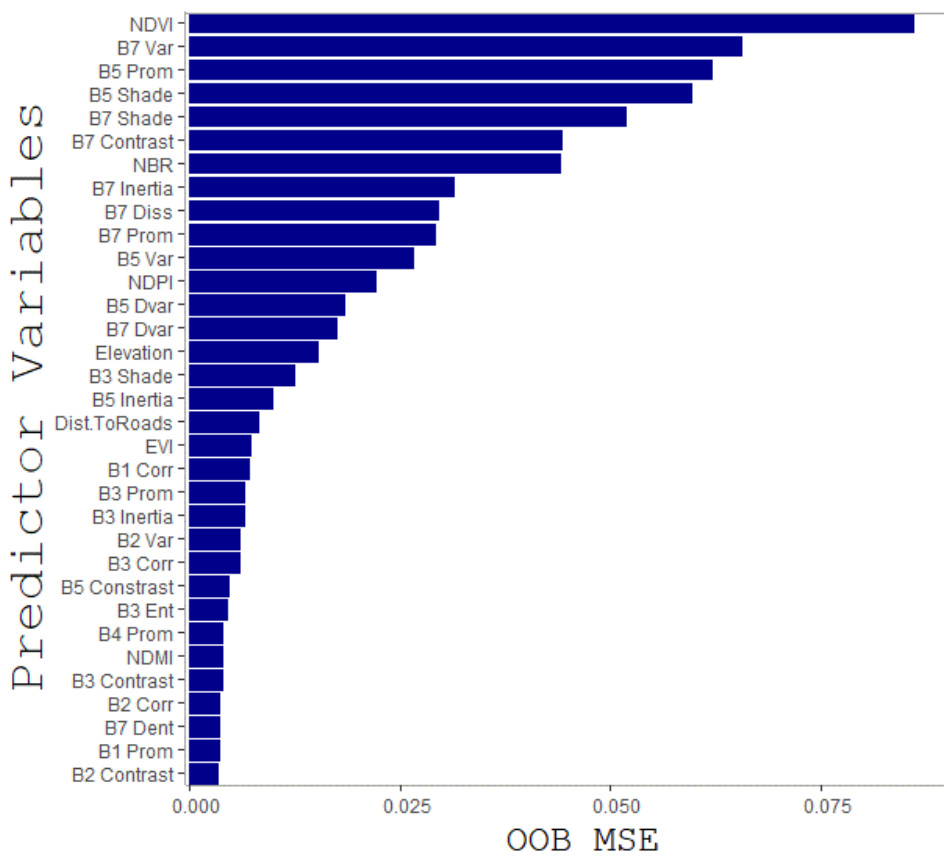


Figure 31. OOB Error delta mean square error per predictor variable

Table 11. Ranking most important variables for Prediction Model

No.	FEATURE	No.	FEATURE	No.	FEATURE
1	NDVI	12	NDPI	23	B2_var
2	B7_var	13	B5_dvar	24	B3_corr
3	B5_prom	14	B7_dvar	25	B5_contrast
4	B5_shade	15	Elevation	26	B3_ent
5	B7_shade	16	B3_shade	27	B4_prom
6	B7_contrast	17	B5_inertia	28	NDMI
7	NBR	18	Distance	29	B3_contrast
8	B7_inertia	19	EVI	30	B2_corr
9	B7_diss	20	B1_corr	31	B7_dent
10	B7_prom	21	B3_prom	32	B1_prom
11	B5_var	22	B3_inertia	33	B2_contrast

Table 12. Prediction model by type of features

FEATURE	TYPE	NUMBER OF FEATURES
Texture	Prom, Contrast, Var, Shade, Inertia, Corr, Dvar, Diss, Ent, Dent	26
Vegetation	NDVI, NBR, NDPI, EVI, NDMI	5
Ancillary Data	Elevation, Distance	2

Table 13. Ranking Variable Importance with Mean Decrease Accuracy and VI standard deviation

No	FEATURES	VI	VI	No.	FEATURES	VI	VI
		Sta.Dev	MeanDecrease			Sta.Dev	MeanDecrease
1	NDVI	0.000768011	0.086136214	26	B3_ent	5.69E-05	0.004601793
2	B7_var	0.001214494	0.065801011	27	B4_prom	6.43E-05	0.004125678
3	B5_prom	0.001363601	0.062143871	28	NDMI	0.000189417	0.00399991
4	B5_shade	0.001187905	0.059787028	29	B3_contrast	0.000160357	0.003955951
5	B7_shade	0.001104322	0.052050002	30	B2_corr	6.45E-05	0.00368263
6	B7_contrast	0.001218029	0.044299986	31	B7_dent	5.20E-05	0.003644859
7	NBR	0.000641549	0.044133753	32	B1_prom	0.000239543	0.003637752
8	B7_inertia	0.000895801	0.031510645	33	B2_contrast	0.00023743	0.00353344
9	B7_diss	0.000644374	0.029756789	34	B1_dvar	0.00010211	0.003239557
10	B7_prom	0.001369874	0.029286184	35	B3_dvar	0.000120067	0.003056289
11	B5_var	0.000901177	0.026644781	36	B3_asm	4.57E-05	0.002960275
12	NDPI	0.000376579	0.022220074	37	B2_inertia	8.86E-05	0.002883857
13	B5_dvar	0.00077405	0.01843628	38	B2_dvar	0.00013064	0.002853011
14	B7_dvar	0.000839501	0.017564857	39	B4_corr	3.62E-05	0.002410043
15	Elevation	0.000108594	0.015360494	40	B2_asm	4.83E-05	0.002363509
16	B3_shade	0.000268223	0.01249159	41	B1_inertia	8.84E-05	0.002273973
17	B5_inertia	0.000460993	0.010048809	42	B7_asm	5.38E-05	0.00218526
18	Distance	6.68E-05	0.008326515	43	B1_dvar	8.44E-05	0.002081691
19	EVI	0.000125837	0.007364225	44	B4_var	4.59E-05	0.001929984
20	B1_corr	8.84E-05	0.007225522	45	NDWI	3.70E-05	0.001767823
21	B3_prom	0.000251745	0.006644481	46	B2_ent	4.32E-05	0.001716429
22	B3_inertia	0.000401314	0.006593314	47	B2_idm	4.13E-05	0.001665071
23	B2_var	0.000429015	0.006112326	48	B3_diss	8.89E-05	0.001587885
24	B3_corr	6.89E-05	0.005998248	49	B1_shade	0.000144978	0.001483771
25	B5_contrast	0.000472913	0.004796879				

4.2 Partial Dependence Plots Prediction Model

Understanding the relationship of the input features for estimating ASGM probabilities (presence) can be described briefly using the PDPs, as shown in figure 31. The chart depicts the six most important variables of the prediction model (see appendix 2 for complete PDPs for prediction model). The units in the Y-label correspond to probability [0,1], where 1 is the presence of ASGM, X-label renders the magnitude of change of each feature multiplied by one thousand in the temporal segmentation.

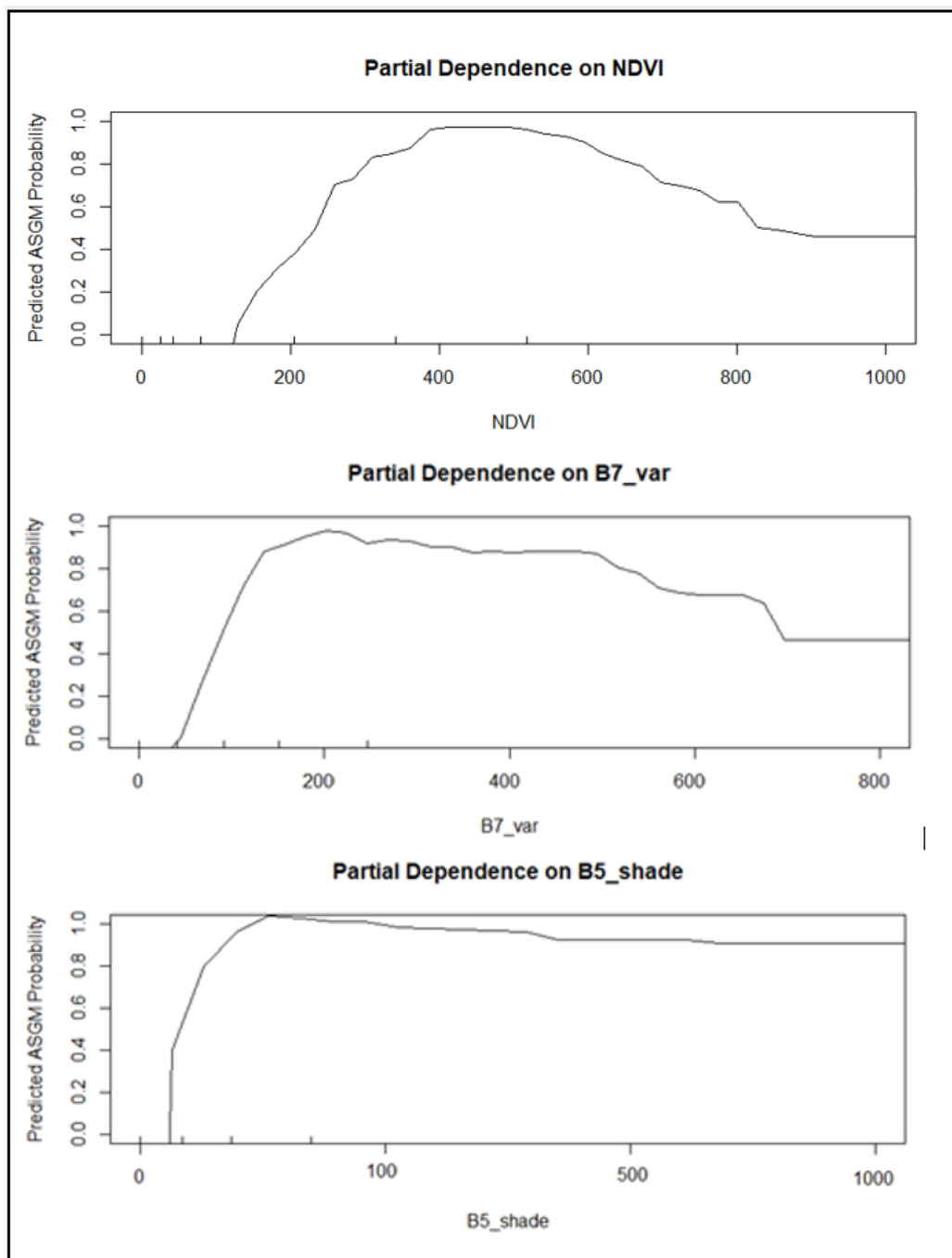


Figure 32. Partial Dependence Plot per Feature. Top: NDVI. Medium: B7_Var. Bottom: B5_Shade

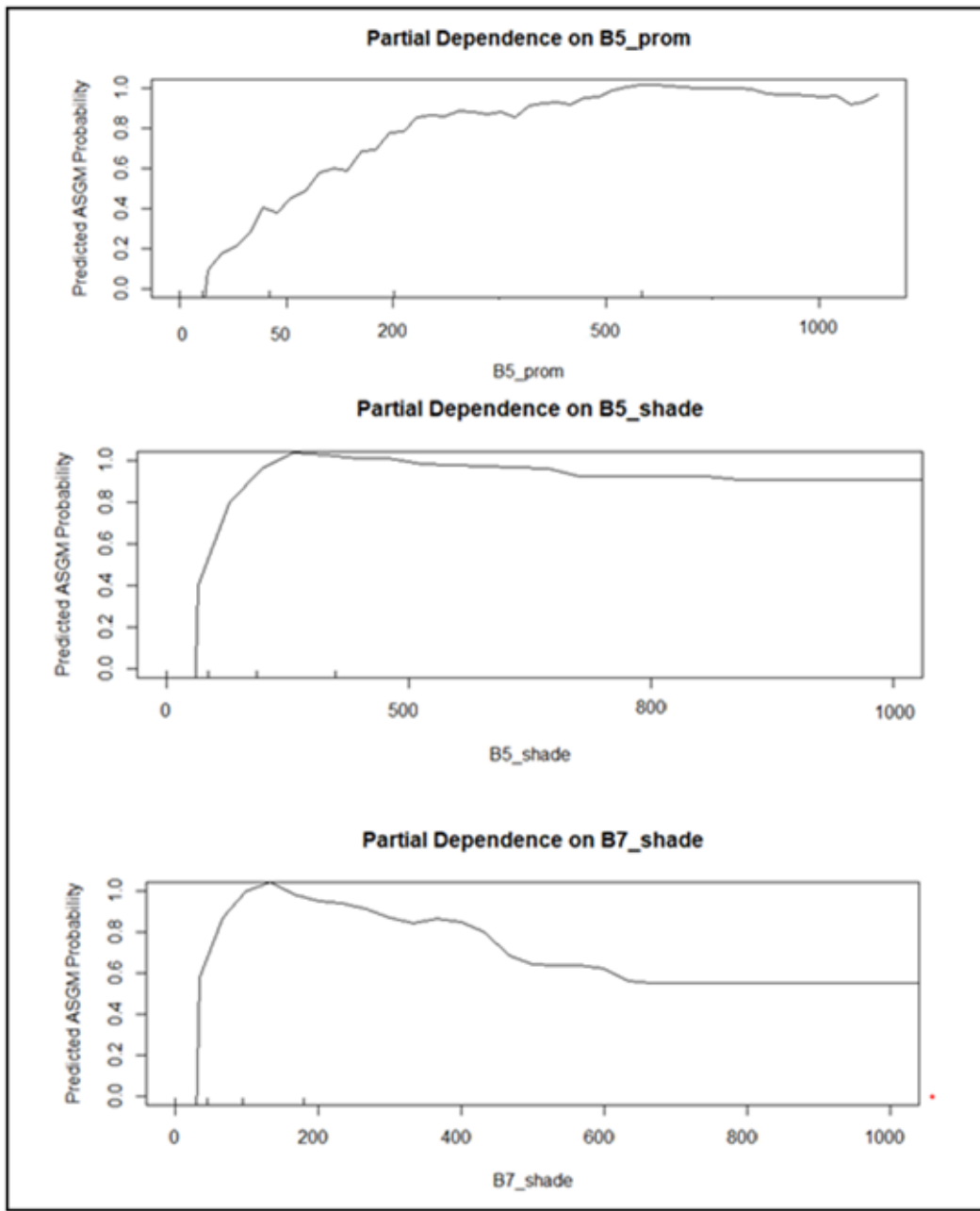


Figure 33. Partial Dependence Plot per Feature. Top: B5_Prom. Medium: B5_Shade. Bottom: B7_Shade

The plots explain the relationship of changes in probabilities of ASGM presence with the change in classification by features in the prediction model. From the chart, it can be inferred that low values in B7_shade and B5_shade have the highest ASGM's presence probabilities among all sets of texture features. This can be partly explained since Cluster Shade is a skewness indicator; lower values are more related to high asymmetry in the pixel; in contrast, higher values result from an image with high uniformity. In comparison, when Cluster Prominence (B5_prom) value is high indicates a peak in the mean values at the GCLM matrix showing a high variation in the grayscale levels. Therefore, the combination of both types of textures complements the spatial relations information, hence the probabilities of ASGM prediction.

The ASGMs are forest disturbances that change the homogenous symmetry of the tropical forest by small clusters or patches where the settlements take place, particularly close to the water bodies. Those alterations in the landscape break the uniformity of the forest independently of the land cover modified. This can also be seen from the vegetation indices, particularly NDVI and NBR, where the dense forest land cover is replaced; values around 400 (interval: [-1,1] * 1000) have more probabilities in ASGM prediction. High NDVI and NBR values generally indicate healthy vegetation, while low values represent the bare ground, deforested patches, or recently burned areas.

It is important to note that the partial dependence plot represents the effect of the predictor after accounting the average effect of the other predictors, which analogically can be seen as a singular linear regression, where the “y” coefficient on each “x” separate feature, measure the effect obtained dismissing the other predictors' effect. The previous charts show that values around 200 for variance (texture) have a higher marginal effect on the detection of the ASGM, depicting.

4.3 Prediction Model Error Assessment

The prediction models were subjected to comparison and assessment on the average OOB error, the average independent error, and the average mean overall accuracy with the prediction model and the whole set the features. In order to assess the feature reduction and its influence on the accuracy of the final classification, some calculations were performed running 50 iterations, and the average for all iterations was considered a model performance indicator (Table 13). The number of trees for every model and iteration remains constant, according to chart 29. The number of variables for splitting was set considering the root square of the number of. The results can be found in table 13, and the values reached per iteration in figure 31.

Table 14. Model Comparison Assessment

	WHOLE SET OF FEATURES	INTERPRETATION MODEL	PREDICTION MODEL
Average Mean OOB Error	3.82%	3.76%	3.79%
Average Mean Independent. Error	3.79%	3.71%	3.82%
Average Mean Overall Accuracy	89.27%	92.6%	90.8%
Number of Variables	86	49	33
Ntree	500	500	500
Mtry	10	7	6

The OOB error is computed as the number of correctly predicted values from the out-of-the-bag sample, being an indicator of RF model validation and prediction error assessment while being trained. The independent error is used to assess the stability of predicted classes and thus evaluate the classification quality. The comparison assessment table shows no spatial autocorrelation among the predictors on the three models; according to Millard & Richardson, (2015), when the spatial autocorrelation between the training samples is low, the OOB error tends to be similar to the independent error. On the other hand, the OOB error curves and the

independent error do not show any trend along with the number of iterations; the values fluctuate between 3.7% and 3.9%, showing consistency in the classification in the prediction. Despite the difference in the number of features of the three models, the overall accuracy reached, particularly, the prediction is a bit more than 90%, which is very acceptable for model performance.

Moreover, in terms of accuracy and error difference between the prediction and interpretation model is slightly modest despite the difference in features. Sixteen additional variables increase the accuracy by 1.8%.

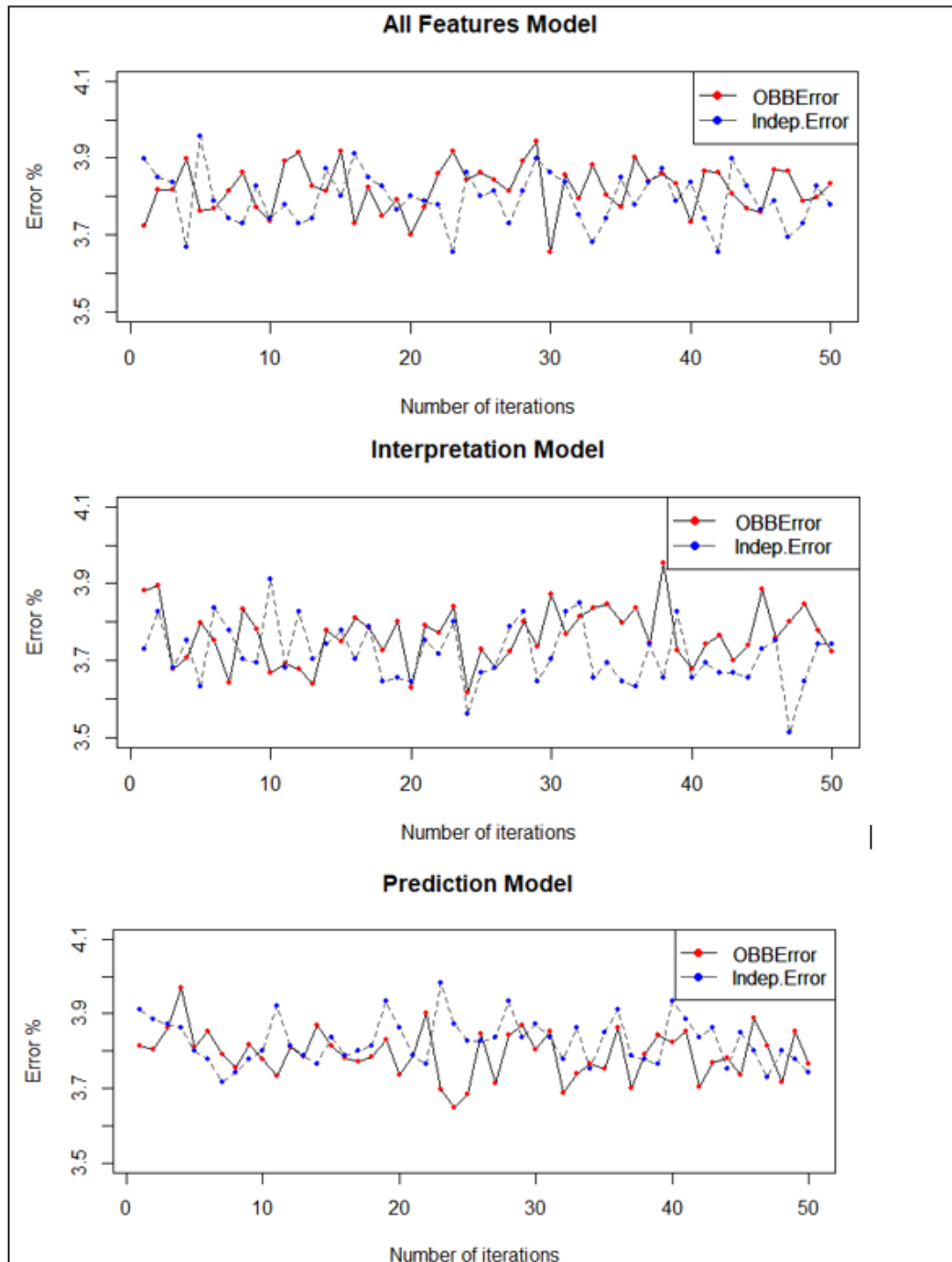


Figure 34. OOB error and independent error for Top: the whole set of features. Medium: Interpretation Model
Bottom: Prediction model

4.4 Binary Classification

Although ASGM is not considered a land cover in the scope of this research (assumption), the binary classification was used for preliminary and qualitative assessment of the feature's performance. Additionally, considering the assessment of the model and the mean overall accuracy, a binary classification with (Mine/ No Mine) was performed (figure 35).

Some remarkable findings from the binary classification and the predictors' performance were found in the thematic map. For instance, the model could discriminate water bodies and roads where the ASGM activities are absent despite the similar spectral reflectance; in turn, sandbanks and sediments lengthwise the rivers were also labeled as not mines. Since predictors mainly represent the magnitude of change, fundamentally for significant changes in the time series and not only for the spectral reflectance of the land cover. Moreover, there is an evident clustering occurrence in the mine class distribution close to the roads and rivers whereby the mining ponds are located for mineral extraction, and some informal settlements are incorporated for later transportation. Water is an indispensable resource for mining needed for the extraction of minerals that may be in the form of solids such as sand or gravel, and therefore the presence of the mines is outstandingly close for water bodies, as shown in figure 35.

Nevertheless, the classification was not able to distinguish deforested areas from ASGM completely. Despite that, logging activities are highly correlated with the ASGM settling. Deforested patches are not necessarily ASGM. However, in the ASGM settling, a deforestation process is nurtured for mineral extraction into the mining ponds along the shoreline and the incorporation of machinery inland. Therefore, the relationship between deforestation and ASGM settlements is unidirectional, where the ladder implies mostly the former but not necessarily deforested patches means ASGM activities.

Table 14 depicts the confusion matrix for the binary classification. Class 1 represents the areas classified as Mine.

Table 15. Confusion Matrix for Binary Classification

CLASS	1	2	Class. Error
1	7329	195	0.02591
2	490	9861	0.04733

Overall accuracy: 0.9082742

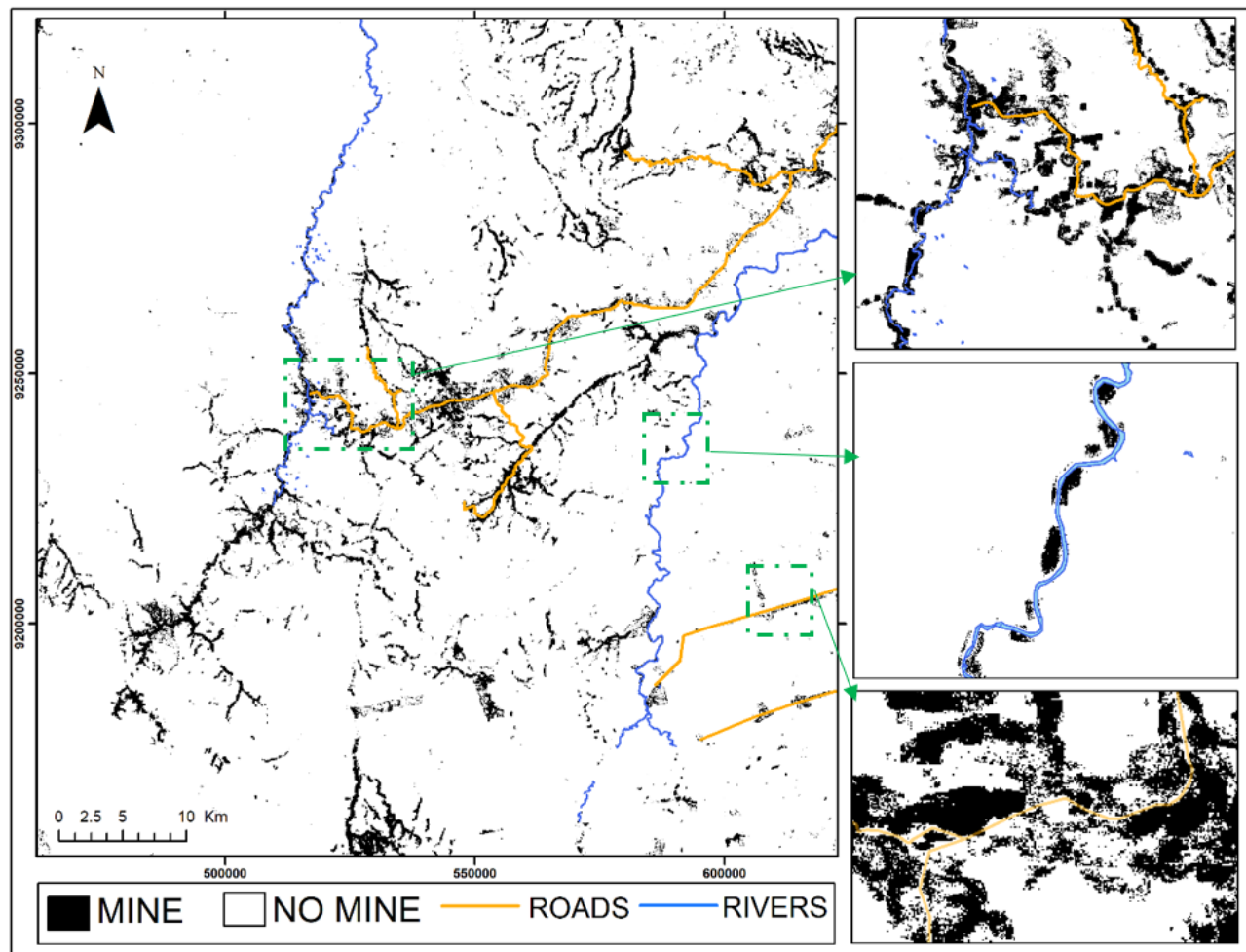


Figure 35. Binary Classification using Random Forest Classifier

4.5 Probabilistic Random Forest Classification

Random Forests is a practical machine learning ensemble approach that provides accurate predictions for classification and regression (DeFries & Chan, 2000). Nevertheless, since the target output is predicted probabilities of ASGM rather than membership of one belongs group or class, a probability class estimation was performed. It is relevant to estimate the probability of belonging to each class when the threshold between classes is not clearly defined in the landscape and when transition areas from one class to another are fuzzy (DeFries & Chan, 2000). This might also be interesting to know the sampling's class membership probability, which is an important fact for stakeholders and the implementation of further strategies. In that sense, the preference to have the probability of ASGM presence rather than the simple knowledge that class belonging seems more suitable for decision making. Logistic regression models, vote counting, and probability machines are the most traditional methods for probability estimation in the RF (Corcoran et al., 2013b). According to Bostrom, (2007), average vote performs better for two-class problems ($K=2$) than logistic regression or relative

class frequency. Therefore, it was the method selected for estimating probabilities of ASGM occurrence.

The counting votes of the trees define the class probability in the ensemble by averaging the unweighted class votes by the ensemble members (Boström, 2007). Each member vote for a single class, and the fraction of trees that vote for a particular class is calculated, choosing the most probable class. Figure 36 shows the final classification using the RF classifier with probability output. It is a pixel basis classifier; therefore, for every pixel in the AoI, an ASGM presence probability was estimated in percentage terms. Subsequently, six probability intervals were defined for smoothing purposes and further comprehension for potential stakeholders.

The probability of belonging to a particular class (Mine / no Mine) is calculated in the RF machine learning algorithm considering the relative class frequency votes in the ensemble for the two classes. RF does majority voting among all its trees to predict the class of any sample, telling about the fraction of the total number of trees which votes for the specific class, selecting any data point which is greater than 0.5 used as a cutoff. If the sample is greater than the cutoff, it is assigned to ASGM with a certain probability (Breiman, 2001). Figure 37 shows the probability occurrence for the ASGM class in the study area. Figure 38 depicts a reclassification of the probabilities for better understanding and representation.

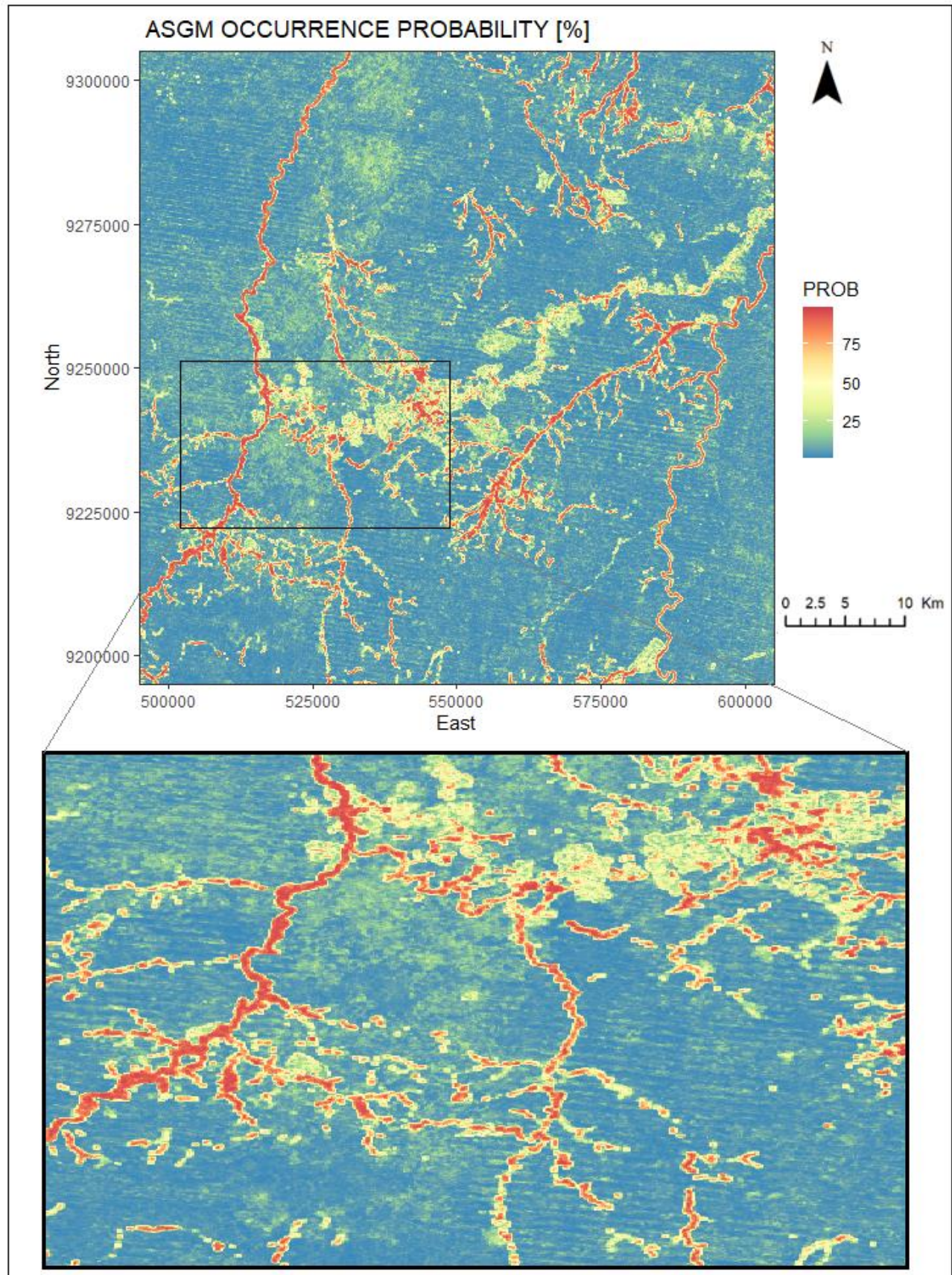


Figure 36. ASGM Occurrence Probability in percentage (%)

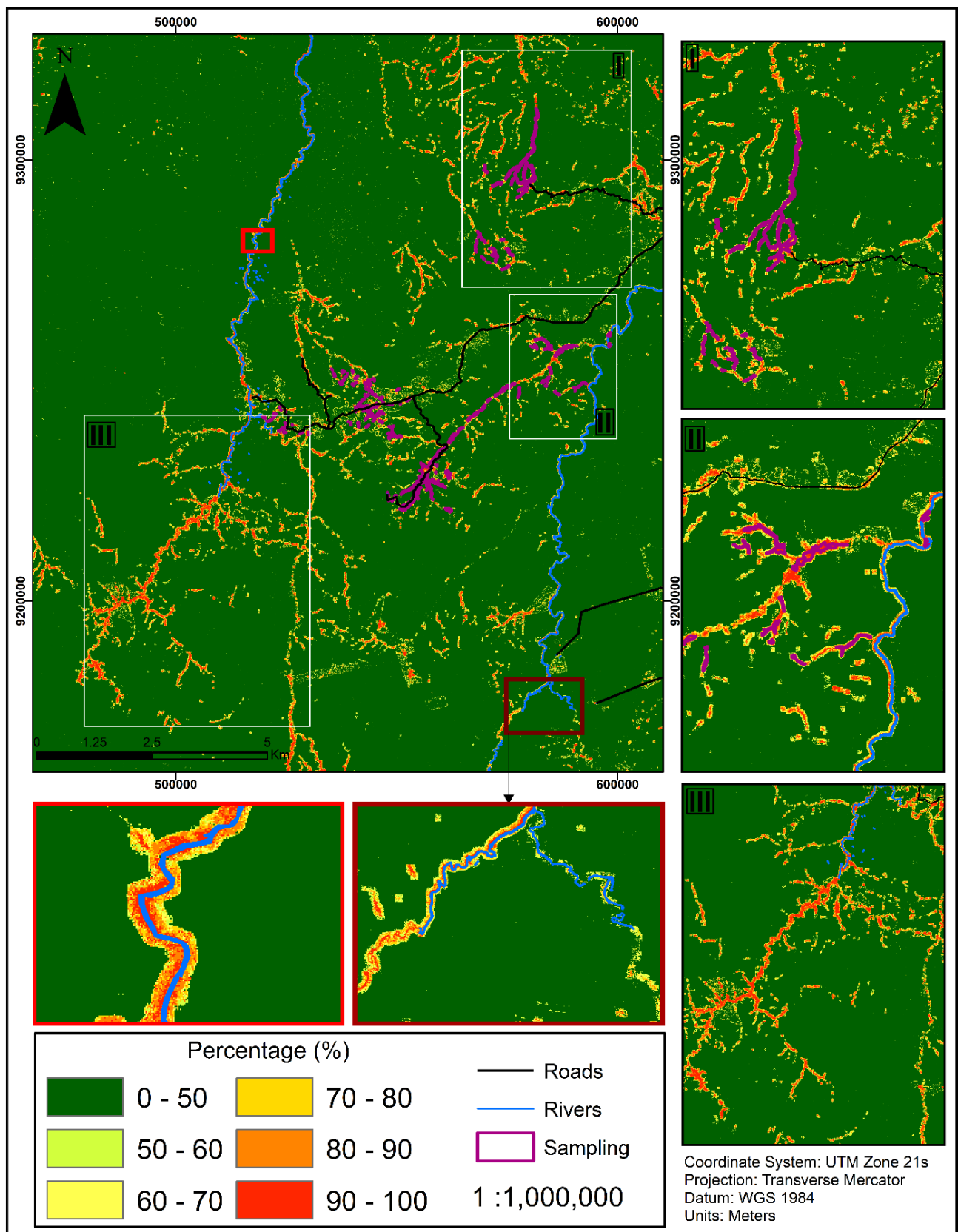


Figure 37. ASGM Occurrence Probability Multiclass Percentage

4.6 Change Detection

The LandTrendr algorithm allows the detection of forest disturbances using temporal segmentation. After estimating the magnitude of change at pixel basis using the spectral signature, the year of change is calculated considering the vertex of the magnitude of the change vector. Figure 38 renders the year of change using the RGB triangle representation. Pixels with red color are pixels whose change was in 2010. The green color represents changes in 2010 and the blue color in 2019. The RGB representation allows calculating the year and epoch of the land cover change and forest disturbance. Yellow color represents changes from 2000 to 2010, pixels colored in cyan renders changes because of ASGM from 2010 and 2019.

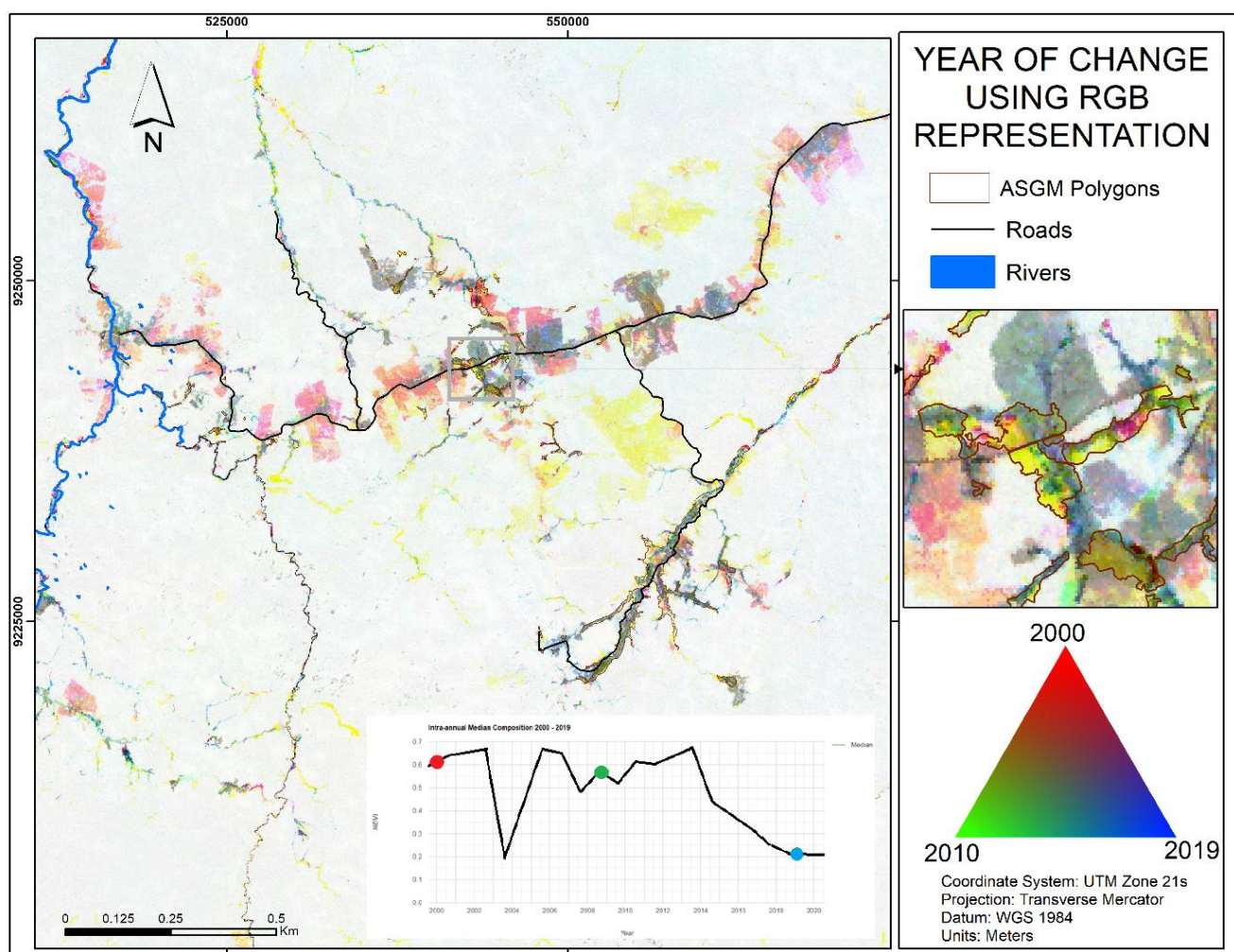


Figure 38. Year of Detection using RGB representation (R:2000, G: 2010, B: 2019)

4. DISCUSSION

The current research describes a process for mapping and detecting ASGM settlements in the Amazon Forest using Landsat time series with ancillary information as data input. In this research, the Random Forest was used as a classifier and the LandTrendr algorithm to investigate the spectral trends of the multispectral and textural features. This research represents the first attempt to map and monitor the ASGM activities using multifeatured analysis with temporal segmentation of dense Landsat time series on the GEE platform. The cloud computing environment allows handling multidimensional datasets, multifunctional data processing, and straightforward statistics extraction. Moreover, a variable importance selection was carried on using the VSURF package for feature reduction and variable importance assessment, cutting down the final model free of redundancy and noise, and achieving notable results and acceptable accuracy (above 90%) with almost one-third of the initial set of variables.

The LandTrendr algorithm has previously proven to be effective for the detection of forest disturbances and recovery (Zhu et al., 2019), (Fragal et al., 2016), (Hislop et al., 2019), but its usability to detect particularly disturbances associated with ASGM has not been used to the knowledge of this study. Therefore, this research seems to be the first attempt to monitor this particular forest disturbance using the LandTrendr for temporal segmentation. Showing a notable performance through a semi-automated approach to recognize the multiple variations, environmental impact evidence, and breakpoints detection in long-term trends, reducing the noise significantly, differences in illumination and atmospheric conditions, phenological changes, and geometric registration (R. Kennedy et al., 2018).

This analysis finds clear evidence that LandTrendr throughout temporal segmentation of multifeatured for ASGM detections is a reliable method for monitoring this type of forest disturbances that is worth considering as follows. (i) it can be applied over any remote sensing image as input with limited support of validation data, assuring broad applicability, especially for places not easily accessible or limited ground-truth such as the Amazon Forest (Y. Yang et al., 2018). (ii) the temporal segmentation process allows to detect land cover changes year by year by the spectral trajectory in a temporal profile, which could also inform about the magnitude of the change and the year of detection, in contrast with traditional multitemporal remote sensing classification approaches. (iii) The LandTrendr outputs can be used for spatial extent, pattern, and degree assessment of the land-cover-change-recovery process, allowing to understand the dynamics of the ecosystem in a spatially explicit form (Y. Yang et al., 2018). (iv) given that forest disturbances are related to subtle or gradual land cover changes that can easily be confused with phenological or natural fluctuations, the magnitude of change for abrupt change detection because of ASGM allows to identify and discriminate the changes related to anthropogenic activities. (v) The approach conducted incorporating RF with multiple spectral time series trajectories enables to enhance the classification by harnessing differential sensitivities captured by different temporal segmentations simultaneously. Combining a suite of single data features retrieved from the use of multiple spectral and textural features temporal segmented. (vi) The RMSE and fit-to-vertex metrics ensure that multiple linear regression used for segmentation are faithful representations of changes because of forest disturbance, in this

case, ASGM activities. Maintaining consistency in predictive mapping through time and, consequently, the classification, omitting minor subtle changes that might affect overall accuracy. Finally, the temporal representation through the temporal segmentation and use over any remote sensing image ensures extended monitoring by appending new satellite images in the future, which meant that the disturbance and recovery process of the ASGM is detectable continuously, for futures reports of ASGM regulation and formalization process as it is required in and sustainable management context. Consequently, a monitoring system can be directly implemented and sequentially extended to assess ASGM progress in NAP (National Action Plan – Minamata Convention) incorporation.

Some previously published studies (Xu et al., 2019), (Y. Yang et al., 2018) and (Dlamini & Xulu, 2019) that have implemented the LandTrendr for mining activities had separately relied on evaluating single spectral information for change detection analysis, a bit of motivated because the LandTrendr only allows using one spectral feature per run. Obtaining different results that cannot depict the forest disturbance completely and separate similar spectral classes. Since the use of a single spectral index might induce gaps, biased and discontinuity, and affect the interannual land cover changes assessment by spectral trajectories through the time series (Mugiraneza et al., 2020). Moreover, mining activities such as ASGM are evident in several different biophysical factors that need to be analyzed holistically and cannot entirely depict using a singular spectral variable. In contrast, the use and combination of multispectral and textural features in characterizing the land cover changes seems reasonably reliable as this approach attempted. Since the proposed method considers the different surface characteristics and heterogeneity impacts analyzed from different spectral approaches and includes spatial information (Cohen et al., 2017). Moreover, the usability and combination of different spectral indices have been considered as a better indicator for land cover changes than a single spectral index because they can reduce the topography and atmospheric influence on the surface reflectance and can amplifier some particular, specific, and desired effects of interest for ASGM detection, (Liu et al., 2017). Multiple Spectral indices allow retrieving and assessing information regarding the vegetation greenness, soil moisture, vegetation moisture, vegetation liquid water content, or water flow, providing complementary, interrelated, and independent insights about the forest disturbance because of ASGM activities (Deng et al., 2007). The singular spectral assessment by vegetation indices or spectral bands might induce misclassifications and detection issues since the class spectral heterogeneity reduces the probability of proper identification given the variability of spectral responses and mix of land covers presented traditionally in the ASGM settlements. The spectral similarity with other land covers provides another restriction for the sole use of spectral information; since the class threshold is not recognizable in a feature space directly, the overlapping in multiple spectral spaces causes mislabeling of the features, and therefore a false detection.

The study has shown that NDVI was the most important variable in the feature reduction using RF for variable selection. This finding is in line with previous researches (Jin et al., 2018), where NDVI has been used to detect land degradation activities – among other things- such as deforestation (Asner, 2009), soil erosion (del Río-Mena et al., 2020), droughts (Liu et al., 2017), and vegetation burning (Key & Benson, 2006). Changes due to deforestation or sedimentation are directly related to decreasing values of NDVI through the time series; the higher the impact, the lower the value of the index, and therefore, the higher the magnitude value in the temporal segmentation in LandTrendr. Therefore, the analysis of NDVI values for

areas mined at different periods indicates disturbed areas in a timeframe, as it was depicted in the PDP plot (figure 33). Similarly, NBR was another important spectral index selected in the feature reduction. The index has been used in capturing the spatial complexity of severity within wildfires boundaries (Hislop et al., 2019). The process by which land is historically cleaned has been used in illegal mining hotspots (Salman & de Theije, 2017). High values are linked with changes in the amount of live green vegetation, moisture content, and soil conditions that may occur after ASGM settling. Another important spectral index selected was NDMI, which provided a complementary metric for effects related to land surface temperature quantitatively over forest areas with high impact due to mining disturbances and accelerated sediment accumulation processes.

This research has used the variable importance mean decrease error (value) as threshold metric on the whole set of features; then, on the relevant subset of features, it has applied a wrapper considering variable importance standard deviation and the ΔMSE (value) for prediction model with the final set of best predictors (table 13). Seven out of the top ten predictors are features related to texture features, which explains that the ASGM detection better exploits the spatial complexity of mixed classes than a solely spectral analysis. Since the temporal segmentation of texture features provides unique insights about the changes of the spatial relationships and for distinguishing land cover classes with similar spectral characteristics but with different spatial configurations. Moreover, the temporal segmentation of the texture features contributes to assessing the spatial-temporal changes that occur in small patches with multiple land covers (the main characteristic of ASGM) whose classification by spectral feature space is quite limited considering the wideband of the spectral bands and the spatial resolution of the images (Ramola et al., 2020). The texture features retrieved by the GLCM matrix complement the spectral variables derived from the spectral indices in the classification and detection process of forest units with high spectral heterogeneity and different vegetation densities (Ruiz et al., 2004).

Cluster Prominence texture (Prom) was the most representative feature among all the most important features. B5_Prom (B5 = Swir 1), B7_Prom (B7 = Swir 2) are in the top ten of most important predictors, while B4_prom (B4 = Nir), B2_prom (B2 = Green) are in the twelve and fourteen positions respectively (figure 31, table 13). It can be explained since cluster prominence is an asymmetry indicator. The higher the cluster prominence value, the more asymmetric the image is, the higher the spatial heterogeneity and the higher the spectral variability in the analysis window (X. Yang et al., 2012). This can also be shown by the partial dependence plot (figure 33) where the marginal probability of the B5_prom predictor is high if the prom's value is also high, showing a monotonic function where the probability of ASGM occurs is directly proportional to the value of the cluster prominence.

Consequently, if the value is low, there is a low probability and a peak around the mean values in the GLCM matrix and, therefore, a slight variation in gray-scale values. This asymmetry indicator is particularly handy for distinguishing different land covers represented by gray-scale levels in small analysis patches. Moreover, the temporal segmentation provides additional information about the temporal change of those multiple land covers (gray-scale levels asymmetry) in small patches along the time. Allowing to relate the spatial (texture) and temporal (segmentation) changes in an area with multiple land covers and, therefore, different spectral responses produced by ASGM activities.

Among the twelve textural features, Cluster Prominence, Cluster Shade, Variance and Contrast seemed to be most promising features for ASGM detection due their relative large separation, small standard deviation (X. Yang et al., 2012), variable importance metrics, and performance in the binary classification. Cluster shade is a skewness indicator of the matrix, measuring the uniformity of the image and its intrinsically linked to the Cluster Prominence; the higher the shade values, the lower the uniformity, the lower the skewness (Unser, 1986). The metric was proposed by Connors et al. (1984) to relate it directly with the Cluster Prominence texture. Indicating that high values of both metrics are clear evidence of multiple land cover in small local spaces with high spectral heterogeneity and high image asymmetry. It also can be seen through the PDPs plots (figure 33), where the relation of the Cluster Shade concerning the marginal probability of ASGM occurrence is high for elevated shade values.

The variance and contrast textures are linked directly and provide information about the image variability. High variance values seemed to suggest a high contrast while the opposite relationship does not apply; both are related to local and global variability, respectively. A high variance value indicates high heterogeneity of the gray-scale values – differ from their mean and the contrast measures the local variations presented in the image. The contrast texture is also a representation of the difference between the lowest and the highest values over a continuous local area formed by a window (kernel) of analysis.

These results suggest that the study area possesses complex texture and large variations, while the cluster prominence and cluster shade indicate constant asymmetry and high spectral variability. Figure 37 (panel (iii)) shows the spectral variability and the high asymmetry at the nearby areas of the ASGM settlements. The multiple different impacts of the land cover in small areas produced multiples spectral and therefore spatial relations are mainly detected by using these four spectral features.

Texture information derived from the SWIR bands worked better since they have yielded the most exemplary characteristics about the spatial relationships of neighboring pixels which attributed to changes in the land cover, since SWIR bands have contrast in their imagery that make objects easily recognizable, discriminating moisture content of soil and vegetation and less sensitive to atmospheric influence. The window size selected for texture calculation (3x3) might introduce some noise, considering that the bigger the kernel, the smoother the texture image (Chen et al., 2020). However, the kernel size was selected considering the smallest size of the ASGM (no higher than 1ha) and the constantly spatial variation in small patches produced by different land cover impacts than a higher kernel might smooth, reducing the sharpening with a spatial feature is identified. The main drawback of introducing texture features in the analysis is the border effect, given that the calculation of every metric independently presents significant errors in transition areas and the appropriate delimitation of the kernel size for texture extraction. Nonetheless, the achieved results reveal that the highest the contrast is, the more information is obtained from the texture analysis, which notably enhances the discrimination ability and identification of the ASGM by the temporal segmentation of texture features and the capture of spatial complexity of mixed classes.

Severe changes in land cover due to deforestation or excavation of the topsoil layer are best detected in bands 5 (Swir 1) and 7 (Swir 2) of Landsat. These bands observe the reflectance of solar radiation between $1.60\mu\text{m}$ and $2.19 - 2.22 \mu\text{m}$. In this range, the spectral signature of vegetation is considerably different from that of bare soil or cleared and logging patches

because of deforestation. This difference is beneficial for identification and discrimination from land covers with vegetation and those without, and this spectral zone is susceptible to forest structure, moisture, shadowing, and vegetation density. This application of the SWIR bands is well supported by (Mitchell et al., 2017), (Asner, 2009), (Gerard et al., 2003) that rely on SWIR bands for forest disturbance detection because they are not affected by haze or other noises as the RGB bands, and because SWIR bands in remote sensing occur in the atmospheric windows, offering unique opportunities for sensitive information regarding leaf moisture content, mineral chemistry and perform analysis that is not possible with visible and near-infrared alone.

Elevation and distance to roads were the only important features included in the final model built by the variable importance and feature reduction method with VSURF. A remarkable consideration explains the relevance of these two features: Firstly, most of the 75 % of the Amazon ASGM are alluvial mines located close to the shorelines and rarely in the middle of the forest (Elmes et al., 2014). Secondly, the rudimentary roads interconnect the ASGM locations for mineral transportation and mining supplies (Güiza, 2013), which are built to foster the ASGM activities (Roulet et al., 2001). Consequently, the relevance of ancillary data as an essential input in the ASGM detection cannot be argued in the light of the results achieved, given the spatial correlation of the water bodies and the roads in the ASGM distribution. Nevertheless, the fact that topography and vegetation relationships are influenced by other environmental factors – out of this scope- feature relevance and feature selection indicates that the connection needs to be understood in a broader context (Deng et al., 2007). Previous studies have pointed out the influence of topographic features and the spatial scale effects of detecting forest disturbances (Deng et al., 2007), (Qi & Wu, 1996) (Aman et al., 1992). The main issue concerns the spatial scale (30m). Given that the spatial resolution of the data derived from the SRTM and used in the analysis might not represent the scale at which the ASGM correlates with topography features, and that the spatial patterns observed might not inform about the contextual ASGM activities that involve the characterization in large areas used in this research. Analyzing a more continuous surface and higher-order or spatial resolution provides better sights of the landscape structure between topographic attribute and vegetation variables and, therefore, correlation with forest disturbances.

The Random Forest algorithm generally performs well with a high dimensional classification framework allowing nonlinear relationships among predictors (Mellor et al., 2015). Nevertheless, the input predictors present high correlation (spectral indices), collinearity, and spatial correlation (texture features derived from the GLCM matrix) required to be mitigated. Therefore, identified the strong predictors that do not decrease the overall accuracy of the ASGM detection, but also diminished the correlation and collinearity among some predictors. When using the VSURF, the dimensionality, variable correlation of the dataset is well reduced by selecting only the most important features while the classification accuracies slightly change; 89.2% by 86 variables, 92.6% by 49 features, and 90.8% by 33 variables, (table 14) suggesting that feature reduction did not impact predictive ability, but feature redundancy and noise (figure 34). The stepwise procedure and wrapper method includes statistical measures such as the variable importance standard deviation, variable importance mean decrease error and the coefficient of variation for feature reduction and selection the most important predictors and reducing the correlation among the predictors. Although these variables are not especially predictors, their usability to establish a threshold and assess the relationships with other variables seems fundamental for feature reduction and selection, since it constructs several

models for training purposes, implying that the selection is made in a way that captures the whole variability of the predictors considering for modeling removing biased selection in favor of particular predictors (Iguayon et al., 2003). The multicollinearity and spatial autocorrelation was overlooked given that RF uses the bootstrap sampling and feature sampling, selecting different set of features for different ensembles in the forest (Corcoran et al., 2013).

Two classifications (binary and probabilistic) were carried on using the Random Forest classifier. The binary Mine / No Mine classification performs an overall accuracy of 90.8% using 50 iterations with the most important predictors selected after using VSURF. The qualitative assessment shows that land covers with similar surface reflectance responses were - partially- separated. For instance, adjacent areas to rivers with sediments or sandbank, spectrally similar to topsoil, overburden, and mining pit c were classified correctly as No-mine (figure 35), which presumes and notable advance in ASGM mapping compares to (Isidro et al., 2017) and the limitations founded by (F. de L. Lobo et al., 2018), where the spectral analysis was not allowed to separate this classes. This remarkable result is given for the incorporation of texture features as predictors in the RF classification process. Moreover, the binary classification. However, this binary classification fails in the discrimination of the deforested patches and the ASGM settlements. This is induced for the complexity of separate areas mining areas from logging patches, which could be or not directly linked with ASGM activities. Moreover, it is important to recognize that the ASGM are abstract objects with fuzzy boundaries and multiple land covers, which as a whole constituted the concept of ASGM creating large footprints of bare soil and mining ponds. In contrast to other forest disturbances such as like cattle ranching or cropping, where the spectral variability and the spatial context could be defined by some boundaries. In that sense, the probability approach seems reasonable to the spatial display of the occurrence probability of the ASGM class and a visualization tool of the dynamic change and further hypothesis formulation.

The probability map (figure 36, 37) shows the spatial distribution of the ASGM occurrence. Qualitatively, it is possible to see that the highest probabilities are associated with water bodies, as expected. Considering the most of the mines in the sampling data set are alluvial mines (RAISG, 2020). Moreover, the location of mining ponds and the neediness of water for mineral extraction foster the location of ASGM along the rivers. It is important to remark that the model, in some areas, can separate mineral deposits from ASGM settlements along the rivers (figure 37 brown square) despite the high concentration of sediments of the Tapajos tributes rivers (F. L. Lobo et al., 2015), which can be classified as ASGM given their spectral characteristics. Besides, the time of analysis (middle June - middle October) also defines the probability of ASGM occurrence, where most of the tributary rivers at the Tapajos basin experience a change of water siltation through the time frame of this analysis (dry season), coupled with low water flow and an increase of total suspended solids (F. L. Lobo et al., 2015); and considering to Ipenza et al. (2014) where at the end of the rainy season (early/middle June) mining activities are intensified.

Another important feature of this approach is the recognition of the deforested patches (regular squares and pattern distribution through the roads (light yellow) figure 36) with a low-medium probability that, given their characteristics of shape and association are easily recognizable as No Mine areas, but high forest disturbed spots that cannot be directly linked with ASGM activities.

4.1 LIMITATIONS

Given the nature of the problem, the informality related to and scattering pattern of distribution of the ASGM settlements, this pilot study has found some limitations described as follows. Data acquisition for training and validation purposes is the main limitation in model building for mapping and monitoring this type of forest disturbances (Wagner, 2016). Moreover, the relation of ASGM activities with organized delinquency bands (Ipenza et al., 2014) limited the process of an intensive and more specific sampling for model validation. Furthermore, the boundaries delimitation of the ASGM in the digitization process is subjective, inconsistent, and labor-intensive by the photo interpreter even if the process is rigorously carried on following the techniques proposed by (Avery, 1969), (Stone, 1964). Therefore, a potential alternative to improve the quality of the sampling for training and validation purposes is to implement an automated process (segmentation) to delineate homogeneous stands of ASGMs (Thompson et al., 2008), which have the potential to aid in the rapid utilization of extensive historical records with several caveats for future consideration (Morgan et al., 2013). On the other hand, the final set of the features reached for the prediction model after variable reduction and selection is slightly high (33 features), which means that most features explain the minimal variance, as shown in figure 31. Therefore, an extra assessment of model performance with fewer features could be incorporated to evaluate a potential reduction in the final number of predictors, using a different metric rather than delta mean square error per variable used in the current scope.

Considering the volume of features to process and images required for the temporal segmentation in the time series and subsequent classification using RF, the bulk of information requires an automatized process with tailor-made controls that guarantee the optimal outcome. Additionally, it is essential to consider detectors failure at the Landsat-7 ETM+, which provides noise and errors in the predictor's outcome for yearly composite, and even despite that LandTrendr algorithm incorporates an interpolation process for temporal segmentation, the influence of the failure detector is particularly remarkable in the extraction and calculation of the texture features. In light of the results and considering the qualitative characteristics of the images resultant from temporal segmentation, it seems that the interpolation process has not been pretty successful. The gaps because of SLC-off are evident in most of the images and inputs used in the RF classification, which biased the final classification. However, given the adaptability of the LandTrendr and usability with any remote sensing image, the incorporation of the satellite images Landsat 5 and Landsat 7 (open source) in the first decade of the new millennium provides an alternative to overcome the gap. Finally, the model requires an additional and independent validation for the probabilistic classification, which was out of the aims and scope of the current research.

4.2 IMPLEMENTATION

The approach proposed in this work proves an efficient and direct method for ASGM detection. The use of the GEE allows multifunctional data processing eliminating the onerous data acquisition, management, and preprocessing steps in a cloud computing environment, allowing to manipulate big geospatial data and access to real-time satellite data in a high-end computational process, independently of the hardware capacity. LandTrendr is perfectly functional in the GEE environment (LT-GEE), and it counts with a user-friendly API for statistics extraction and interactive visualization (R. Kennedy et al., 2018). The LT-GEE environment has been used for land cover reconstruction and monitoring in forest disturbances, and it raised as a potential option for monitoring and detecting ASGM in the whole rain forest. The transferability over other areas is a topic for further research and is highly suggested to assess its performance in other areas with different environmental and climatological conditions. Nevertheless, the workflow, methodology, and results achieved in this research arise as a real potential option for forest management, and monitoring of the ASGM activities in the Amazon Forest over an open-source platform with freely accessible data and an automatized process in a cloud environment are advantages and benefits that is reasonable to assume that could be successfully implemented for making decisions.

5. CONCLUSIONS

This research presents an efficient and quick ASGM mapping and monitoring method using the LandTrendr for temporal segmentation analysis, VSURF for feature reduction and variable importance, and machine learning Random Forest for probabilistic ASGM occurrence Tapajos river basin. Considering the approach and method to detect mining activities in the Brazilian Amazon currently available on visual interpretation of aerial photographs (F. de L. Lobo et al., 2018), the initial contribution of this research is the development of freely accessible data processed in an open-source platform with an automatized method to derive features and variable predictors and subsequently classification with notable accuracy. Moreover, it reduces image processing time with a cost-effective method. Furthermore, it demonstrates the usefulness of the ensemble approach using the Random Forest machine learning algorithm for multifeatured and different sorts of predictors, which enables to assess the classification precision.

The proposed method's major novelty lies in identifying ASGM using time series with temporal segmentation of multifeatured spectral and textural features. It appears to be a feasible and robust approach to detect the forest disturbances produced by ASGM activities, using a linear regression-based-trajectory-fitting that allows recognizing long processes of land change cover and long-term land monitoring system. The temporal segmentation of texture features mainly provides unique insights about the changes of the spatial relationships and the importance of textural analysis for distinguishing land cover classes with similar spectral characteristics but with different spatial configurations, patterns, and local pixel associations with neighbors. The analysis performed of variable importance and feature reduction shows the preponderance of the texture features via temporal segmentation and magnitude of change parameter from the GLCM matrix variables to identify disturbances due to ASGM, which addressed an important gap in the current forest disturbances literature.

Another notable contribution of this study was the ability to assess the importance and marginal effect of different variables have on the ASGM prediction and select the features that combined over a tree ensemble model allows predicting the occurrence (presence) of ASGM in probabilistic terms, providing a promising alternative to the current labeling and static land cover class approach employed in complex spatial areas with fuzzy boundaries, and multi-type of land cover interacting together in small patches of the forest. Therefore, the probabilistic approach presented as the final result tries to solve the problem related to the fact that ASGM activities are not a singular land cover class. It is an abstract phenomenon recognizable in the space by associating an amalgamation of different land covers with a set of dynamic and temporal processes. Labeling the phenomenon in a single land cover class minimizes and cuts down the spectral variability in the analysis and what the problem represents.

6. REFERENCES

- Almeida-Filho, R., & Shimabukuro, Y. E. (2002). Digital processing of a Landsat-TM time series for mapping and monitoring degraded areas caused by independent gold miners, Roraima State, Brazilian Amazon. *Remote Sensing of Environment*, 79(1), 42–50. [https://doi.org/10.1016/S0034-4257\(01\)00237-1](https://doi.org/10.1016/S0034-4257(01)00237-1)
- Alvarez Berrios, N. L., & Mitchell Aide, T. (2015). Global demand for gold is another threat for tropical forests. *Environmental Research Letters*, 10(1), 014006. <https://doi.org/10.1088/1748-9326/10/1/014006>
- Aman, A., Randriamanantena, H. P., Podaire, A., & Frouin, R. (1992). Upscale Integration of Normalized Difference Vegetation Index: The Problem of Spatial Heterogeneity. *IEEE Transactions on Geoscience and Remote Sensing*, 30(2), 326–338. <https://doi.org/10.1109/36.134082>
- AMAP/UN Environment. (2018). *Global Mercury Assessment 2018: Key Findings*. Retrieved from <https://www.apmap.no/documents/doc/technical-background-report-for-the-global-mercury-assessment-2018/1815>
- Asner, G. P. (2009). Automated mapping of tropical deforestation and forest degradation: CLASlite. *Journal of Applied Remote Sensing*, 3(1), 033543. <https://doi.org/10.1117/1.3223675>
- Asner, G. P., Llactayo, W., Tupayachi, R., & Luna, E. R. (2013). Elevated rates of gold mining in the Amazon revealed through high-resolution monitoring. *Proceedings of the National Academy of Sciences of the United States of America*, 110(46), 18454–18459. <https://doi.org/10.1073/pnas.1318271110>
- Asner, G. P., & Tupayachi, R. (2017). Accelerated losses of protected forests from gold mining in the Peruvian Amazon. *Environmental Research Letters*, 12(9), 094004. <https://doi.org/10.1088/1748-9326/aa7dab>
- Asrar, G., Kanemasu, E. T., & Yoshida, M. (1985). Estimates of leaf area index from spectral reflectance of wheat under different cultural practices and solar angle. *Remote Sensing of Environment*, 17(1), 1–11. [https://doi.org/10.1016/0034-4257\(85\)90108-7](https://doi.org/10.1016/0034-4257(85)90108-7)
- Avery, T. E. (1969). *Forester's Guide To Aerial Photo Interpretation*. US Department of Agriculture, Forest Service.
- Belgiu, M., & Drăgu, L. (2016, April 1). Random forest in remote sensing: A review of applications and future directions. *ISPRS Journal of Photogrammetry and Remote Sensing*, Vol. 114, pp. 24–31. <https://doi.org/10.1016/j.isprsjprs.2016.01.011>
- Boström, H. (2007). Estimating class probabilities in random forests. In *Proceedings - 6th International Conference on Machine Learning and Applications, ICMLA 2007*. <https://doi.org/10.1109/ICMLA.2007.45>
- Breiman, L. (2001). Random forests. *Machine Learning*, 45(1), 5–32. <https://doi.org/10.1023/A:1010933404324>
- CAMEP. (2013). Mercury in Madre de Dios. Mercury Concentrations in Fish and Humans in Puerto Maldonado. In *Carnegie Institution for Science*. Retrieved from https://www-legacy.dge.carnegiescience.edu/research/CAMEP/CAMEP_Research_Brief_-_Puerto

Maldonado English - FINAL.pdf

- Champion, I., Dubois-Fernandez, P., Guyon, D., & Cottrel, M. (2008). Radar image texture as a function of forest stand age. *International Journal of Remote Sensing*, 29(6), 1795–1800. <https://doi.org/10.1080/01431160701730128>
- Chen, S., Useya, J., & Mugiyono, H. (2020). Decision-level fusion of Sentinel-1 SAR and Landsat 8 OLI texture features for crop discrimination and classification: case of Masvingo, Zimbabwe. *Heliyon*, 6(11), e05358. <https://doi.org/10.1016/j.heliyon.2020.e05358>
- Clausi, D. A., & Zhao, Y. (2002). Rapid extraction of image texture by co-occurrence using a hybrid data structure. *Computers and Geosciences*, 28(6), 763–774. [https://doi.org/10.1016/S0098-3004\(01\)00108-X](https://doi.org/10.1016/S0098-3004(01)00108-X)
- Cohen, W. B., Healey, S. P., Yang, Z., Stehman, S. V., Brewer, C. K., Brooks, E. B., ... Zhu, Z. (2017). How Similar Are Forest Disturbance Maps Derived from Different Landsat Time Series Algorithms? *Forests*, 8(4), 98. <https://doi.org/10.3390/f8040098>
- Cohen, W. B., Yang, Z., Healey, S. P., Kennedy, R. E., & Gorelick, N. (2018). A LandTrendr multispectral ensemble for forest disturbance detection. *Remote Sensing of Environment*, 205, 131–140. <https://doi.org/10.1016/j.rse.2017.11.015>
- Conners, R. W., Trivedi, M. M., & Harlow, C. A. (1984). Segmentation of a high-resolution urban scene using texture operators (Sunnyvale, California). *Computer Vision, Graphics, & Image Processing*, 25(3), 273–310. [https://doi.org/10.1016/0734-189X\(84\)90197-X](https://doi.org/10.1016/0734-189X(84)90197-X)
- Corbett, T., O'Faircheallaigh, C., & Regan, A. (2017). 'Designated areas' and the regulation of artisanal and small-scale mining. *Land Use Policy*, 68, 393–401. <https://doi.org/10.1016/j.landusepol.2017.08.004>
- Corcoran, J., Knight, J., & Gallant, A. (2013a). Influence of Multi-Source and Multi-Temporal Remotely Sensed and Ancillary Data on the Accuracy of Random Forest Classification of Wetlands in Northern Minnesota. *Remote Sensing*, 5(7), 3212–3238. <https://doi.org/10.3390/rs5073212>
- Corcoran, J., Knight, J., & Gallant, A. (2013b). Influence of Multi-Source and Multi-Temporal Remotely Sensed and Ancillary Data on the Accuracy of Random Forest Classification of Wetlands in Northern Minnesota. *Remote Sensing*, 5(7), 3212–3238. <https://doi.org/10.3390/rs5073212>
- Dash, J., Mathur, A., Foody, G. M., Curran, P. J., Chipman, J. W., & Lillesand, T. M. (2007). Land cover classification using multi-temporal MERIS vegetation indices. *International Journal of Remote Sensing*, 28(6), 1137–1159. <https://doi.org/10.1080/01431160600784259>
- DeFries, R. S., & Chan, J. C. W. (2000). Multiple criteria for evaluating machine learning algorithms for land cover classification from satellite data. *Remote Sensing of Environment*, 74(3), 503–515. [https://doi.org/10.1016/S0034-4257\(00\)00142-5](https://doi.org/10.1016/S0034-4257(00)00142-5)
- del Río-Mena, T., Willemen, L., Tesfamariam, G. T., Beukes, O., & Nelson, A. (2020). Remote sensing for mapping ecosystem services to support evaluation of ecological restoration interventions in an arid landscape. *Ecological Indicators*, 113, 106182. <https://doi.org/10.1016/j.ecolind.2020.106182>
- Deng, Y., Chen, X., Chuvieco, E., Warner, T., & Wilson, J. P. (2007). Multi-scale linkages between topographic attributes and vegetation indices in a mountainous landscape. *Remote*

Sensing of Environment, 111(1), 122–134. <https://doi.org/10.1016/j.rse.2007.03.016>

Department of the Interior U.S. Geological Survey. (2011). Landsat 7 Science Data Users Handbook Landsat 7 Science Data Users Handbook. In *National Aeronautics and Space Administration*. Retrieved from <https://www.usgs.gov/core-science-systems/nli/landsat/landsat-7-data-users-handbook>

Department of the Interior U.S. Geological Survey. (2016). Landsat 8 Data Users Handbook. In *Nasa* (Vol. 8). Retrieved from <https://landsat.usgs.gov/documents/Landsat8DataUsersHandbook.pdf>

Dlamini, L. Z. D., & Xulu, S. (2019a). Monitoring mining disturbance and restoration over RBM site in South Africa using landtrendr algorithm and landsat data. *Sustainability (Switzerland)*, 11(24), 6916. <https://doi.org/10.3390/SU11246916>

Dlamini, L. Z. D., & Xulu, S. (2019b). Monitoring mining disturbance and restoration over RBM site in South Africa using landtrendr algorithm and landsat data. *Sustainability (Switzerland)*, 11(24), 6916. <https://doi.org/10.3390/SU11246916>

Domingues, M. M., Cury, E. D. T., de Araújo, A. A. K., Junior, J. M. F. C., & da Conceição Nascimento Pinheiro, M. (2019). Somatosensory psychophysic losses in inhabitants of riverside communities of the Tapajós river basin, Amazonas, Brazil: The possible involvement of exposure to methylmercury. *Journal of the Neurological Sciences*, 405, 255–256. <https://doi.org/10.1016/j.jns.2019.10.1287>

Eduful, M., Alsharif, K., Eduful, A., Acheampong, M., Eduful, J., & Mazumder, L. (2020). The Illegal Artisanal and Small-scale mining (Galamsey) ‘Menace’ in Ghana: Is Military-Style Approach the Answer? *Resources Policy*, 68, 101732. <https://doi.org/10.1016/j.resourpol.2020.101732>

Elmes, A., Yarlequé Ipanaqué, J. G., Rogan, J., Cuba, N., & Bebbington, A. (2014a). Mapping licit and illicit mining activity in the Madre de Dios region of Peru. *Remote Sensing Letters*, 5(10), 882–891. <https://doi.org/10.1080/2150704X.2014.973080>

Elmes, A., Yarlequé Ipanaqué, J. G., Rogan, J., Cuba, N., & Bebbington, A. (2014b). Mapping licit and illicit mining activity in the Madre de Dios region of Peru. *Remote Sensing Letters*, 5(10), 882–891. <https://doi.org/10.1080/2150704X.2014.973080>

Farr, T. G., Rosen, P. A., Caro, E., Crippen, R., Duren, R., Hensley, S., ... Alsdorf, D. E. (2007). The shuttle radar topography mission. *Reviews of Geophysics*, 45(2), RG2004. <https://doi.org/10.1029/2005RG000183>

Fauvel, M., Chanussot, J., & Benediktsson, J. A. (2012). A spatial-spectral kernel-based approach for the classification of remote-sensing images. *Pattern Recognition*, 45(1), 381–392. <https://doi.org/10.1016/j.patcog.2011.03.035>

Feng, Q., Liu, J., & Gong, J. (2015). UAV Remote Sensing for Urban Vegetation Mapping Using Random Forest and Texture Analysis. *Remote Sensing*, 7(1), 1074–1094. <https://doi.org/10.3390/rs70101074>

Flood, N. (2013). Seasonal Composite Landsat TM/ETM+ Images Using the Medoid (a Multi-Dimensional Median). *Remote Sensing*, 5(12), 6481–6500. <https://doi.org/10.3390/rs5126481>

Fragal, E. H., Silva, T. S. F., & Novo, E. M. L. de M. (2016). Reconstrução histórica de mudanças na cobertura florestal em várzeas do baixo amazonas utilizando o algoritmo

- landtrendr. *Acta Amazonica*, 46(1), 13–24. <https://doi.org/10.1590/1809-4392201500835>
- Friedman, J. H. (2001). Greedy function approximation: A gradient boosting machine. *Annals of Statistics*, 1189–1232. Retrieved from <https://statweb.stanford.edu/~jhf/ftp/trebst.pdf>
- Gallwey, J., Robiati, C., Coggan, J., Vogt, D., & Eyre, M. (2020). A Sentinel-2 based multispectral convolutional neural network for detecting artisanal small-scale mining in Ghana: Applying deep learning to shallow mining. *Remote Sensing of Environment*, 248, 111970. <https://doi.org/10.1016/j.rse.2020.111970>
- Gao, B. C. (1996). NDWI - A normalized difference water index for remote sensing of vegetation liquid water from space. *Remote Sensing of Environment*, 58(3), 257–266. [https://doi.org/10.1016/S0034-4257\(96\)00067-3](https://doi.org/10.1016/S0034-4257(96)00067-3)
- Genuer, R., Poggi, J.-M., & Tuleau-Malot, C. (2015). VSURF: an R package for variable selection using random forests. *The R Journal*, 7(2), 19–33.
- Gerard, F., Plummer, S., Wadsworth, R., Sanfeliu, A. F., Iliffe, L., Balzter, H., & Wyatt, B. (2003). Forest Fire Scar Detection in the Boreal Forest with Multitemporal SPOT-VEGETATION Data. *IEEE Transactions on Geoscience and Remote Sensing*, 41(11 PART I), 2575–2585. <https://doi.org/10.1109/TGRS.2003.819190>
- Gillanders, S. N., Coops, N. C., Wulder, M. A., & Goodwin, N. R. (2008). Application of Landsat satellite imagery to monitor land-cover changes at the Athabasca Oil Sands, Alberta, Canada. *The Canadian Geographer / Le Géographe Canadien*, 52(4), 466–485. <https://doi.org/10.1111/j.1541-0064.2008.00225.x>
- Gómez, C., White, J. C., & Wulder, M. A. (2016, June 1). Optical remotely sensed time series data for land cover classification: A review. *ISPRS Journal of Photogrammetry and Remote Sensing*, Vol. 116, pp. 55–72. <https://doi.org/10.1016/j.isprsjprs.2016.03.008>
- Griffiths, P., Van Der Linden, S., Kuemmerle, T., & Hostert, P. (2013). A pixel-based landsat compositing algorithm for large area land cover mapping. *IEEE Journal of Selected Topics in Applied Earth Observations and Remote Sensing*, Vol. 6, pp. 2088–2101. <https://doi.org/10.1109/JSTARS.2012.2228167>
- Güiza, L. (2013). LA PEQUEÑA MINERÍA EN COLOMBIA: UNA ACTIVIDAD NO TAN PEQUEÑA. *DYNA*, 80(181), 109–117. Retrieved from <https://revistas.unal.edu.co/index.php/dyna/article/view/35819>
- Güiza Suárez, L., & Aristizabal, J. D. (2013). Mercury and gold mining in Colombia: a failed state. *Universitas Scientiarum*, 18(1), 33–49. <https://doi.org/10.11144/javeriana.sc18-1.mgmc>
- Han, H., Guo, X., & Yu, H. (2016). Variable selection using Mean Decrease Accuracy and Mean Decrease Gini based on Random Forest. *Proceedings of the IEEE International Conference on Software Engineering and Service Sciences, ICSESS*, 0, 219–224. <https://doi.org/10.1109/ICSESS.2016.7883053>
- Haralick, R. M., Dinstein, I., & Shanmugam, K. (1973). Textural Features for Image Classification. *IEEE Transactions on Systems, Man and Cybernetics, SMC-3*(6), 610–621. <https://doi.org/10.1109/TSMC.1973.4309314>
- Hilson, G. (2002). An overview of land use conflicts in mining communities. *Land Use Policy*, 19(1), 65–73. [https://doi.org/10.1016/S0264-8377\(01\)00043-6](https://doi.org/10.1016/S0264-8377(01)00043-6)

- Hilson, G., & Maconachie, R. (2020). Artisanal and small-scale mining and the Sustainable Development Goals: Opportunities and new directions for sub-Saharan Africa. *Geoforum*, 111, 125–141. <https://doi.org/10.1016/j.geoforum.2019.09.006>
- Hinton, J. J. (2006). *Communities and Small-Scale Mining (CASM) Initiative : An integrated review for development planning*. Retrieved from <http://artisanalmining.org/>
- Hislop, S., Jones, S., Soto-Berelov, M., Skidmore, A., Haywood, A., & Nguyen, T. H. (2019). A fusion approach to forest disturbance mapping using time series ensemble techniques. *Remote Sensing of Environment*, 221, 188–197. <https://doi.org/10.1016/j.rse.2018.11.025>
- Horch, A., Djemal, K., Gafour, A., & Taleb, N. (2019). Supervised fusion approach of local features extracted from SAR images for detecting deforestation changes. *IET Image Processing*, 13(14), 2866–2876. <https://doi.org/10.1049/iet-ipr.2019.0122>
- Hu, Y., & Hu, Y. (2020). Detecting Forest Disturbance and Recovery in Primorsky Krai, Russia, Using Annual Landsat Time Series and Multi-Source Land Cover Products. *Remote Sensing*, 12(1), 129. <https://doi.org/10.3390/rs12010129>
- Huete, A., Didan, K., Miura, T., Rodriguez, E. P., Gao, X., & Ferreira, L. G. (2002). Overview of the radiometric and biophysical performance of the MODIS vegetation indices. *Remote Sensing of Environment*, 83(1–2), 195–213. [https://doi.org/10.1016/S0034-4257\(02\)00096-2](https://doi.org/10.1016/S0034-4257(02)00096-2)
- IBGE. (2020). Monitoramento da Cobertura e Uso da Terra. Retrieved May 4, 2021, from Instituto Brasileiro de Geografia e Estatística website: <https://www.ibge.gov.br/geociencias/informacoes-ambientais/cobertura-e-uso-da-terra/15831-cobertura-e-uso-da-terra-do-brasil.html?=&t=notas-tecnicas>
- Ibrahim, E., Lema, L., Barnabé, P., Lacroix, P., & Pirard, E. (2020). Small-scale surface mining of gold placers: Detection, mapping, and temporal analysis through the use of free satellite imagery. *International Journal of Applied Earth Observation and Geoinformation*, 93, 102194. <https://doi.org/10.1016/j.jag.2020.102194>
- Iguyon, I., & Elisseeff, A. (2003). An introduction to variable and feature selection. *Journal of Machine Learning Research*, 3(Mar), 1157–1182. <https://doi.org/10.1162/153244303322753616>
- International Labour Organization. (2018). Una responsabilidad compartida: Las organizaciones de trabajadores en la lucha contra el trabajo infantil y sus peores formas. In *International Labour Organization Report*. Retrieved from http://ilo.org/ipec/Informationresources/WCMS_IPEC_PUB_12893/lang--es/index.htm
- Ipenza, C., & Valencia, L. (2014). *La realidad de la minería ilegal en países amazónicos* (Vol. 1). <https://doi.org/10.13140/RG.2.2.24893.31204>
- Isidro, C., McIntyre, N., Lechner, A., & Callow, I. (2017). Applicability of Earth Observation for Identifying Small-Scale Mining Footprints in a Wet Tropical Region. *Remote Sensing*, 9(9), 945. <https://doi.org/10.3390/rs9090945>
- Jensen, J. R. (1996). *Introductory digital image processing: a remote sensing perspective*. Prentice-Hall Inc.
- Jensen, J. R. (2015). *Introductory digital image processing: a remote sensing perspective* (4th Edito; Pearson Series in Geographic Information Science, Ed.). Los Angeles, CA: Prentice Hall Press.

- Jin, Y., Liu, X., Chen, Y., & Liang, X. (2018). Land-cover mapping using Random Forest classification and incorporating NDVI time-series and texture: a case study of central Shandong. *International Journal of Remote Sensing*, 39(23), 8703–8723. <https://doi.org/10.1080/01431161.2018.1490976>
- Jovanović, D., Govedarica, M., Sabo, F., Bugarinović, Ž., Novović, O., Beker, T., & Lauter, M. (2015). Land cover change detection by using remote sensing - A case study of Zlatibor (Serbia). *Geographica Pannonica*, 19(4), 162–173. <https://doi.org/10.5937/GeoPan1504162J>
- Kennedy, R.E., Yang, Z., Gorelick, N., Braaten, J., Cavalcante, L., Cohen, W.B., Healey, S. (2018). 5 LT-GEE Outputs | LT-GEE Guide. Retrieved February 24, 2021, from Kennedy, R.E., Yang, Z., Gorelick, N., Braaten, J., Cavalcante, L., Cohen, W.B., Healey, S. (2018). Implementation of the LandTrendr Algorithm on Google Earth Engine. *Remote Sensing*, 10, 691 website: <https://emapr.github.io/LT-GEE/lt-gee-outputs.html>
- Kennedy, R. E., Townsend, P. A., Gross, J. E., Cohen, W. B., Bolstad, P., Wang, Y. Q., & Adams, P. (2009). Remote sensing change detection tools for natural resource managers: Understanding concepts and tradeoffs in the design of landscape monitoring projects. *Remote Sensing of Environment*, 113(7), 1382–1396. <https://doi.org/10.1016/j.rse.2008.07.018>
- Kennedy, R. E., Yang, Z., & Cohen, W. B. (2010). Detecting trends in forest disturbance and recovery using yearly Landsat time series: 1. LandTrendr - Temporal segmentation algorithms. *Remote Sensing of Environment*, 114(12), 2897–2910. <https://doi.org/10.1016/j.rse.2010.07.008>
- Kennedy, R., Yang, Z., Gorelick, N., Braaten, J., Cavalcante, L., Cohen, W., & Healey, S. (2018). Implementation of the LandTrendr Algorithm on Google Earth Engine. *Remote Sensing*, 10(5), 691. <https://doi.org/10.3390/rs10050691>
- Key, C. H., & Benson, N. C. (2006). Landscape Assessment (LA) sampling and analysis methods. In *USDA Forest Service - General Technical Report RMRS-GTR*.
- Kupidura, P. (2019). The Comparison of Different Methods of Texture Analysis for Their Efficacy for Land Use Classification in Satellite Imagery. *Remote Sensing*, 11(10), 1233. <https://doi.org/10.3390/rs11101233>
- Lersch, R., Haertel, V., & Shimabukuro, Y. (2007). On the use of ancillary data by applying the concepts of the theory of evidence to remote sensing digital image classification. *International Geoscience and Remote Sensing Symposium (IGARSS)*, 2063–2066. <https://doi.org/10.1109/IGARSS.2007.4423238>
- Li, N., Liu, Y., Liu, S., Liu, F., & Chen, Z. (2014). Port surveillance by using co-occurrence matrix on multi-temporal SAR images. In L. Bruzzone, J. A. Benediktsson, & F. Bovolo (Eds.), *Image and Signal Processing for Remote Sensing XX* (Vol. 9244, p. 924417). <https://doi.org/10.11117/12.2066968>
- Li, P., Jiang, L., & Feng, Z. (2013). Cross-Comparison of Vegetation Indices Derived from Landsat-7 Enhanced Thematic Mapper Plus (ETM+) and Landsat-8 Operational Land Imager (OLI) Sensors. *Remote Sensing*, 6(1), 310–329. <https://doi.org/10.3390/rs6010310>
- Lira, J. (2006). Segmentation and morphology of open water bodies from multispectral images. *International Journal of Remote Sensing*, 27(18), 4015–4038. <https://doi.org/10.1080/01431160600702384>

- Liu, S., Wei, X., Li, D., & Lu, D. (2017). Examining forest disturbance and recovery in the subtropical forest region of Zhejiang Province using landsat time-series data. *Remote Sensing*, 9(5), 479. <https://doi.org/10.3390/rs9050479>
- Lobo, F., Costa, M., Novo, E., & Telmer, K. (2016a). Distribution of Artisanal and Small-Scale Gold Mining in the Tapajós River Basin (Brazilian Amazon) over the Past 40 Years and Relationship with Water Siltation. *Remote Sensing*, 8(7), 579. <https://doi.org/10.3390/rs8070579>
- Lobo, F., Costa, M., Novo, E., & Telmer, K. (2016b). Distribution of Artisanal and Small-Scale Gold Mining in the Tapajós River Basin (Brazilian Amazon) over the Past 40 Years and Relationship with Water Siltation. *Remote Sensing*, 8(7), 579. <https://doi.org/10.3390/rs8070579>
- Lobo, F. de L., Souza-Filho, P. W. M., Novo, E. M. L. de M., Carlos, F. M., & Barbosa, C. C. F. (2018). Mapping Mining Areas in the Brazilian Amazon Using MSI/Sentinel-2 Imagery (2017). *Remote Sensing*, 10(8), 1178. <https://doi.org/10.3390/rs10081178>
- Lobo, F. L., Costa, M. P. F., & Novo, E. M. L. M. (2015). Time-series analysis of Landsat-MSS/TM/OLI images over Amazonian waters impacted by gold mining activities. *Remote Sensing of Environment*, 157, 170–184. <https://doi.org/10.1016/j.rse.2014.04.030>
- Malm, O., Branches, F. J. P., Akagi, H., Castro, M. B., Pfeiffer, W. C., Harada, M., ... Kato, H. (1995). Mercury and methylmercury in fish and human hair from the Tapajos river basin, Brazil. *Science of the Total Environment*, 175(2), 141–150.
- Mapbiomas. (2015). Mapbiomas Brasil. Retrieved April 6, 2021, from Brasil, Projeto de Mapeamento Anual da Cobertura e Uso do Solo no website: <https://mapbiomas.org/o-projeto>
- Marshall, M., Norton-Griffiths, M., Herr, H., Lamprey, R., Sheffield, J., Vagen, T., & Okotto-Okotto, J. (2017). Continuous and consistent land use/cover change estimates using socio-ecological data. *Earth System Dynamics*, 8(1), 55–73. <https://doi.org/10.5194/esd-8-55-2017>
- Martín, A., Arias, J., López, J., Santos, L., Venegas, C., Duarte, M., ... Zambrano, C. C. (2020). Evaluation of the Effect of Gold Mining on the Water Quality in Monterrey, Bolívar (Colombia). *Water*, 12(9), 2523. <https://doi.org/10.3390/w12092523>
- McNairn, H., & Protz, R. (1993). Mapping corn residue cover on agricultural fields in Oxford county, Ontario, using thematic mapper. *Canadian Journal of Remote Sensing*, 19(2), 152–159. <https://doi.org/10.1080/07038992.1993.10874543>
- Mellor, A., Boukir, S., Haywood, A., & Jones, S. (2015). Exploring issues of training data imbalance and mislabelling on random forest performance for large area land cover classification using the ensemble margin. *ISPRS Journal of Photogrammetry and Remote Sensing*, 105, 155–168. <https://doi.org/10.1016/j.isprsjprs.2015.03.014>
- Millard, K., & Richardson, M. (2015). On the Importance of Training Data Sample Selection in Random Forest Image Classification: A Case Study in Peatland Ecosystem Mapping. *Remote Sensing*, 7(7), 8489–8515. <https://doi.org/10.3390/rs70708489>
- Mitchell, A. L., Rosenqvist, A., & Mora, B. (2017). Current remote sensing approaches to monitoring forest degradation in support of countries measurement, reporting and verification (MRV) systems for REDD+. *Carbon Balance and Management*, 12(1), 1–22.

<https://doi.org/10.1186/s13021-017-0078-9>

- Mohanaiah, P., Sathyanarayana, P., & GuruKumar, L. (2013). Image texture feature extraction using GLCM approach. *International Journal of Scientific and Research Publications*, 3(5), 1–5.
- Morgan, J. L., & Gergel, S. E. (2013). Automated analysis of aerial photographs and potential for historic forest mapping. *Canadian Journal of Forest Research*, 43(8), 699–710. <https://doi.org/10.1139/cjfr-2012-0492>
- Mugiraneza, T., Nascetti, A., & Ban, Y. (2020). Continuous Monitoring of Urban Land Cover Change Trajectories with Landsat Time Series and LandTrendr-Google Earth Engine Cloud Computing. *Remote Sensing*, 12(18), 2883. <https://doi.org/10.3390/rs12182883>
- Nagendra, H., Lucas, R., Honrado, J. P., Jongman, R. H. G., Tarantino, C., Adamo, M., & Mairotta, P. (2013). Remote sensing for conservation monitoring: Assessing protected areas, habitat extent, habitat condition, species diversity, and threats. *Ecological Indicators*, 33, 45–59. <https://doi.org/10.1016/j.ecolind.2012.09.014>
- Ngom, N. M., Mbaye, M., Baratoux, D., Baratoux, L., Catry, T., Dessay, N., ... Delaitre, E. (2020). Mapping Artisanal and Small-Scale Gold Mining in Senegal Using Sentinel 2 Data. *GeoHealth*, 4(12), e2020GH000310. <https://doi.org/10.1029/2020GH000310>
- Obeng, E. A., Oduro, K. A., Obiri, B. D., Abukari, H., Guuroh, R. T., Djagbletey, G. D., ... Appiah, M. (2019). Impact of illegal mining activities on forest ecosystem services: local communities' attitudes and willingness to participate in restoration activities in Ghana. *Heliyon*, 5(10), e02617. <https://doi.org/10.1016/j.heliyon.2019.e02617>
- Ofosu, G., Dittmann, A., Sarpong, D., & Botchie, D. (2020, April 1). Socio-economic and environmental implications of Artisanal and Small-scale Mining (ASM) on agriculture and livelihoods. *Environmental Science and Policy*, Vol. 106, pp. 210–220. <https://doi.org/10.1016/j.envsci.2020.02.005>
- Peterson, G. D., & Heemskerk, M. (2001). Deforestation and forest regeneration following small-scale gold mining in the Amazon: the case of Suriname. *Environmental Conservation*, 117–126.
- PlanetGOLD. (2020). *ANNUAL PROGRESS REPORT 2019/2020*. New York, EEUU.
- Qi, Y., & Wu, J. (1996). Effects of changing spatial resolution on the results of landscape pattern analysis using spatial autocorrelation indices. *Landscape Ecology*, 11(1), 39–49. <https://doi.org/10.1007/BF02087112>
- RAISG. (2020). Amazon Geo-Referenced Socio-Environmental Information Network. Retrieved from <https://mineria.amazoniasocioambiental.org/> website: <https://mineria.amazoniasocioambiental.org/>
- Ramola, A., Shakya, A. K., & Van Pham, D. (2020). Study of statistical methods for texture analysis and their modern evolutions. *Engineering Reports*, 2(4), e12149. <https://doi.org/10.1002/eng2.12149>
- Riddell, A. P., Fitzgerald, S. A., Qi, C., & Strimbu, B. M. (2020). Classification Strategies for Unbalanced Binary Maps: Finding Ponderosa Pine (*Pinus ponderosa*) in the Willamette Valley. *Remote Sensing*, 12(20), 3325. <https://doi.org/10.3390/rs12203325>
- Rogan, J., Miller, J., Stow, D., Franklin, J., Levien, L., & Fischer, C. (2003). Land-cover change

- monitoring with classification trees using Landsat TM and ancillary data. *Photogrammetric Engineering and Remote Sensing*, 69(7), 793–804. <https://doi.org/10.14358/PERS.69.7.793>
- Rogers, C. (2005). *Artisanal and Small Scale Mining, Presentation at the Workshop on Integrated Resource Planning: Managing Mineral Wealth*. Kampala, Uganda.
- Roulet, M., Lucotte, M., Canuel, R., Farella, N., De Freitos Goch, Y. G., Pacheco Peleja, J. R., ... Amorim, M. (2001). Spatio-temporal geochemistry of mercury in waters of the Tapajós and Amazon rivers, Brazil. *Limnology and Oceanography*, 46(5), 1141–1157. <https://doi.org/10.4319/lo.2001.46.5.1141>
- Rouse, J. W., Haas, R. H., Schell, J. A., & Deering, D. W. (1974). Monitoring vegetation systems in the Great Plains with ERTS. *NASA Special Publication*, 351(1974), 309.
- Roy, D. P., Kovalskyy, V., Zhang, H. K., Vermote, E. F., Yan, L., Kumar, S. S., & Egorov, A. (2016). Characterization of Landsat-7 to Landsat-8 reflective wavelength and normalized difference vegetation index continuity. *Remote Sensing of Environment*, 185, 57–70. <https://doi.org/10.1016/j.rse.2015.12.024>
- Ruiz, L. A., Fdez-Sarría, ; A., & Recio, J. A. (2004). *TEXTURE FEATURE EXTRACTION FOR CLASSIFICATION OF REMOTE SENSING DATA USING WAVELET DECOMPOSITION: A COMPARATIVE STUDY*.
- Salman, T., & de Theije, M. (2017). Analysing conflicts around small-scale gold mining in the Amazon: The contribution of a multi-temporal model. *Extractive Industries and Society*, 4(3), 586–594. <https://doi.org/10.1016/j.exis.2017.03.007>
- Sanchez-Pinto, L. N., Venable, L. R., Fahrenbach, J., & Churpek, M. M. (2018). Comparison of variable selection methods for clinical predictive modeling. *International Journal of Medical Informatics*, 116, 10–17. <https://doi.org/10.1016/j.ijmedinf.2018.05.006>
- Shaban, M. A., & Dikshit, O. (2001). Improvement of classification in urban areas by the use of textural features: The case study of Lucknow city, Uttar Pradesh. *International Journal of Remote Sensing*, 22(4), 565–593. <https://doi.org/10.1080/01431160050505865>
- Small, C. (2001). Estimation of urban vegetation abundance by spectral mixture analysis. *International Journal of Remote Sensing*, 22(7), 1305–1334. <https://doi.org/10.1080/01431160151144369>
- Spiegel, S. J., & Veiga, M. M. (2010). International guidelines on mercury management in small-scale gold mining. *Journal of Cleaner Production*, 18(4), 375–385. <https://doi.org/10.1016/j.jclepro.2009.10.020>
- Stone, K. H. (1964). A Guide to the Interpretation and Analysis of Aerial Photos. *Annals of the Association of American Geographers*, 54(3), 318–328. <https://doi.org/10.1111/j.1467-8306.1964.tb00492.x>
- Swenson, J J, Carter, C. E., Domec, J.-C., & Delgado, C. I. (2011). Gold Mining in the Peruvian Amazon: Global Prices, Deforestation, and Mercury Imports. *PLoS ONE*, 6(4), 18875. <https://doi.org/10.1371/journal.pone.0018875>
- Swenson, Jennifer J., Carter, C. E., Domec, J.-C., & Delgado, C. I. (2011). Gold Mining in the Peruvian Amazon: Global Prices, Deforestation, and Mercury Imports. *PLoS ONE*, 6(4), e18875. <https://doi.org/10.1371/journal.pone.0018875>

- Swiss Cooperation Office. (2013). *Annual Report 2012 Swiss Agency for Development and Cooperation (SDC) in Mongolia*. Retrieved from www.swissconsulate.mn
- Szantoi, Z., Escobedo, F., Abd-Elrahman, A., Smith, S., & Pearlstine, L. (2013). Analyzing fine-scale wetland composition using high resolution imagery and texture features. *International Journal of Applied Earth Observation and Geoinformation*, 23(1), 204–212. <https://doi.org/10.1016/j.jag.2013.01.003>
- Telmer, K., & Stapper, D. (2007). Evaluating and monitoring small scale gold mining and mercury use: Building a knowledge-base with satellite imagery and field work. *United Nations Industrial Development Organization: Victoria, BC, Canada*.
- Thompson, S. D., & Gergel, S. E. (2008). Conservation implications of mapping rare ecosystems using high spatial resolution imagery: Recommendations for heterogeneous and fragmented landscapes. *Landscape Ecology*, 23(9), 1023–1037. <https://doi.org/10.1007/s10980-008-9263-2>
- Touw, W. G., Bayjanov, J. R., Overmars, L., Backus, L., Boekhorst, J., Wels, M., & Sacha van Huijum, A. F. T. (2013). Data mining in the life science with random forest: A walk in the park or lost in the jungle? *Briefings in Bioinformatics*, 14(3), 315–326. <https://doi.org/10.1093/bib/bbs034>
- TrimbleInc. (2015). eCognition Suite Overview. Retrieved April 6, 2021, from Trimble Germany GmbH website: <https://docs.ecognition.com/v9.5.0/Page collection/eCognition Suite Overview.htm>
- UNEP. (2012). *Analysis of formalization approaches in the artisanal and small-scale gold mining sector based on experiences in Ecuador*. Retrieved from <http://www.unep.org/hazardoussubstances/Mercury/PrioritiesforAction/ArtisanalandSmallScaleGoldMining/Report>
- UNEP. (2013). *MINAMATA CONVENTION ON MERCURY*. Retrieved from www.unep.org/www.unep.org/www.mercuryconvention.org
- UNEP. (2014). *Intergovernmental negotiating committee to prepare a global legally binding instrument on mercury Sixth session*. Bangkok.
- UNITAR, & UNEP. (2018). *Handbook for Developing National ASGM Formalization Strategies within National Action Plans*. Geneva.
- Unser, M. (1986). Sum and Difference Histograms for Texture Classification. *IEEE Transactions on Pattern Analysis and Machine Intelligence, PAMI-8*(1), 118–125. <https://doi.org/10.1109/TPAMI.1986.4767760>
- Veiga, M. M., Maxson, P. A., & Hylander, L. D. (2006). Origin and consumption of mercury in small-scale gold mining. *Journal of Cleaner Production*, 14(3–4), 436–447. <https://doi.org/10.1016/j.jclepro.2004.08.010>
- Virdi, J. S., Peng, W., & Sata, A. (2019). Feature selection with LASSO and VSURF to model mechanical properties for investment casting. *ICCID 2019 - 2nd International Conference on Computational Intelligence in Data Science, Proceedings*. <https://doi.org/10.1109/ICCID.2019.8862141>
- Vogeler, J. C., Braaten, J. D., Slesak, R. A., & Falkowski, M. J. (2018). Extracting the full value of the Landsat archive: Inter-sensor harmonization for the mapping of Minnesota forest canopy cover (1973–2015). *Remote Sensing of Environment*, 209, 363–374.

<https://doi.org/10.1016/j.rse.2018.02.046>

- Wagner, L. (2016). *Organized Crime and Illegally Mined Gold in Latin America*. Retrieved from <https://globalinitiative.net/wp-content/uploads/2016/03/Organized-Crime-and-Illegally-Mined-Gold-in-Latin-America.pdf>
- Wang, C., Chen, J., Wu, J., Tang, Y., Shi, P., Black, T. A., & Zhu, K. (2017). A snow-free vegetation index for improved monitoring of vegetation spring green-up date in deciduous ecosystems. *Remote Sensing of Environment*, 196, 1–12. <https://doi.org/10.1016/j.rse.2017.04.031>
- Wasige, J. E., Groen, T. A., Smaling, E., & Jetten, V. (2012). Monitoring basin-scale land cover changes in Kagera Basin of Lake Victoria using: Ancillary data and remote sensing. *International Journal of Applied Earth Observation and Geoinformation*, 21(1), 32–42. <https://doi.org/10.1016/j.jag.2012.08.005>
- Wilson, E. H., & Sader, S. A. (2002). Detection of forest harvest type using multiple dates of Landsat TM imagery. *Remote Sensing of Environment*, 80(3), 385–396. [https://doi.org/10.1016/S0034-4257\(01\)00318-2](https://doi.org/10.1016/S0034-4257(01)00318-2)
- World Health Organization. (2019). *Strategic planning for implementation of the health-related articles of the Minamata Convention on Mercury*. Retrieved from licence: CC BY-NC-SA 3.0 IGO
- Xiao, W., Deng, X., He, T., & Chen, W. (2020). Mapping Annual Land Disturbance and Reclamation in a Surface Coal Mining Region Using Google Earth Engine and the LandTrendr Algorithm: A Case Study of the Shengli Coalfield in Inner Mongolia, China. *Remote Sensing*, 12(10), 1612. <https://doi.org/10.3390/rs12101612>
- Xiao, X., Boles, S., Frolking, S., Salas, W., Moore Iii, B., Li, C., ... Zhao, R. (2002). Observation of flooding and rice transplanting of paddy rice fields at the site to landscape scales in China using VEGETATION sensor data. *International Journal of Remote Sensing*, 23(15), 3009–3022.
- Xu, H., Wei, Y., Liu, C., Li, X., & Fang, H. (2019). A scheme for the long-term monitoring of impervious-relevant land disturbances using high frequency Landsat archives and the Google Earth Engine. *Remote Sensing*, 11(16), 1891. <https://doi.org/10.3390/rs11161891>
- Xue, J., & Su, B. (2017). Significant remote sensing vegetation indices: A review of developments and applications. *Journal of Sensors*, Vol. 2017. <https://doi.org/10.1155/2017/1353691>
- Yang, X., Tridandapani, S., Beitler, J. J., Yu, D. S., Yoshida, E. J., Curran, W. J., & Liu, T. (2012). Ultrasound GLCM texture analysis of radiation-induced parotid-gland injury in head-and-neck cancer radiotherapy: An in vivo study of late toxicity. *Medical Physics*, 39(9), 5732–5739. <https://doi.org/10.1118/1.4747526>
- Yang, Y., Erskine, P. D., Lechner, A. M., Mulligan, D., Zhang, S., & Wang, Z. (2018). Detecting the dynamics of vegetation disturbance and recovery in surface mining area via Landsat imagery and LandTrendr algorithm. *Journal of Cleaner Production*, 178, 353–362. <https://doi.org/10.1016/j.jclepro.2018.01.050>
- Zhu, Z., & Woodcock, C. E. (2014). Continuous change detection and classification of land cover using all available Landsat data. *Remote Sensing of Environment*, 144, 152–171. <https://doi.org/10.1016/j.rse.2014.01.011>

7. APPENDIXES

7.1 LandTrendr Parameters for Texture

	IDM	CONT	ASM	CORR	VAR	ENT	DVAR	DENT	DISS	INERTIA	SHADE	PROM	Texture Parameter
B1	8	6	6	10	10	8	10	8	8	8	10	10	Max Segments
	0.9	0.9	0.9	0.5	0.1	0.9	0.2	0.9	0.9	0.2	0.1	0.1	Spike Threshold
	3	3	3	3	3	1	1	2	2	1	5	1	Vertex Count Overshoot
	TRUE	TRUE	TRUE	Prevent One Year Recovery									
	0.25	0.25	0.25	0.25	0.95	0.25	0.45	0.25	0.25	0.85	0.95	0.98	Recover Threshold
	0.05	0.05	0.05	0.05	0.05	0.05	0.05	0.05	0.05	0.05	0.05	0.05	Pval. Threshold
	0.75	0.75	0.75	0.75	0.75	0.75	0.75	0.75	0.75	0.75	0.75	0.75	Best Model Proportion
B2	6	6	6	6	7	6	6	6	6	6	6	6	Min Observations Needed
	10	8	6	10	8	8	10	6	9	10	12	10	Max Segments
	0.1	0.1	0.9	0.2	0.1	0.1	0.5	0.7	0.9	0.9	0.1	0.1	Spike Threshold
	1	1	3	1	1	1	1	3	3	3	1	1	Vertex Count Overshoot
	TRUE	TRUE	TRUE	Prevent One Year Recovery									
	0.35	0.75	0.25	0.7	0.9	0.9	0.9	0.25	0.85	0.6	0.9	0.9	Recover Threshold
	0.05	0.05	0.05	0.05	0.05	0.05	0.05	0.05	0.05	0.05	0.05	0.05	Pval. Threshold
B3	0.75	0.75	0.75	0.75	0.75	0.75	0.75	0.75	0.75	0.75	0.75	0.75	Best Model Proportion
	6	6	6	6	6	6	6	6	6	6	6	6	Min Observations Needed
	10	10	6	11	11	6	6	6	7	9	12	12	Max Segments
	0.6	0.6	0.9	0.2	0.1	0.9	0.9	0.9	0.9	0.9	0.1	0.1	Spike Threshold
	1	1	3	3	3	3	3	3	3	3	3	3	Vertex Count Overshoot
	TRUE	TRUE	TRUE	Prevent One Year Recovery									
	0.3	0.3	0.25	0.25	0.5	0.25	0.7	0.25	0.8	0.9	0.9	0.9	Recover Threshold
B4	0.05	0.05	0.05	0.05	0.05	0.05	0.05	0.05	0.05	0.05	0.05	0.05	Pval. Threshold
	0.75	0.75	0.75	0.75	0.75	0.75	0.75	0.75	0.75	0.75	0.75	0.75	Best Model Proportion
	6	6	6	6	6	6	6	6	6	6	6	6	Min Observations Needed
	12	9	6	12	8	6	12	6	6	12	10	12	Max Segments
	0.1	0.6	0.9	0.1	0.1	0.9	0.1	0.9	0.1	0.1	0.1	0.2	Spike Threshold
	1	1	3	1	1	3	3	3	3	1	3	3	Vertex Count Overshoot
	TRUE	TRUE	TRUE	Prevent One Year Recovery									
B5	0.3	0.6	0.25	0.25	0.6	0.6	0.9	0.25	0.9	0.25	0.25	0.6	Recover Threshold
	0.05	0.05	0.05	0.05	0.05	0.05	0.05	0.05	0.05	0.05	0.05	0.05	Pval. Threshold
	0.75	0.95	0.75	0.75	0.75	0.75	0.75	0.75	0.75	0.75	0.75	0.75	Best Model Proportion
	7	6	6	6	6	6	7	6	6	6	8	6	Min Observations Needed
	12	12	6	9	12	6	12	6	8	10	13	12	Max Segments
	0.01	0.1	0.9	0.05	0.1	0.9	0.1	0.9	0.9	0.05	0.01	0.1	Spike Threshold
	1	1	3	3	3	3	1	3	1	1	1	1	Vertex Count Overshoot
B7	TRUE	TRUE	TRUE	Prevent One Year Recovery									
	0.99	0.99	0.25	0.25	0.99	0.6	0.45	0.25	0.99	0.99	0.95	0.99	Recover Threshold
	0.05	0.05	0.05	0.05	0.05	0.05	0.05	0.05	0.05	0.05	0.05	0.05	Pval. Threshold
	0.95	0.75	0.75	0.75	0.75	0.75	0.75	0.75	0.75	0.75	0.75	0.75	Best Model Proportion
	7	6	6	6	6	6	6	6	6	6	6	6	Min Observations Needed

7.2 Partial Dependence Plots

